Application of boundary layer suction on the vertical fin of a sailplane

A Smith

orcid.org/0000-0003-2329-1376

Dissertation submitted in fulfilment of the requirements for the degree Master of Science in Engineering Science with Mechanical Engineering at the

North-West University

Supervisor: Dr. JJ Bosman

Graduation: August 2021

Student number: 25105280

ABSTRACT

High-performance aircraft have advanced so much in recent years that every part of a sailplane has to be investigated and improved separately in order to discover prospective areas for improvement. One of these areas is the vertical stabilizer of the sailplane. Sailplanes operate in the flow region where both laminar and turbulent boundary layers are present on the surfaces. In order to reduce drag, longer laminar flow regions must be established. Boundary layer control in the form of suction is a potential method to increase performance and is thus investigated.

Boundary layer suction is an active boundary layer control method used to decrease the drag of a body moving through a fluid by keeping the boundary layer laminar past the point where transition occurs naturally. This is a drag reduction technique to remove the slowed bottom part of the boundary layer through slots or a poriferous material.

High-performance sailplanes cannot make use of an external source of propulsion, which means that a pump cannot be used to drive the system. Therefore, a low-pressure zone on the vertical stabilizer must be identified to be used as the source of suction.

In this research, computational fluid dynamics (CFD) was used to investigate the possibility to reduce drag on a glider's vertical fin with the application of boundary layer suction. The results include the location and design of the outlet on the tail section, as well as the layout of suction holes that would result in the largest reduction in drag.

It is evident from the results of this study that boundary layer suction on the JS3 vertical stabilizer is not a viable option. Although boundary layer suction reduce drag by $20\ \%$, a necessary suction outlet port, however, increases drag. The final result is a net loss of aerodynamic performance on the vertical stabilizer.

TABLE OF CONTENTS

LIST OF TABLES

LIST OF FIGURES

ACKNOWLEDGEMENTS

First of all, I want to thank God for granting me the ability to be able to complete this project with success. I also wish to convey my gratitude to my parents for their constant support in my studies; my father, from whom I got my love for aviation and who taught me to be determined, and my mother who always believed in my academic endeavours.

I would also like to thank my other half for his love and support, as well as my friends without whom this project would not be a success.

Lastly, I want to thank my study leader for his assistance and guidance throughout the creation of this dissertation.

KEYWORDS

Boundary layer suction, boundary layer control, boundary layer transition, CFD, Computational fluid dynamics, drag reduction, sailplane, STAR-CCM+.

NOMENCLATURE

Abbreviations

AOA	Angle of attack
CAD	Computer-aided design
CFD	Computational fluid dynamics
LFC	Laminar flow control
NACA	National Advisory Committee on Aeronautics
RANS	Reynolds-averaged Navier-Stokes

Symbols

c	Chord length $[m]$
C_D	Drag coefficient
C_f	Skin friction coefficient
C_L	Lift coefficient
C_p	Pressure coefficient
C_q	Suction coefficient
D	Drag $[N]$
L	Lift $[N]$
$\dot{m}$	Mass flow $[kg/s]$
N	Critical amplification factor for e^N transition model
p	Pressure $[kPa]$
Re	Reynolds number
Re_{crit}	Critical Reynolds number

S_{body} Surface of the body $[m^2]$

U_∞ Free-stream velocity $[m/s]$

V Velocity $[m/s]$

y Wall distance $[m]$

Greek and special letters

δ Boundary layer thickness $[m]$

δ^* Displacement thickness $[m]$

λ Intermittency

μ Dynamic viscosity $[Ns/m^2]$

v Kinematic viscosity $[m^2/s]$

ρ Density $[kg/m^3]$

τ Shear stress $[N/m^2]$

CHAPTER 1: INTRODUCTION

1.1 Background

New developments in high-performance gliders are driven by the need for improved performance to stay ahead of the competition. There is little room for further aerodynamic development on these high-performance aircraft if the same design methods or tools, such as panel methods, are used as before (van Leer, 2010). According to Blazek (2015), physics, numerical mathematics and computer sciences were integrated during the 1970's to create computational fluid dynamics (CFD). CFD was utilized to simulate simple flows, as well as free and confined jet flows (Khalil & Akademia Baru, 2012). The field of CFD has improved immensely in the last ten years, with work done to a great extent on transition prediction models. These models are essential to accurately predict the lift and drag produced by aircraft. Both laminar and turbulent flow exists on aircraft and, because drag produced by turbulent flow exceeds drag generated from laminar flow, the prediction of the transition location is vital for accurate drag calculation.

The aerodynamic friction between a solid and a fluid is called skin friction drag. Friction between the solid object and the fluid produces a thin layer of decelerated fluid next to the body's surface. The friction forces occur due to the viscosity of the fluid. Another contributing factor to the extent of the friction force, is the roughness of the body's skin. In 1904, Ludwig Prandtl examined the layer of fluid touching the surface subjected to these friction forces. This thin layer decelerated flow adjacent to the body is called the boundary layer (Braslow, 1999).

The boundary layer near the surface of the body is mainly laminar or turbulent in low-speed aerodynamics. When the flow remains well-ordered, the boundary layer flow is laminar. When the boundary layer is turbulent, the fluid elements mix and the frictional force's skin drag is much larger than in the laminar case. This drag increase is due to momentum losses connected with the mixing of fluid layers. The energy needed to overcome the viscous drag forms a significant part in the total energy required for an airplane to fly (Braslow, 1999). According to Beck *et al.* (2018), turbulent boundary layers create five to ten times more viscous drag than laminar boundary layers. This drag increase means that laminar flow is pursued when designing high-performance gliders.

Laminar flow is an unstable flow state that easily transitions to turbulent flow because of magnification of disturbances. Laminar-turbulent transition takes place when air flows from a low-pressure, high-speed zone to a high-pressure, low-speed zone. Air flows naturally from a high to a low pressure, and thus gives resistance to flow in the previous scenario. The airflow becomes unstable and friction occurs between the air particles and the aircraft. This friction causes the

laminar boundary layer flow to transition. In the trailing edge region of wings, an adverse pressure gradient is present, which means that active boundary layer control can be used. Laminar flow is achieved for a more substantial chord length percentage of the wing with the implementation of active boundary layer control (Braslow, 1999). Boundary layer control is described as the manipulation or control of the boundary layer to produce the desired result.

Boundary layer suction takes place when the flow in the boundary layer is removed through the surface of the body before laminar-turbulent transition can occur. Successful implementation of boundary layer suction lengthens the laminar flow region over the body. This form of active boundary layer control was found by researchers to improve the glider's glide ratio from 43 to 60 (Boermans, 2006; Bridges, 2007). Boundary layer suction is the main focus of this study and will be discussed in-depth in the chapters that follow.

1.2 Problem definition

There is an ongoing need to enhance the performance of gliders used in competitions. Drag reduction of a glider increases the performance. The JS3 is a high-performance glider where the margin for further aerodynamic improvement is small. Specific areas of the glider with possible room for improvement must be examined. One such area is the vertical stabilizer because of the region of turbulent flow at the airfoil's trailing edge. By implementing boundary layer suction on the vertical stabilizer, this turbulent region can be minimized. The flow in the area where boundary layer suction is implemented is complex, and CFD could be used to analyse this region.

Sailplanes operate at Reynolds number ranges where both laminar and turbulent flow occur, and where separation of flow can take place. Transition from one flow regime to the next must be predicted accurately to calculate aerodynamic properties, like lift and drag, without error. Previous methods used in the design of sailplanes, such as panel methods, were unsuccessful when certain aerodynamic events occurred. These events include flow separation and the instance when the interaction between the viscous and inviscid flow becomes too strong. Thus, suitable design methods are required. Researchers recently conducted a substantial amount of work on transition prediction models for CFD software, but these models should be validified before it can be applied to boundary layer suction research.

A suction pump can aid in boundary layer suction, but additional energy sources to drive this pump are prohibited in gliding competitions. The reason is that a suction pump that provides a force to assist in boundary layer suction, is viewed as an engine as it increases the performance of the sailplane. FAI Sporting Code for Gliding states that a glider is a fixed-wing aircraft with no means of propulsion. Thus, gliders taking part in FAI Sporting Events are forbidden to make use of pumps (Internationale, 2008). Therefore, a natural, low-pressure region on the sailplane needs to be implemented as the source for boundary layer suction. This region must also have the ability to create a large enough mass flow through the boundary layer suction holes to maximally reduce the drag. The outlet situated in this low-pressure zone must be designed to produce the least amount of drag in order to obtain meaningful results.

1.3 Project objectives

This dissertation focuses on the following objectives:

- The validation of the CFD transition models against experimental results for similar flow conditions as found on sailplanes.
- To examine the application and feasibility of boundary layer suction on the vertical stabilizer of the JS3.
- To find the optimum boundary layer suction position for maximum drag reduction in order to improve the overall efficiency of the sailplane. This includes hole size, location on chord and distance between holes, as well as the number of holes.
- To find a natural, low-pressure zone near the vertical stabilizer of the sailplane which can be utilized as the source for boundary layer suction by providing adequate flow rates and low pressure for the reduction of drag.
- To determine the net gain or loss in performance when all the factors are considered.

1.4 Layout of this dissertation

Chapter 1: Introduction

The introduction forms the outline of this dissertation. The background behind boundary layer suction, the problem as well as the objectives are defined.

Chapter 2: Fundamentals of boundary layer suction

The literature study forms a summary of the relevant knowledge available on all aspects of boundary layer suction. The literature is obtained from studies on the topic, academic resources and books. Topics include boundary layer theory, and the focus is on laminar and turbulent flow. Transition and drag are also discussed. The focal point is on how boundary layer suction influences these topics.

Chapter 3: Numerical modelling of boundary layer suction with CFD

This chapter is the second part of the literature survey. An overview is provided of turbulence and transition modelling in CFD, as well as the requirements of both for accurate results.

Chapter 4: Two-dimensional validation

The two-dimensional CFD model is validated by comparing XFOIL results of the airfoil to wind tunnel experimental data and results obtained from STAR-CCM+.

Chapter 5: Three-dimensional validation

The three-dimensional studies are executed on the Standard Cirrus glider where transitional flow is present. Experimental data was used for comparison with the studies to validate the CFD model.

Chapter 6: Boundary layer suction modelling

This chapter includes all CFD studies related to boundary layer suction on the JS3 vertical stabilizer airfoil. Boundary layer suction is implemented on a two-dimensional airfoil as a preliminary study. Improvements are made for the application of boundary layer suction on the three-dimensional airfoil.

Chapter 7: Boundary layer suction system application

The outlet specifications for the boundary layer suction system are addressed. It contains a discussion of the results of boundary layer suction applied on the vertical stabilizer. All the results from the combined system are addressed here.

Chapter 8: Conclusion and recommendations

This chapter concludes the investigation and recommendations for future studies regarding boundary layer suction are made.

CHAPTER 2: FUNDAMENTALS OF BOUNDARY LAYER SUCTION

The development of boundary layer suction for application on aircraft progressed significantly in the last two decades. When boundary layer suction is implemented successfully, the performance of the aircraft is enhanced. Chapter 2 gives a detailed explanation of the theory behind boundary layer suction. Several factors that influence boundary layer suction, including laminar-turbulent transition and flow instabilities, are discussed. The connection between boundary layer suction and drag is also explored. The latter part of this chapter elaborates more on the challenges that may arise with the application of boundary layer suction on aircraft.

2.1 Introduction to boundary layer suction

Laminar flow control is a means to promote and extend the laminar flow condition. This enlargement of the laminar region is done by delaying or preventing transition to take place, which in turn reduces the skin friction. Boundary layer suction is an active form of boundary layer flow control, where the air is removed from the boundary layer through slots or a poriferous material (Boermans, 2006). The reduction in drag when boundary layer suction is implemented, is also the result of minimizing the boundary layer thickness (Green, 1997). Removing a piece of the boundary layer helps maintain the stabilization of the boundary layer by filling up the velocity profile close to the airfoil (Schlichting & Gersten, 2017), as illustrated in Figure 2-1.

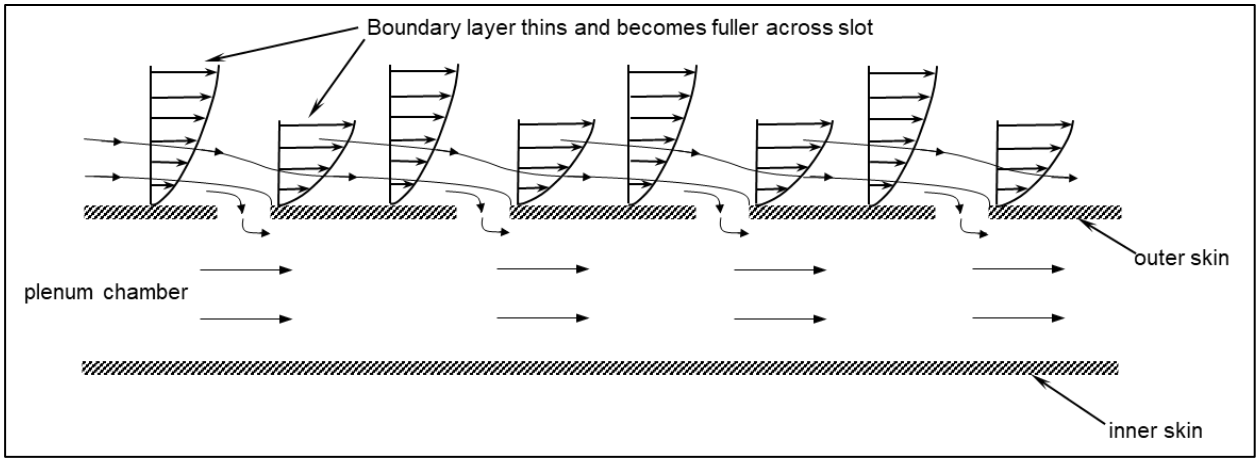

Figure 2-1: Boundary layer velocity profile before and after suction slots (McCormick, 2009)

When boundary layer suction is implemented near the trailing edge of an airfoil, the result is a favourable pressure gradient on a larger airfoil area. This increases the laminar flow region over the airfoil, reducing skin friction and the overall drag. The advantage of a larger region laminar flow can be better understood when examining boundary layer theory in more detail. Blowing, a method where flow is introduced into the boundary layer through holes, is the only form of active boundary layer control being used on gliders at this time (Jonker, 2011). The goal of blowing is to deliberately force transition of the boundary layer to turbulent flow before separation occurs. Turbulent flow resists separation better than laminar flow. Although boundary layer suction has not yet been implemented on gliders, the concept thereof has shown great potential in studies.

2.2 Boundary layer theory

When examining a flat plate submerged in a steady stream of fluid, the boundary layer concept can be easily understood. Air exhibits a no-slip condition ascribed by the fluid's viscosity, which means that the fluid's velocity on the plate's surface is zero; the fluid's velocity transition from being stationary directly next to the surface, to the velocity of the mainstream flow (Schlichting & Gersten, 2017). This transition in velocity through a thin layer of fluid near the surface is called the boundary layer (Schlichting & Gersten, 2017), where the frictional forces are the reason for the velocity gradient $\frac{\partial u}{\partial y}$ (Katz, 2003). The fluid's viscosity outside the boundary layer is negligible because the flow is associated with an inviscid solution and is called the inviscid outer flow.

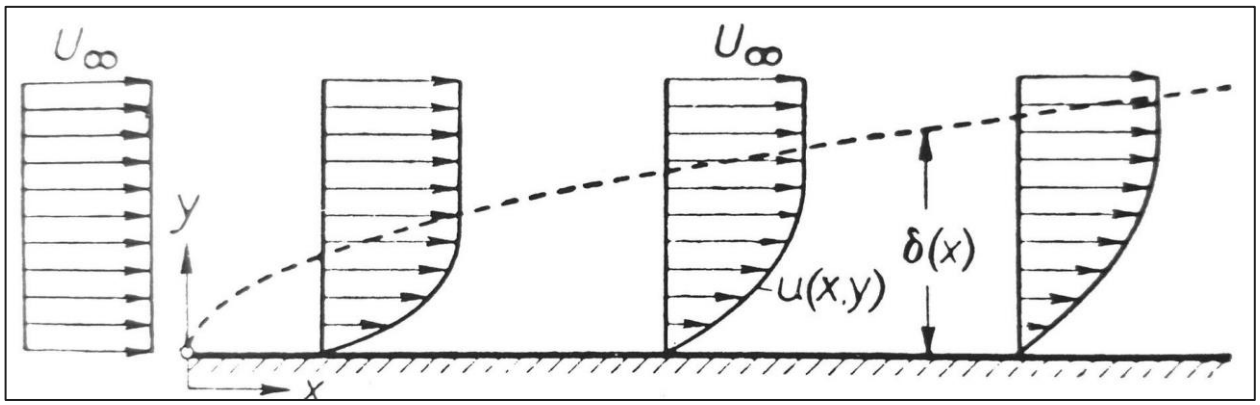

Figure 2-2: Velocity distribution in the boundary layer (Schlichting & Gersten, 2017)

Figure 2-2 visualizes the velocity distribution in the boundary layer. The thickness of the boundary layer, δ, is the space between the body to where the boundary layer velocity reaches the mainstream value, U_∞. Since there is no definite separation line between the boundary layer and the bottom of the outer flow, the thickness of the boundary layer is not easily defined. A more palpable definition is therefore used. The displacement thickness, δ^*, is defined by the displacement the inviscid flow undergoes due to the boundary layer (Schlichting & Gersten, 2017) and, given by equation 2.1, U depicts the velocity at the border of the boundary layer.

$$\delta^* = \int_0^\infty \left(1 - \frac{u}{U}\right) dy \tag{2.1}$$

Because of the different velocities in the boundary layer, the fluid is subjected to relative internal movement. The internal movement in turn establishes changes in the inertial and frictional forces. The Reynolds number characterizes the correlation between the inertial and viscous forces generated in the boundary layer. Equation 2.2 denotes the formula for the Reynolds number (Katz, 2003), with ρ being the fluid density, μ being the viscosity, V being the velocity and L being the characteristic length of the solid.

$$\mathrm{Re} = \frac{\rho \mathrm{V} \mathrm{L}}{\mu} \tag{2.2}$$

When the ratio between the inertial to viscous forces is relatively small, the boundary layer fluid moves parallel to the wall. This parallel movement of fluid adjacent to the wall is called a laminar boundary layer. When the ratio is high, the fluid starts to mix and the boundary layer is turbulent. These two concepts will be discussed in more detail in sections 2.2.1 and 2.2.2.

Shear force experienced at the wall is vastly influenced by the boundary layer state, namely laminar or turbulent. The shear force is present due to the fluid's viscosity, and is directly proportional to the velocity profile gradient in the boundary layer. Equation 2.3 provides the definition for shear stress, with μ being the dynamic viscosity of the fluid.

$$\tau_w = \mu \left(\frac{\partial u}{\partial y}\right)_w \tag{2.3}$$

Skin friction drag is acquired when the shear stress at the wall is integrated along the surface. The non-dimensional value that plays a crucial role in skin friction drag, is the skin friction coefficient C_f. To find C_f, the wall shear stress is divided by the dynamic pressure of the inviscid outer flow, as can be seen in equation 2.4.

$$C_f = \frac{\tau_w}{\frac{1}{2}\rho U_\infty^2} \tag{2.4}$$

As previously stated, the boundary layer state influences skin friction. The following two sections will elaborate more on the association between a laminar or turbulent boundary layer and skin friction.

2.2.1 Laminar boundary layer

Laminar flow can also be described as layered flow where the fluid layers are smooth and move parallel to the wall; the fluid particles are not exchanged perpendicular to the wall in a laminar boundary layer. A thickening of the boundary layer with distance occurs along the plate as the fluid in the upper layers is influenced by the frictional forces. A thick boundary layer creates a more significant amount of viscous friction drag than a thin boundary layer. Frictional forces hinder the forward movement of an object through a fluid and establish a force in the direction opposing motion, which is called skin friction drag.

When considering fluid motion over a flat plate, a laminar boundary layer starts to grow at the leading edge. The height of the boundary layer increases as the fluid progresses over the plate. Figure 2-3 depicts fluid motion over a flat plate. A laminar boundary layer starts to grow at the

leading edge and the height of the boundary layer increases as the fluid progresses over the plate. A turbulent boundary layer develops after some distance when the flow becomes unstable.

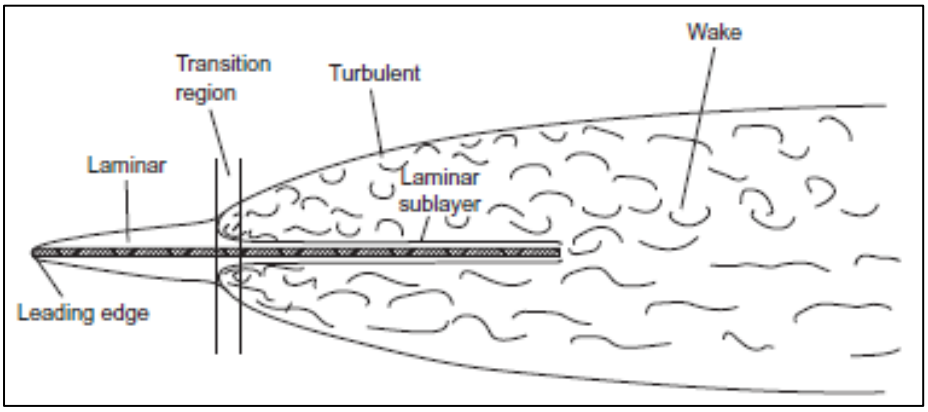

Figure 2-3: Visualization of a boundary layer on a flat plate (Houghton *et al.*, 2016)

2.2.2 Turbulent boundary layer

The streamlines and velocity in a turbulent boundary layer fluctuate and the fluid has an irregular flow pattern, causing the fluid particles to be exchanged between adjacent layers (Schlichting & Gersten, 2017). The thickness of a boundary layer in a turbulent boundary layer increases faster than that of a laminar boundary layer due to the mixing of fluid. Shear forces are also more significant due to the mixing and the exchange of momentum between layers, meaning that the skin friction drag will be extensive for turbulent flow.

Turbulent flow, however, cannot occur in the immediate region next to the wall. A viscous sublayer exists underneath the turbulent region in which the flow is laminar; this phenomenon is visible in Figure 2-3 (Houghton *et al.*, 2016). The viscous sublayer is an area of decelerated flow next to the wall, where the influences of viscosity are limited to that region (Schlichting & Gersten, 2017). Therefore, the turbulent boundary layer comprises of two layers.

The area above the viscous sublayer is the frictional layer, where viscosity does not influence the flow and the fluid has a turbulent fluctuating motion. The velocity of the fluid in this region reaches the outer flow's velocity faster than a laminar boundary layer. This means that the velocity profile of a turbulent boundary layer is fuller, with the velocity gradient steeper than that of a laminar boundary layer. Recollecting equations 2.3 and 2.4, with a higher velocity gradient, the shear stress is higher, equating to higher skin friction. Figure 2-4 shows the connection between the Reynolds number and the skin friction coefficient. In this case, the Reynolds number

is given by equation 2.5 and the skin friction coefficient is given by equation 2.6, where F is the skin friction drag.

$$Re = UL/v \tag{2.5}$$

$$C_F = F/(\frac{1}{2})\,\rho\, U^2 S_w \tag{2.6}$$

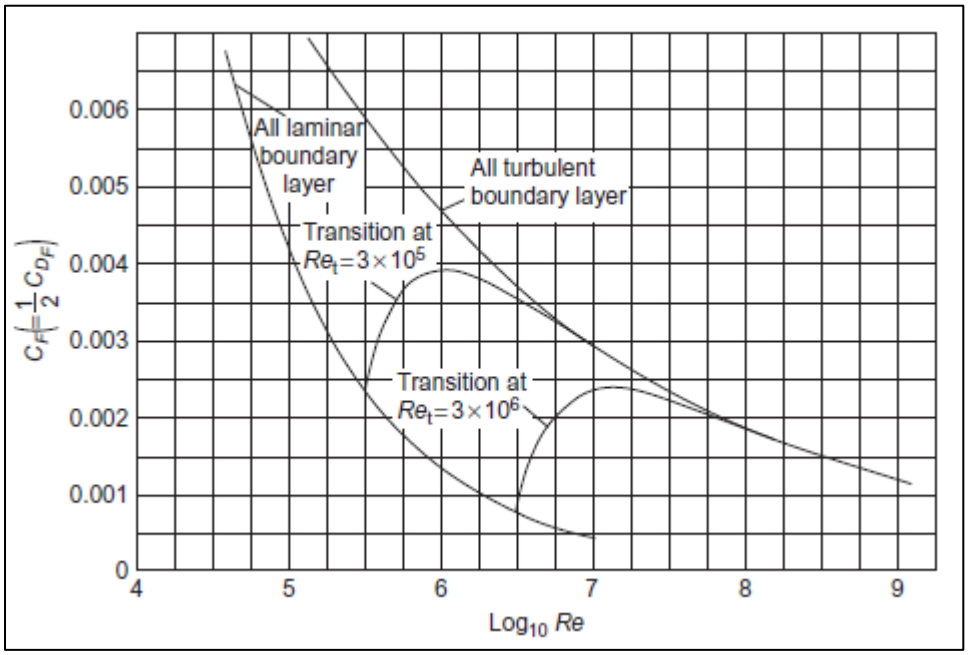

Figure 2-4: Skin friction drag coefficients for a flat plate (Houghton *et al.*, 2016)

When transition from laminar to turbulent flow is delayed, the amount of skin friction drag is reduced. Boundary layer suction can minimize skin friction drag by delaying the start of transition. In Section 2.3, the occurrence of boundary layer transition and how the turbulent boundary layer's progress can be managed and postponed are investigated.

2.3 Laminar-turbulent transition

The boundary layer transition region is the area where the boundary layer flow transforms from laminar to turbulent. Apart from the Reynolds number, the commencement of laminar-turbulent transition can be caused by several disturbances, also known as instabilities, in the flow. These include the wall curvature, a coarse surface, vibrations and the turbulence intensity of the inviscid outer flow (Schlichting & Gersten, 2017). The Reynolds number, where the laminar boundary layer becomes unstable and transitions to turbulent flow, is called the critical Reynolds number.

Boundary layer transition is a process that does not occur instantaneously. The point where transition starts, is recognized by an abrupt increase in velocity and boundary-layer thickness (Schlichting & Gersten, 2017). Receptivity is the initial stage of the transition process where disturbances in the outer flow, such as sound and turbulence, are transferred to the boundary layer as perturbations (Saric, 1992). The initial disturbances are small and, in many cases, unmeasurable in the boundary layer. According Zahn (2017), the most critical instability for an unswept wing is the Tollmien-Schlichting (TS) waves.

The Tollmien-Schlichting waves form when the outer flow disturbances are converted into simple harmonic waves. These waves are two-dimensional and proceed downstream in the streamwise direction (Gad-El-Hak, 2000). Amplification of these waves occurs on account of the no-slip condition at the wall (Van de Wal, 2010). As the amplitude of these waves increases, they evolve into three-dimensional waves in the spanwise direction and, in due course, they collapse into turbulence.

Boundary layer transition can take several routes after the initial disturbances to the flow, depending on the intensity and character of these disturbances. These processes will be discussed in sections 2.3.1, 2.3.2 and 2.3.3.

According to Houghton *et al.* (2016), when external stimuli are present near the boundary layer, the first reaction to the stimuli is linear oscillations in the boundary layer. Only a slight amplification of the oscillations exists during the linear stage, and the growth of the disturbances is weak. Secondary instabilities grow from the linear stage that exhibits non-linearities. The non-linear stage takes place with an increase in amplitude compared to the linear stage (Saric, 1992). The transition process progresses swiftly once the non-linear stage commences due to the intensity of the secondary instabilities.

2.3.1 Natural transition

Natural transition takes place when the turbulent intensity of the outer flow is less than 1%. In other words, the disturbances in the environment are relatively weak. The disturbances related to natural transition include the T-S wave and cross-flow instabilities (A Medida, 2014).

Turbulent spots develop when the velocity fluctuations are amplified sufficiently, after which the turbulent spots increase in size and move downstream. The rate at which the turbulent spots are produced, is called intermittency. These turbulent sections grow and after some time, turn into a fully turbulent boundary layer where the transition process is complete (A Medida, 2014).

2.3.2 Bypass transition

If the free-stream turbulence level is higher than 1%, the linear stage is omitted from the transition process and substituted with the non-linear stage (Langtry, 2006). This is called bypass transition. The disturbances that lead to bypass transition include surface roughness, acoustic perturbations and free-stream vorticial disturbances.

2.3.3 Separated flow transition

When the increase of the boundary layer thickness is too steep, decelerated fluid particles are forced outward and flow separation may occur (Katz, 2003). When separation of the laminar boundary layer takes place, transition occurs in the shear layer of the separated flow. This transition is due to the inviscid instability system (Langtry, 2006). The disturbances that lead to separated flow transition include an adverse pressure gradient, tripwire and when the leading edge of an airfoil has a small radius. After separation, reattachment can occur in the form of a separation bubble (Gleyzes *et al.*, 1984). The Reynolds number range in which the JS3 operates, ensures that transition will most likely occur through natural transition or separated flow transition, with the formation of a laminar separation bubble (Thomas & Milgram, 1999).

The occurrence of a laminar separation bubble begins when the boundary layer transitions to turbulent flow. A separation bubble forms when this turbulent flow comes into contact and reattaches to the surface (Houghton *et al.*, 2016). This occurrence is visible in Figure 2-5.

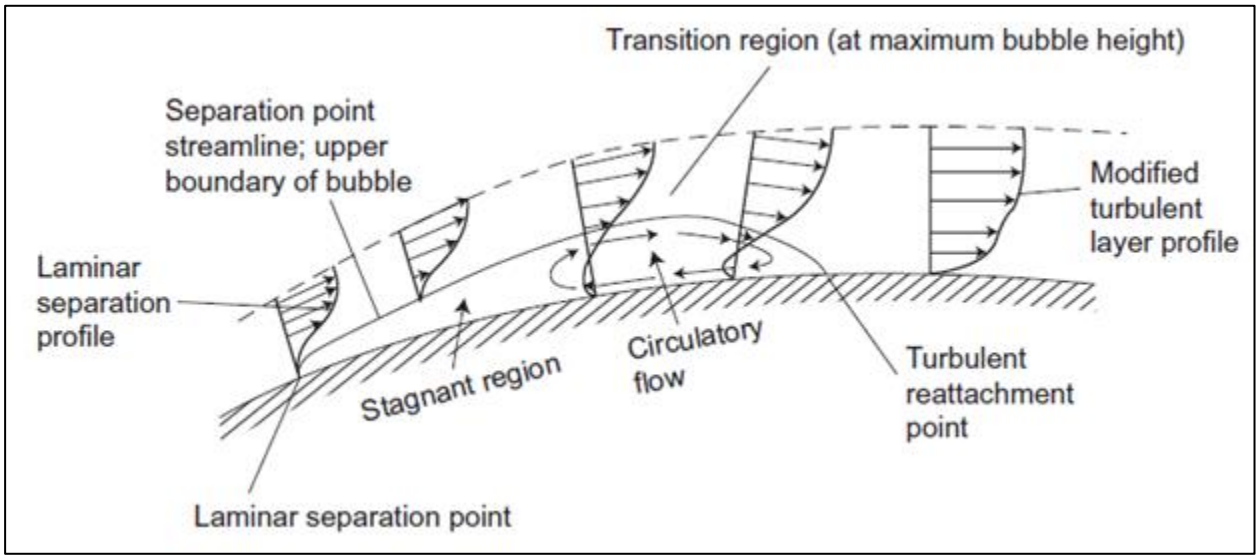

Figure 2-5: Laminar separation bubble (Houghton *et al.*, 2016)

2.4 The influence of boundary layer suction on transition

Boundary layer suction is a method used to postpone transition and to delay separation of the boundary layer (Gad-El-Hak, 2000). Removing a piece of the turbulent boundary layer delays separation of the boundary layer; an action that requires a substantial amount of energy (Van de Wal, 2010). Transition, on the other hand, is postponed when suction is applied when the boundary layer is laminar. By delaying transition, separation is also delayed.

The curvature of the velocity profile changes when fluid is removed from the boundary layer through boundary layer suction. The laminar flow control methods that are utilized to alter the curvature of the boundary layer velocity profile, are called stability modifiers. Alteration of the velocity profile with these stability modifiers keeps the linear development of unstable waves to a minimum, and improves the stability characteristics of the boundary layer (Gad-El-Hak, 2000).

The boundary layer momentum equation indicates which variables (stability modifiers) influence the curvature of the velocity profile or, in other words, the flow stability and its opposition to separation. The streamwise boundary layer momentum in two dimensions is shown below, where the variables on the left side of equation 2.7 are the stability modifiers (Gad-El-Hak, 2000).

$$\rho_w v_w \frac{\partial u}{\partial y}\Big|_{y=0} + \frac{\partial p}{\partial x}\Big|_{y=0} - \frac{\partial \mu}{\partial y}\Big|_{y=0} \frac{\partial u}{\partial y}\Big|_{y=0} = \mu \frac{\partial^2 u}{\partial y^2}\Big|_{y=0} \tag{2.7}$$

For the velocity profile to become negative, wall suction (v_w) and the pressure gradient ($\frac{\partial p}{\partial x}$) must be negative, and the viscosity ($\frac{\partial \mu}{\partial y}$) must be positive. All of these will have a positive influence on the velocity profile and reduce the amplification of unstable waves (Gad-El-Hak, 2000).

2.5 Boundary layer suction and drag

Before discussing the relationship between boundary layer suction and drag, the definition and different types of drag that can be influenced by boundary layer suction must be considered. Drag reduction of high-performance aircraft is an ongoing struggle for designers. Drag is the aerodynamic force opposing the direction of the velocity vector of a moving body, and the reduction in drag is directly correlated to an increase in performance.

Drag generates a resisting force that acts on the moving object. The two main components of drag are (1) skin friction drag, and (2) pressure or form drag. An airfoil moving through fluid has both skin friction and pressure drag; Figure 2-6 demonstrates the normal pressure and tangential stress (McCormick, 2009). The amount of drag an object will experience, is expressed by an equation containing the dimensionless coefficient of drag, C_D, as can be seen in equation 2.8 (Young, 1989).

$$D = \frac{1}{2}\,\rho V^2\, SC_d \tag{2.8}$$

In this equation, D is the drag created by the moving body, ρ is the fluid density, V is the velocity of the moving body relative to the air, S is the reference area of the body and C_d is the drag coefficient. The descriptions of skin friction drag and pressure or form drag are discussed in 2.5.1 and 2.5.2, respectively.

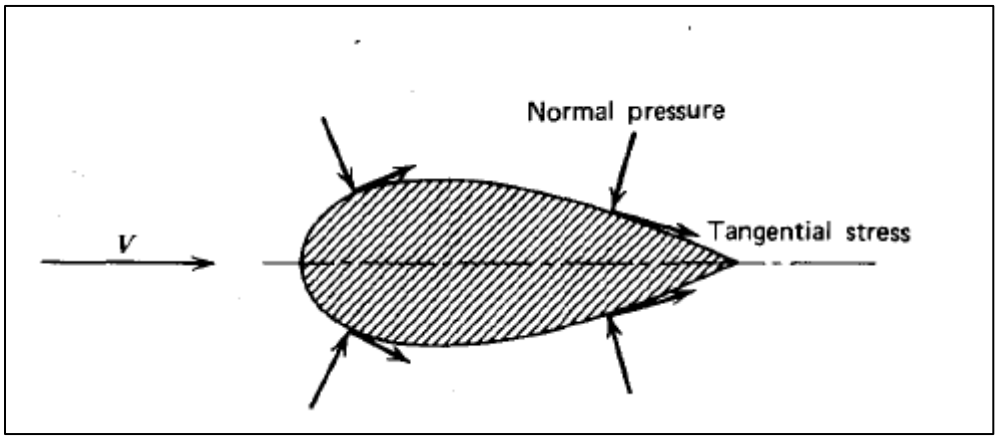

Figure 2-6: An airfoil with skin friction and pressure drag (McCormick, 2009)

2.5.1 Skin friction drag

When viscous forces act in the same direction as the fluid flow over the outside of the body, the outcome is skin friction drag (McCormick, 2009). The boundary layer starts developing at the leading edge of an airfoil as laminar flow. Boundary layer thickness grows as the fluid flows over the airfoil. After some distance, the flow becomes unstable and unable to withstand the

disturbances from surface roughness and instabilities in the free-stream flow. When instabilities occur, the boundary layer transition to turbulent flow, which is related to an irregular thickening of the boundary layer. If transition occurs, the skin friction drag increases.

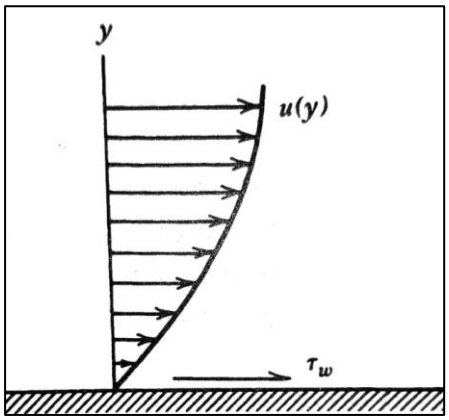

Figure 2-7: Viscous flow adjacent to a surface

The equation for fluid viscosity can be seen in equation 2.9. Shear stresses are a function of the viscosity (μ) of the fluid, as well as the velocity gradient (du/dy).

$$\tau = \mu\left(\frac{du}{dy}\right) \tag{2.9}$$

2.5.2 Pressure drag

A body that encounters skin friction drag will also encounter drag from the arrangement of pressure acting perpendicular to the body's surface. The force resulting from the static pressure, acting perpendicular to the surface of the moving object and in the direction of drag, is known as pressure drag (McCormick, 2009).

The Reynolds number has a substantial influence on pressure drag. The reason for this is that when a fluid moves past an enlargement in the cross-section of a body where the static pressure is minimum, the momentum of the fluid is inadequate to move against the positive pressure gradient. This creates a separated flow region past the enlargement and results in high-pressure before the enlargement, and a low-pressure trailing the enlargement. Therefore, high form drag is experienced.

When the Reynolds number is higher, laminar-turbulent transition occurs before boundary layer separation can take place. The momentum of a turbulent boundary layer is higher than that of a laminar boundary layer, which means the attached boundary layer is prolonged past the enlargement of the body.

2.5.3 Profile drag

Profile drag is the combination of skin friction and pressure drag. According to Jonker (2011), the wing profile drag produces about $53\ \%$ of the overall drag at high speed, and the glider airfoils operate between the Reynolds number range of 0.5×10^6 and $3\ \times 10^6$. In this Reynolds number range, the boundary layer can undergo different transitional behaviours. The first is the laminar-turbulent transition at the pressure recovery region. Secondly, a laminar separation bubble can exist on the wall when the laminar flow separates from the wall and reattaches, trailing the separation zone as turbulent flow (Jonker, 2011).

For small Reynolds numbers (below 10^4), the boundary layer will not reattach after separation. When the Reynolds number is large, transition of the boundary layer occurs without any separation (Jonker, 2011). The laminar separation bubble forms in the Reynolds number range between $10^4 < Re < 10^5$ (Gad-El-Hak, 2000).

At a Reynolds number of $Re = 1 \times 10^5$, the skin friction drag over a smooth surface is roughly four times greater when the flow is turbulent instead of laminar (Thomas & Milgram, 1999). Thus, it is paramount to keep the boundary layer laminar to create an airfoil with the least amount of drag possible. Form drag is dominant when the boundary layer is separated (Van Dam, 1999). Therefore, form drag can be reduced by delaying the start of separation from the surface.

2.5.4 Drag and boundary layer suction

Increasing the region of the laminar boundary layer through suction is not the only factor that should be acknowledged when examining drag. By stabilizing the boundary layer, the local skin friction increases due to the fuller boundary layer profile (Spalart & McLean, 2011). However, when the boundary layer is stabilized and the laminar flow region increased, the amount of skin friction due to a turbulent boundary layer is reduced. Even though the skin friction drag is increased slightly in the laminar boundary layer, the overall drag is much less than it would have been from a larger turbulent flow region.

Furthermore, a laminar boundary layer produces less pressure drag. The boundary layer thickness increases when transition to a turbulent boundary layer has taken place and an increase in pressure drag ensues. The increase in pressure drag occurs on account of the outer flow resisting displacement because of a larger boundary layer thickness (Van de Wal, 2010).

2.6 Boundary layer suction

2.6.1 Previous research on boundary layer suction

Prandtl conducted a study in 1931 on boundary layer suction and separation on a venturi tube type model with an adverse pressure gradient after the neck of the model (Braslow, 1999). His findings included that the decelerated fluid particles are removed from the boundary layer before separation can occur. The resulting non-separated flow after suction is applied after the neck of a diffusor, can be observed in Figure 2-8 (c). When no suction is applied to the side of the wall, as can be seen in Figure 2-8 (a), separation is apparent. When suction is present at the upper wall of the diffusor Figure 2-8 (b), the flow adheres to the surface, and the same is true when suction is applied to both walls, as depicted in (c) (Schlichting & Gersten, 2017).

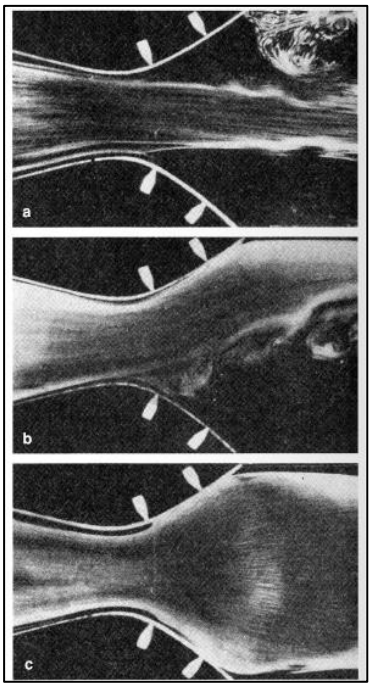

Figure 2-8: (a) Separation, (b) Suction at the upper wall of the diffusor, (c) Suction on both walls of the diffusor (Schlichting & Gersten, 2017)

The first person to propose that boundary layer suction can extend the laminar flow over a surface, was B.M. Jones in 1928 (Carmichael, 2002). Boundary layer suction research started in the 1930's and 1940's by experiments conducted in wind tunnels. In 1939, researchers from the National Advisory Committee for Aerodynamics (NACA) tested the effect on transition of applying suction through slots. During these experiments, it was found that laminar flow is possible for a Reynolds number of up to 7 million, which was unusually large at that time. In 1941, the first flight experiments were conducted by installing suction slots on different chord lengths of a test panel on a wing of a B-18 (Braslow, 1999).

Boundary layer suction was first used on gliders by Dr. August Raspet from 1949 to 1952 by applying a control device to the leading edge of the wing for aerodynamic research (Carmichael, 2002). There were also boundary layer suction studies conducted in 1964 with discouraging results since laminar flow has already been achieved over 70 percent of the chord, and it was not necessary to pursue further improvement at that time (Carmichael, 2002). The impact of suction on the overall performance of a glider was determined in 1977, and the glide ratio was improved from 90 to 100 (McMasters, 1977). Loek Boermans conducted studies at Delft University of Technology (Boermans, 2006), and concluded that the glide ratio of a Standard Class glider could possibly be improved from 43 to 60 when suction is applied. A significant improvement in the performance of gliders is thus possible when implementing boundary layer suction.

Several components influence the efficacy of boundary layer suction. These include the suction pressure, the position and size of the suction holes, the Reynolds number and the boundary layer thickness (Kulkarni *et al.*, 2018). These concepts will be explained in sections 2.6.2 to 2.6.5.

2.6.2 Suction coefficient

The aim of boundary layer suction is to extend the point of transition with the minimum amount of suction force. This will reduce the momentum loss and therefore minimize skin friction (Gad-El-Hak, 2000). The momentum integral equation for steady, incompressible flow with suction ($v_w < 0$) is shown below in equation 2.10.

$$\frac{C_f}{2} = \frac{d\delta_\theta}{dx} + \frac{|v_w|}{U_0} \tag{2.10}$$

The suction coefficient, C_q, is the last term in equation 2.10. The second term in the equation is proportional to the momentum loss when removing the fluid with suction (Gad-El-Hak, 2000). Skin friction increases with an increase in the suction coefficient, C_q. It was found that, although the skin friction is increased with an increase in C_q, the overall drag is reduced due to the location of transition being extended toward the trailing edge of the airfoil, resulting in less turbulent flow (Shi *et al.*, 2015).

2.6.3 Suction hole size and angle

The size of the suction holes has an influence on the performance of boundary layer suction. A study was conducted by Shi *et al.* (2015) to determine what effect the hole width has on transition and the performance of suction. The hole size influences the suction mass and, in the study, they found that the initial increase in hole size reduced the boundary layer thickness. There was also

an initial reduction in skin friction drag and only started to increase after a certain width has been reached (Kulkarni *et al.*, 2018).

Research was also conducted to determine what the best angle for boundary layer suction would be. Huang and Hauser concluded that boundary layer suction implemented at 90^o has the most noteworthy positive influence on the lift coefficient (Huang *et al.*, 2004).

2.6.4 Suction hole chord location

Numerous studies have investigated the influence of the position where boundary layer suction is implemented. One of these studies was conducted on the influence the suction position has on the length of laminar flow (Shi *et al.*, 2015). This study concluded that the region of the laminar boundary layer increases from a location close to the leading edge to some point where the transition location does not alter. When boundary layer suction is implemented beyond this point, the location where transition occurs is close to where natural transition occurs (Shi *et al.*, 2015). Even though the location of transition stays the same, the transition process is prolonged compared to natural transition. It is viable to say that boundary layer suction has little impact once the Tollmien-Schlichting waves grow to their full extent.

The coefficient of lift increases when boundary layer suction is implemented at the location before natural transition occurs (Shi *et al.*, 2015). The skin friction drag coefficient reduces at first but, past a certain point, there is an increase as the point where suction is applied moves downstream. The boundary layer thickness is reduced when boundary layer suction is applied at the correct chord location, resulting in a lower pressure drag coefficient (Shi *et al.*, 2015)

2.6.5 Suction velocity

Studies on the NACA 0012 airfoil were conducted by Yousefi *et al.* (2013) by considering three suction amplitudes, namely 0.1, 0.3 and 0.5. Suction amplitude is the correlation between suction velocity and free-stream velocity. The study concluded that when the suction amplitude is increased to a certain value, drag reduces (Yousefi *et al.*, 2013). In this study, it was also found that when the suction amplitude is too small, boundary layer suction does not affect the boundary layer.

2.7 Boundary layer suction application on the vertical stabilizer

This project focuses on the tail assembly of the glider, also known as the aircraft's empennage. The empennage consists of stabilizing surfaces, and the fundamental purpose is to create stability and control for the airplane. These stabilizing surfaces consist of a static surface and a moveable control surface.

The vertical stabilizer, or fin, and the rudder provide directional stability in the z-axis, also called the yaw axis. The horizontal stabilizer, or tailplane, and the elevator provide longitudinal stability. The control and stabilizing surfaces are illustrated in Figure 2-9 (Talay *et al.*, 1975). The control surfaces are the moving surfaces responsible for initiating an aerodynamic force and changing the airplane's course. The rudder provides yaw control and the elevator delivers pitch control (Talay *et al.*, 1975). Boundary layer suction will be applied to the vertical stabilizer to reduce the drag produced by the surface.

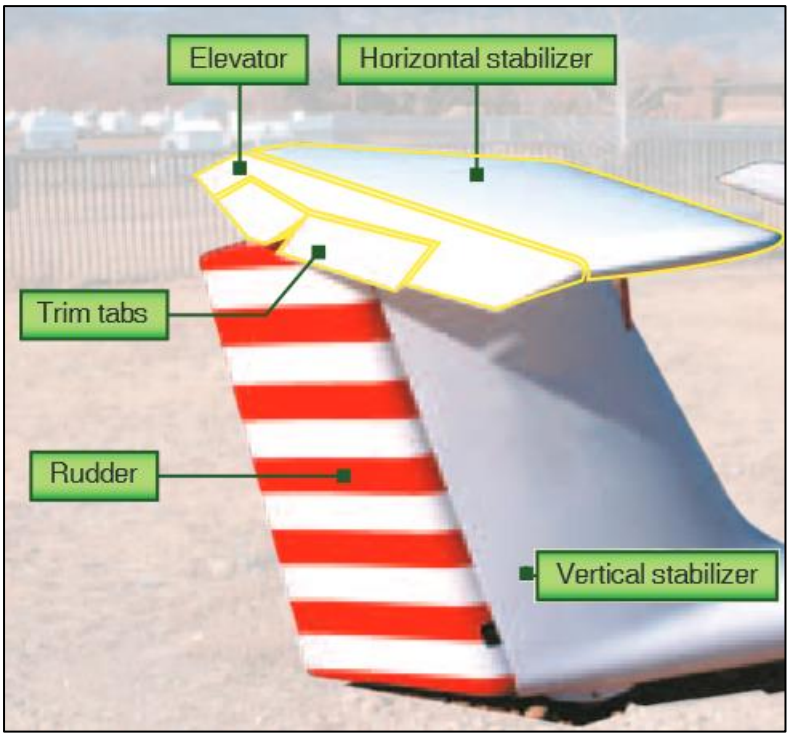

Figure 2-9: Sailplane empennage components (FAA, 2003)

2.8 Boundary layer suction challenges

The challenges for the implementation of boundary layer suction are highlighted in this section. The influence of insect contamination on the implementation of boundary layer suction is investigated in section 2.8.1, section 2.8.2 includes manufacturing difficulties that might appear and in section 2.8.3, the impact of the weather on a boundary layer suction system is discussed.

2.8.1 Insect contamination

The surface of a glider must be kept smooth in order to prevent detrimental instabilities on the boundary layer due to surface roughness. The impact insect contamination has on the boundary layer, is influenced by the population density of insects. Insects occur in high densities at low altitudes and there is a reduction in insect density with an increase in altitude level (Joslin, 1998). Methods to eliminate or prevent insect contamination include mechanical scrapers, a deflector that deflects the insects away from the surface and a cover that can be dissolved by fluid or a continuous fluid discharge (Joslin, 1998). The JS3 is equipped with a mechanism called the bug wipe, which prohibits the build-up of insects on the leading edges of the wings.

The majority of these mechanisms must be implemented on the leading edge of a wing, since this is the part of the surface that first come into contact with insects as they pass the glider. Boundary layer suction is usually implemented near the trailing edge, and insect contamination during flight will only affect the suction system when the boundary layer has been compromised.

2.8.2 Manufacturing and maintenance

According to Joslin (1998), surface roughness during the manufacturing of aircraft was a problem during the 1940's to 1960's that hindered realizing the application of laminar flow control. Manufacturing methods and surface smoothness have improved considerably from the 1990's, resulting in the implementation of laminar flow control methods on aircraft (Joslin, 1998). There are several issues in maintaining laminar flow control systems, such as the need for spare parts, cleaning contamination of the suction system and problem identification during failure of the system.

2.8.3 Weather

Specific weather conditions like rain, wind and ice influence laminar flow. Flight tests were conducted on an F-94A aircraft where wind gusts influenced laminar flow. However, when the gusts passed, laminar flow was regained. During these same flight tests, it was observed that rain influences transition but, when the rain subsided, laminar flow was again acquired (Pfenninger & Groth, 1961). Aircraft experience a loss of laminar flow when making contact with

clouds, but cloud encounters are infrequent and do not result in a substantial loss in performance (Braslow, 1999). It is safe to say that aerodynamic improvements from boundary layer suction still exist after encounters with these weather conditions.

CHAPTER 3: NUMERICAL MODELLING OF BOUNDARY LAYER SUCTION WITH COMPUTATIONAL FLUID DYNAMICS (CFD)

In Chapter 2, boundary layer suction was discussed, including the theory behind the concept and the feasibility thereof. It is now imperative to find a tool to illustrate and calculate the influence of boundary layer suction on the growth of the boundary layer and the effect suction has on laminar-turbulent transition. In Chapter 3, the suitability of computational fluid dynamics (CFD) for the simulation of suction on airfoil sections is investigated.

Laminar-turbulent transition is a crucial phenomenon in fluid mechanics. After transition takes place, the skin friction between the fluid and the wall increases due to the presence of a turbulent boundary layer, resulting in a drag increase. It is therefore crucial to be capable of predicting the location where transition takes place because it has an influence on the accuracy of the aerodynamic parameters. Transition prediction is a possibility with CFD transition modelling and may be used when modelling boundary layer suction. For accurate CFD solutions, all boundary layer phenomena must be modelled correctly, including but not limited to transition, turbulent flow and separation bubbles.

Various CFD transition models exist and the goal now is to determine which model is suitable to use when working with low-speed aerodynamics. In Chapter 3, an overview of numerical modelling connected to the application of boundary layer suction is given.

3.1 Introduction to CFD

Computational fluid dynamics was previously only used by academics or trained specialists, but has become available as commercial software for research, design and utilization in the engineering practice to solve complex problems. CFD integrates fluid mechanics, mathematics and computer science and is mainly devoted to fluids in motion. The complex flow phenomena that occurs when a fluid moves around or within an object, as well as theoretical and experimental results, can be better understood and interpreted with CFD (Tu *et al.*, 2008).

The characteristics of a viscous fluid in motion are described with mathematical equations called the Navier-Stokes equations, by implementing numerical techniques. The fluid flow governing equations are based on the conservation laws of physics and are approximated by using finite difference, finite volume or finite element methods. These equations are solved by using iterative solvers to find the solution to fluid-flow problems.

3.2 Drag prediction with CFD

A lot of research has been devoted to drag prediction. Accurate aerodynamic drag prediction is an integral part of aircraft design, and drag is a quantity related to the performance of aircraft. Drag comprises of skin friction and pressure drag; both terms were discussed in section 2.5. The prediction of drag is elaborated on in section 3.2.

When examining the aerodynamic forces which act on a body submerged in a fluid, the equation for the total force is found by integrating over the normal and tangential forces (Van Dam, 1999). The equation for drag, the force opposing the direction of the free-stream velocity vector, from the body's perspective, is illustrated in equation 3.1. Here, the pressure is p, n is the components of the unit vector normal to the body, S_{body}, and τ is the viscous stress tensor.

$$D = \iint_{S_{Body}} \left(-pn_x + \tau_{xx}n_x + \tau_{xy}n_y + \tau_{xz}n_z\right) dS \tag{3.1}$$

Several factors must be considered for accurate drag prediction in CFD, as listed in sections 3.2.1 to 3.2.8.

3.2.1 Geometry

Geometrical consistency is needed to prevent inaccurate drag predictions. Care must be taken during the process of defining the geometry to ensure that it is geometrically similar to the body being used in experiments.

3.2.2 Mesh

Fine meshes deliver better and more accurate results compared to coarser meshes. An adequate mesh is created when the flow features around the solid body are captured and the physics involved is accurately modelled. The problem with fine meshes is that creating a fine mesh is time-consuming and computationally intensive. Time limitations during the design and development process can be the cause for users to not use fine meshes. Mesh resolution studies by Oskam and Slooff (1998) concluded that drag converges to a single value when the mesh is fine enough.

Having mesh independent solutions ensure results obtained are repeatable and accurate enough for the specific simulations. The inputs used to find a mesh independent solution are then used to perform experimental investigations, which is critical for design (Almohammadi *et al.*, 2013).

The mesh size in the nearfield region close to the body must be fine due to the influence it has on the accuracy of the nearfield force and the far-field wake predictions (Oskam & Slooff, 1998).

The mesh of the wake must be fine enough to capture flow developments and to calculate far-field and wake-based forces accurately (Van Dam, 1999).

Several mesh types are available to use in CFD programs and are divided into two main categories: Structured and unstructured meshes. Subdivisions of these categories include quadrilateral and triangular two-dimensional and three-dimensional meshes, tetrahedral meshes, hexahedral meshes, polyhedral meshes and prism meshing consisting of triangular of quadrilateral prisms (Sadrehaghighi, 2020).

The nodes of a structured mesh have an equal number of elements surrounding them. Creating a structured mesh can be time-consuming because the domain must be divided manually into numerous blocks. The nodes of unstructured meshes, on the other hand, are connected irregularly and this type of meshes are more flexible and automated than structured meshes (Sadrehaghighi, 2020).

Hexahedral meshes are used when the fluid flow moves perpendicular to a surface. The possibility to generate hexahedral meshes for complex geometries does not always exist due to rigidity of the mesh, and the element size must be reduced to successfully acquire accurate results (Sosnowski *et al.*, 2017). Tetrahedral meshes consist of the simplest elements and, in contrast to hexahedral meshes, are easy to generate when the geometry is complex. The downside of using tetrahedral meshes is that more elements must be used because the cells must not be overly stretched.

The advantages of hexahedral and tetrahedral meshes are combined in the polyhedral mesh, and the disadvantages of both mesh types are conquered with polyhedral meshes (Sosnowski *et al.*, 2017). The polyhedral mesh, like the tetrahedral mesh, has many adjacent cells that increase the precision of the answer but is not as delicate in terms of stretching. Polyhedral meshes can, in some instances, have more accurate solutions than hexahedral meshes due to the large number of adjacent cells (Sosnowski *et al.*, 2017).

3.2.3 Numerical solution (solver)

The CFD user must acquire the necessary knowledge of processes like solution control and monitoring to utilize the solver features optimally. A suitable iterative solver must be chosen for the flow problem as well as the relevant discretization scheme. Most CFD packages use the finite volume method as the solution technique. This means that the computational domain is split up into smaller control volumes. The solution domain consists of a limited amount of small control volumes in correlation with the cells of a computational mesh.

STAR-CCM+ is a flow solver and uses finite volume discretization; a method of converting the mathematical model into a structure of algebraic equations by discretizing the governing equations in space and time. The pre-processing, numerical solving of the simulation, as well as the post-processing, can be done on STAR-CCM+. The computer aided design (CAD) can be done on another program and imported as needed. STAR-CCM+ is used to simulate internal and external fluid flow, for several different kinds of fluid and over a broad range of flow regimes. STAR-CCM+ finds the solution to the conservation equations for mass, momentum and energy for incompressible and compressible fluid flows.

3.2.4 Boundary conditions

The boundary conditions of all the relevant surfaces in the computational domain must mimic the real-world flow problem. For internal and external flows, the main difference lies in the top and bottom boundaries. For internal flow, the fluid is confined inside a domain of walls. External flow can take inflow or outflow boundary conditions. It is crucial to let the fluid dynamics develop fully over the span of the computational domain. For internal flow, the flow must be fully developed at the exit. For external flow, the development of the wake behind the body must be encapsulated. The height of the domain for an external case must be at a far enough distance to eliminate the influence the boundary has on the surrounding fluid, but not exceed the calculation capabilities of the computer (Tu *et al.*, 2008).

3.2.5 Flow classification

Factors that influence the flow classification include the velocity and compressibility of the fluid. The Mach number for subsonic flow is smaller than 1 (Chattot & Hafez, 2015), and the assumption for incompressibility is based on the Mach number. When the flow is subsonic and the aircraft's speed is below 150m/s, the air may be treated as incompressible because the effect of changes in density cause only small, insignificant changes in the results (Talay *et al.*, 1975). This means that the flow can be idealized and the assumption is made that density is constant.

3.2.6 Convergence

Convergence can be reached by monitoring the imbalances in the numerical calculations of the flow properties, also known as residuals. The solution has converged when the residual values are less than the criteria for convergence. The convergence can be double-checked by using monitors of forces like lift and drag (Tu *et al.*, 2008). When the results of these aerodynamic monitors have stabilized, convergence has been obtained. Complex simulations will require more iterations before convergence will be reached. A successful solution will most likely have convergence and mesh independence.

In order to see where the mesh must be refined when the intermittency and residuals are too high, one can import a threshold into the mesh scene. An option is available in the $\gamma - Re_\theta$ transition model to use the Temporary Storage Retained function. If selected, the temporary storage is not cleared at the end of the iteration process. This enables the user to see where the residuals are too high; thereafter, a threshold of the residuals above a specific value can be created and imported into the mesh scene.

3.2.7 Laminar-turbulent transition

Transition from a laminar to turbulent flow regime is essential for accurate drag prediction. Extensive research has been conducted on transition prediction models for CFD due to the fact that the prediction of the location of transition has previously been a problem. It was found that transition models used together with Reynolds-averaged Navier-Stokes (RANS) solvers provided accurate drag predictions. Further discussion on turbulence models is done in section 3.2.8.

3.2.8 Turbulence model

Multiple studies have been conducted on turbulence modelling over the last few decades. Turbulent flow is unsteady and it would require a lot of computational resources to model these unsteady characteristics. Due to computational limitations in the engineering industry, a method called Reynolds Decomposition is used for turbulence modelling. The instantaneous variables of the Navier-Stokes equations are divided into a mean and a fluctuating part (Andersson *et al.*, 2011). In other words, the flow is defined by the mean velocity and turbulence properties. The turbulence variables are time-averaged to yield the Reynolds-averaged Navier–Stokes (RANS) equations. The RANS equations have an additional term for the Reynolds stresses when compared to the Navier-Stokes equations. This term must be modelled to close the governing equations.

Turbulence modelling has a compelling influence on accurate drag prediction. Much of the flows over aircraft are turbulent, which means that accurate turbulence modelling is crucial for aircraft design. Much progress has been made on turbulence model development for the RANS equations. It is crucial to apply a turbulence model to the correct flow problem for which it has been developed.

The $K - \omega$ turbulence model is a turbulent kinetic energy and dissipation-based equation model that uses wall functions. In contrast to the $K - \epsilon$ model, the $K - \omega$ model has enhanced performance when adverse pressure gradients are present in the boundary layers. The $K - \omega$ turbulence model does not require extensive amounts of memory and has good convergence with improved accuracy for internal flows (CD-Adapco, 2016).

The standard $K-\omega$ turbulence model shows sensitivity to free-stream inlet conditions. This model was modified by (Menter, 1994), resulting in the shear-stress transport (SST) $K-\omega$ turbulence model. This model usually resolves all viscous flows, and the turbulence model is used throughout the boundary layer (CD-Adapco, 2016).

3.3 Transition modelling with CFD

It is required to simulate the laminar-turbulent transition accurately when designing high-performance gliders. The transition usually occurs as a laminar separation bubble at low Reynolds numbers or subsonic flow. The turbulent flow reattaches trailing the separation bubble, causing the flow between the reattachment zone and the laminar flow in the front to recirculate.

The onset of transition can be predicted when a transition model is used in conjunction with a turbulence model. A transition model is required because transition cannot be predicted error-free by using a turbulence model alone. The two methods available regarding transition is the Turbulence Suppression model and the $\gamma - Re_\theta$ transition model. Transition is suppressed in a pre-defined region when using the Turbulence Suppression model, which means the position of transition must be known. Although this model is the fastest and least expensive, the location of transition is not always known.

The $\gamma - Re_\theta$ model is a correlation-based model that allows the user to solve two transport equations simultaneously (Langtry, 2006). The first is for transition onset momentum thickness Reynolds number, Re_{θ_t}, which is defined in the free-stream, and the second is the intermittency transport equation, γ. This model is more expensive but predicts the onset of transition adequately.

The $\gamma - Re_\theta$ transition model is dependent on the definition of $Re_{\theta t}$ from a correlation specified in the free-stream. The free-stream edge location must be defined before the value of $Re_{\theta t}$ can be specified, and this can be done in STAR-CCM+ by creating and assigning a user field function. The value of the field function in the free-stream is equal to 1, and equal to 0 inside the boundary layer (CD-Adapco, 2016). The free-stream is pre-defined in terms of the wall distance, namely $\$WallDistance > 0.005?\,1:0$. Subject to these terms, the function estimates that the boundary layer everywhere on the body is smaller than $5\ mm$. The user field function must then be assigned in the properties of the $\gamma - Re_\theta$ transition model under Free-stream Edge.

The turbulence model solves the boundary layer by the distance from the wall to the middle of the first cell of the boundary layer mesh (Hansen, 2014). As can be seen in equation 3.2, this distance is given by the wall y^+ value, with y being the distance between the wall and the first cell centroid, u^* being the reference velocity and v being the kinematic velocity.

$$y^+ = \frac{yu^*}{v} \tag{3.2}$$

The y^+ value must be smaller than 1 to better enable convergence of the $\gamma - Re_\theta$ model. The growth rate of the mesh, as well as the mesh density in the transition zone, must be small enough

to encapsulate the laminar separation bubble. The wall y^+ values increase in velocity, which means that the distance between the surface and the centroid of the first mesh cell must be reduced (Hansen, 2014).

3.4 Summary

Fluid flow in the boundary layer must be modelled carefully to find accurate results for lift and drag values. A conclusion can be drawn from the discussions in Chapter 3 that, due to its success at modelling boundary layer phenomena around aircraft, the RANS methods are feasible to use in the application of boundary layer suction. The SST $K-\omega$ turbulence model is a viable choice due to its low memory requirements and good convergence, as well as excellent accuracy for internal flows. For the transition model, a satisfactory option is the $\gamma - Re_{\theta}$ transition model. These models were implemented in STAR-CCM+ and are discussed in the upcoming chapters.

CHAPTER 4: TWO-DIMENSIONAL VERIFICATION AND VALIDATION

One of the methods used to assess the credibility of CFD simulations, is validation. Validation can only be done after verification of the CFD simulation. Verification is related to mathematics and computer sciences whereas validation is related to mathematics and physics. Verification can be explained in short as solving the equations correctly and validation as solving the correct equations.

The verification process include code verification and solution verification. Code verification is the means of deciding if the intended algorithms are implemented correctly by the code. Calculation verification, on the other hand, is the process of determining the accuracy with which algorithms solve mathematical-model equations. Some tools for solution verification include, but are not limited to, iterative convergence and spatial convergence.

During a steady state flow simulation, the simulation starts with uniform flow and is iterated in time until the steady state flow field is obtained – this is iterative convergence. The criteria to determine iterative convergence include convergence of residuals and convergence of results, these two concepts were first introduced Chapter 3.2.6. Two-dimensional iterative convergence was discussed in 4.3.1 and the typical residuals from STAR-CCM+ were also included.

Grid convergence must also be examined for verification to reduce the spatial discretization error. This involves carrying out the simulation on two or more consecutively finer grids. As the grid is refined, the discretization errors should asymptotically approach zero. A mesh independency study was conducted and the results of the study were shown in 4.4.1.

The validation process involves quantifying the uncertainty in the computational model and the solution of the model by using standard experimental data (L. Oberkampf *et al.*, 1998). Comparisons will therefore be made between the CFD code and benchmark experiments to determine if the model is a realistic representation of the real-world flow problem that is being solved (Tu *et al.*, 2008). The accuracy of the computational model is relative to experimental data, which is the best comparison to reality. It is only possible to validate a computational model for which there is experimental data available. After validation, the simulation model can be used for similar models under the same circumstances as the validated model. The objective of this validation study is to work towards obtaining confidence in utilizing the CFD program, with the objective being the application of boundary layer suction on the vertical fin of a sailplane.

The validation process was conducted for two-dimensional and three-dimensional cases. The two-dimensional validation was done by comparing results from STAR-CCM+, XFOIL and wind

tunnel experiments of the NACA-0018 airfoil. To validate the two-dimensional CFD model, the simulation setup of the two-dimensional airfoil was similar to the conditions of the experiments. This airfoil was simulated at angles of attack ranging from $0°$ to $16°$ in order to relate the aerodynamic coefficients from STAR-CCM+ with the values from XFOIL, and wind tunnel tests at the same angles of attack. The purpose of doing a two-dimensional validation is to have confidence in upcoming two-dimensional simulations regarding boundary layer suction. The solver utilized for the two-dimensional validation was STAR-CCM+. The transition model utilized for the validation process was the $\gamma - Re_\theta$ model, along with the $k - \omega$ SST turbulence model.

4.1 Validation requirements

It must be shown through validation that the aerodynamic coefficients are determined correctly through a broad range of angles of attack. This indicates that the transition location on surfaces is modelled accurately because the accuracy of the aerodynamic coefficients is dependent on the transition location. Laminar to turbulent transition will become crucial later when the natural transition location of the airfoil is altered by using laminar flow control. Another reason for the validation of aerodynamic coefficients, is to prove that occurrences in the boundary such as boundary layer growth and separation bubbles are modelled accurately.

According to Anderson (1995), the accuracy of the aerodynamic coefficient is affected by the mesh density and the mesh refinement around the solid body. A mesh dependency study was conducted to determine what the influence of the mesh density is on the accuracy of the aerodynamic coefficients. Since there are limits on computer resources as well as time, the mesh that provides results accurate enough compared to the numerical solution with the smallest number of cells, must be used. The mesh density is reduced until the difference in residuals of the coefficient of drag is below 0.003 (Yang & Schenkel, 2004), or less than $5\,\%$ (Murad *et al.*, 2004). If the correlation between STAR-CCM+, XFOIL and the experimental data is strong, it means that the transition location and the boundary layer are modelled well.

4.2 Two-dimensional validation setup

The NACA-0018 airfoil was chosen for the two-dimensional validation. The reason for this decision is because airfoil coordinates are readily available with sufficient wind tunnel data (Timmer, 2008). The wind tunnel data is used as baseline for the evaluation of XFOIL and CFD calculations.

4.2.1 Environmental parameters

The parameters implemented during the validation process are summarized in Table 4-1. The Reynolds number at which the two-dimensional simulations on the NACA-0018 airfoil was conducted, is 0.7×10^6 and the free-stream velocity was $40\ m/s$. The airfoil has a $0.25\ m$ chord length.

Table 4-1: Environmental parameters for two-dimensional validation on NACA-0018

Parameter	Value	Unit
Material	Air	-
Velocity, V	40	m/s
Density, ρ	1.225	kg/m^3
Pressure, P	101325	Pa
Chord Length, c	0.25	m
Dynamic Viscosity, μ	1.75×10^{-5}	m^2/s
Reynolds Number, Re	0.7×10^6	-

4.2.2 XFOIL setup

The environmental parameters used for the setup of XFOIL are shown in Table 4-1. The number of nodes of the airfoil on XFOIL was changed from 160 to 250 to increase the accuracy of the results. The panel distribution between the leading and trailing edge was also improved, as can be seen in Figure 4-1.

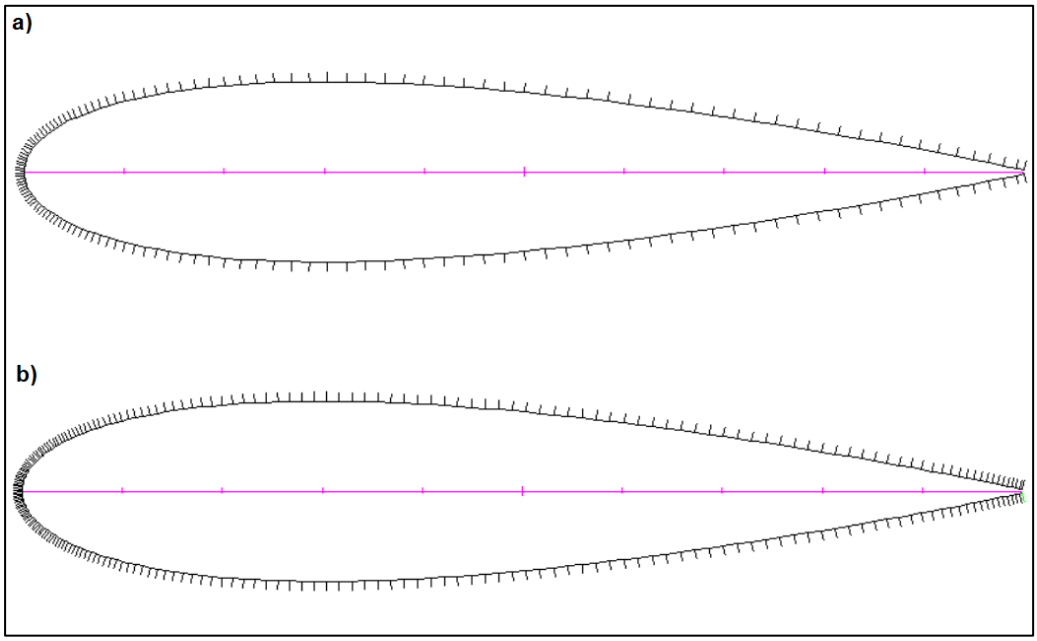

Figure 4-1: NACA-0018 panel distribution in XFOIL: a) Default panel distribution, b) Altered panel distribution

The turbulence intensity for the wind tunnel tests ranged from 0.02% at $10\,m/s$, to 0.07% at $70\,m/s$. Interpolating between these values give a turbulence intensity of $0.045\,\%$ at $40\,m/s$ with the corresponding n_{crit} value as 10. The value for n_{crit} was adjusted accordingly in XFOIL.

4.2.3 Grid configuration

The flow domain around the NACA-0018 airfoil is illustrated in Figure 4-2.

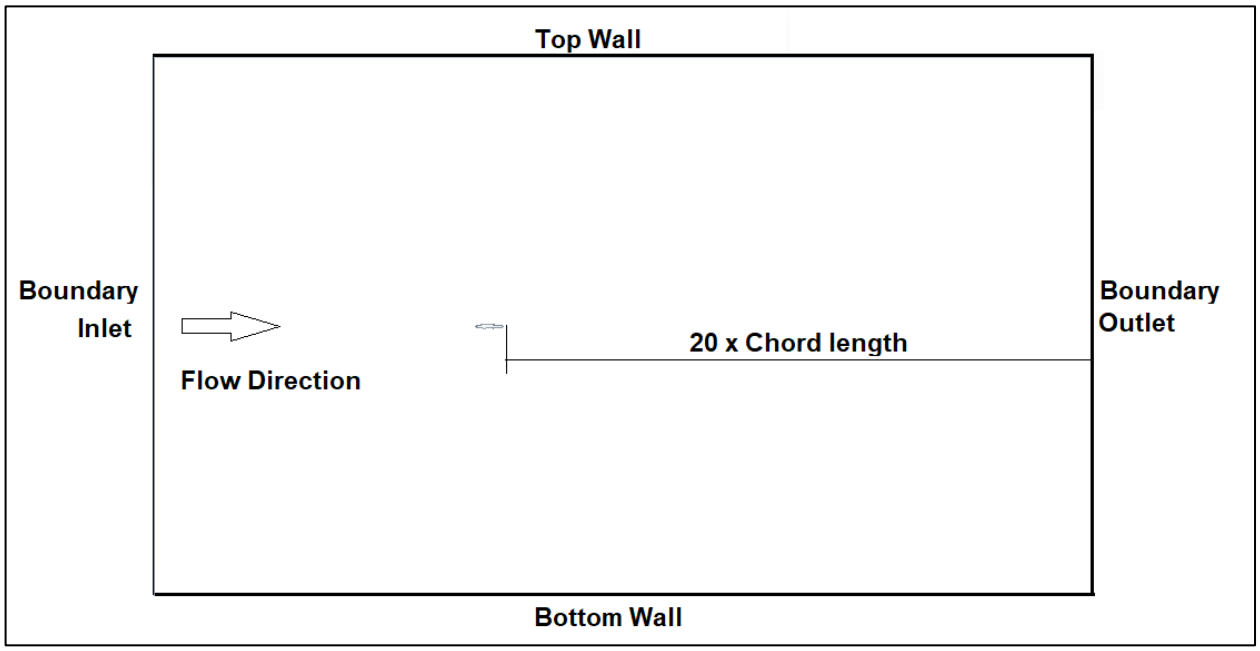

Figure 4-2: Two-dimensional flow domain configuration of the NACA-0018 airfoil

The geometry was created using a CAD program called NX from Siemens PLM Software by importing the coordinates of the airfoil as a .txt file. A sketch was made of the airfoil coordinates and then a solid was extruded from the sketch. The airfoil was scaled to have a chord length of $0.25\,m$, which means the cross-sectional area was $0.25\,m^2/m$ for the two-dimensional case. A rectangular solid representing the flow field was created in STAR-CCM+, and the airfoil was then subtracted from this solid. The domain size in Figure 4-2 is $8\,m$ in length, with the base of the domain $3\,m$ in front of the airfoil.

An automated mesh was used to simplify the method of attaining the two-dimensional mesh. The distribution mode of the prism layer was changed to wall thickness; a function which calculates the cell layer thickness distribution. The y^+ value for the first grid mesh around the solid body must be less than one. The distance from the surface of the solid body to the middle of the first cell adjacent the body, was set to $y_0 = 5\ \times 10^{-3}\,mm$ (El khchine & Sriti, 2017).

Volumetric and surface controls were used as custom controls set by the user to capture the flow more accurately. Volumetric controls were implemented on the leading edge over the airfoil where separation can occur at large angles of attack, as well as behind the trailing edge to capture the wake. Surface controls were utilized for mesh refinement on the airfoil and the trailing edge of the airfoil. The wake refinement control was customized by activating wake refinement in the trailing edge surface control, and a smaller mesh was used than in the wake volumetric control. The accuracy of the result was improved by incorporating custom controls, but a longer

computation time was also required. The mesh depicting the wake refinement volumetric control at a 5° AOA, can be seen in Figure 4-3 a). A cylindrical volumetric control was used on the leading edge to capture the flow accurately, as displayed in Figure 4-3 b), and the smooth transition of the boundary layers at the trailing edge is visible in Figure 4-3 c).

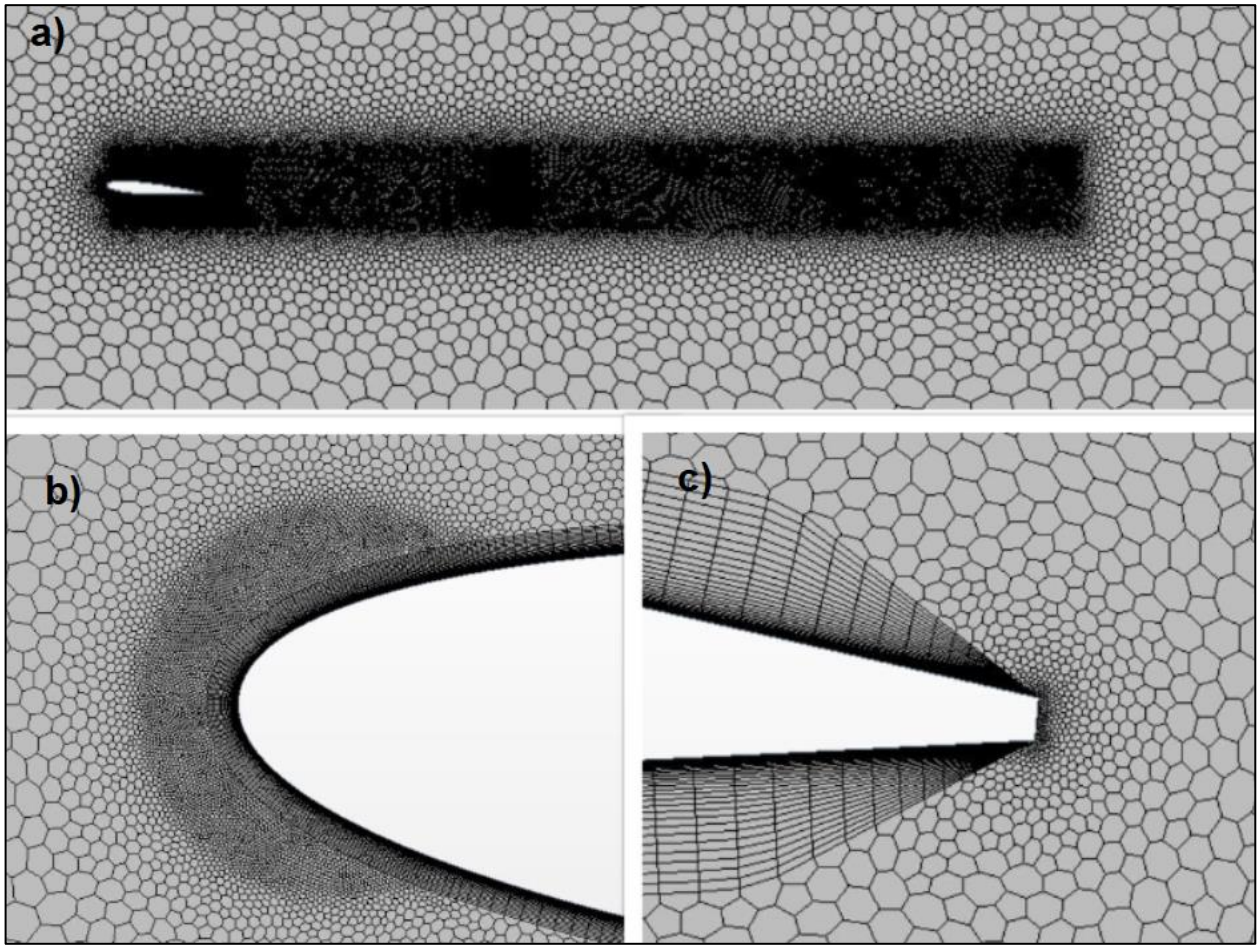

Figure 4-3: Mesh illustration of NACA-0018 at 5° AOA: a) Overview mesh, b) Leading edge, c) Trailing edge

4.2.4 Flow parameters and boundary setup

The physical conditions of the flow were compiled in Continua under Physics. The physics models selected for the CFD simulation model are shown below:

- Space: Two-dimensional
- Time: Steady state
- Material: Gas
- Flow: Segregated flow

- Equation of state: Constant density
- Viscous regime: Turbulent
- Reynolds-averaged Turbulence: $K-\omega$ SST turbulence
- Transition: $\gamma - Re_\theta$
- $K-\omega$ wall treatment: Low y^+ wall treatment

The free-stream edge under the $\gamma - Re_\theta$ transition model was defined by a field function where the wall distance was set to $3\,mm$. The air properties were set to standard sea level conditions with the density equal to $1.225 kg/m^3$.

The boundaries were assigned to each part surface under the Regions tab. The boundary type assigned to the inlet was a velocity inlet, and the velocity magnitude was set to $40\,m/s$. The boundary at the outlet was a pressure outlet with none of the variables changed, and the airfoil surface was set as walls.

4.3 Two-dimensional verification and validation procedure

It was necessary to accurately compute the aerodynamic coefficients through a broad range of angles of attack to validate the results (Oberkampf *et al.*, 1998). The aerodynamic coefficients used for this verification and validation, are the coefficient of lift and the coefficient of drag. The results obtained from XFOIL were compared to those obtained in the STAR-CCM+ two-dimensional simulations, as well as experimental data of the NACA-0018.

4.3.1 Convergence monitoring procedure

The residuals of a simulation represent the change in the equations after each iteration. When the residuals have stabilized, it is an indication of iterative convergence. The order of magnitude of the residual must typically be reduced by three or four for steady-state simulations. Residual monitoring is illustrated in Figure 4-4.

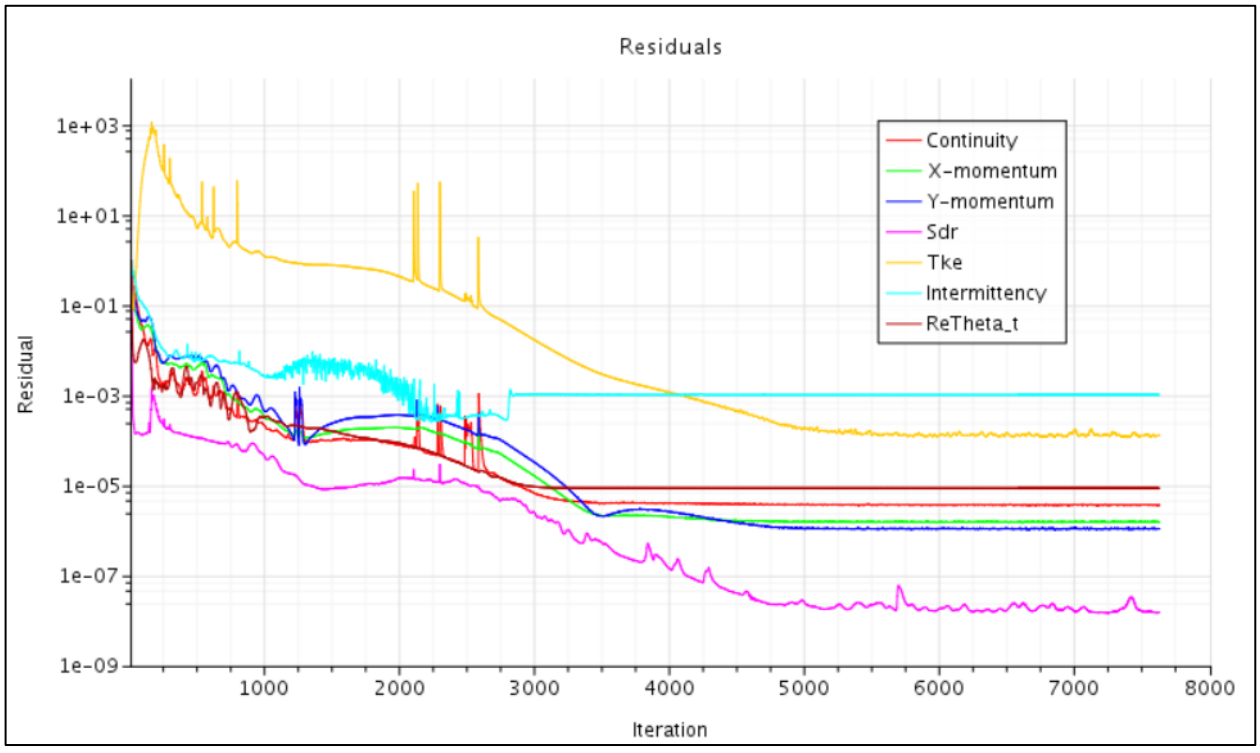

Figure 4-4: Typical residuals from STAR-CCM+ for convergence monitoring

Iterative convergence can also be established when looking at the convergence of graphs of aerodynamic coefficients with regards to iterations. Figure 4-5 indicates the convergence of typical lift and drag coefficient plots.

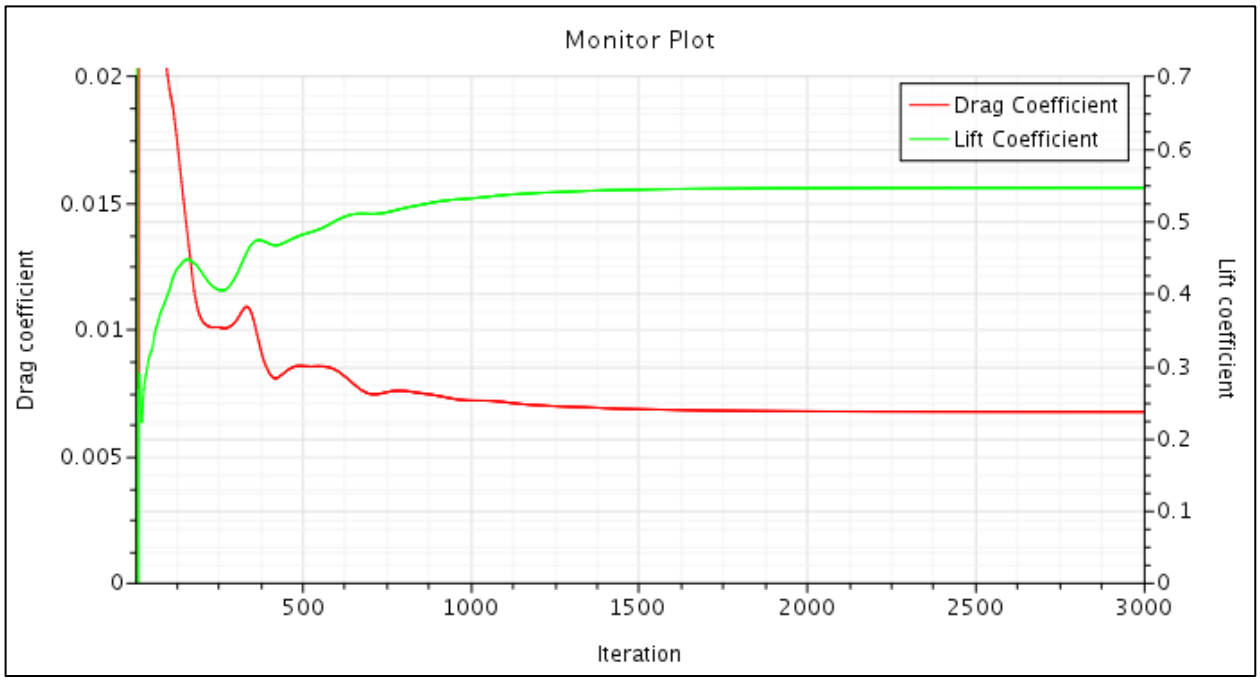

Figure 4-5: Lift and drag coefficient plots for convergence monitoring

4.3.2 Mesh independency procedure

The mesh density required for accurate results was established by performing a mesh independency study. The mesh was refined until the cell count does not have an influence on the accuracy of the results. The number of cells will increase as the mesh is refined and will require longer computing time, which is unwanted when efficiency is required. Minor differences in the results will exist after mesh independency is reached, but will be small and can be disregarded. The desired mesh resolution will keep an optimal balance between computational resources and the simulation time.

4.3.3 Transition prediction procedure

The location of transition on the NACA-0018 airfoil from the STAR-CCM+ results, was compared to the predicted transition location from XFOIL and the data collected from the wind tunnel tests conducted by Timmer (2008). XFOIL uses an envelope e^n transition prediction method, and the results from this method compare well with experimental data (Drela & Giles, 1987). XFOIL is thus a suitable tool for the validation of the transition location.

The transition location was found by examining the skin friction plot of the airfoil. This phenomenon occurs where there is a sudden change in the form of the plot. A boundary layer velocity vector plot also gives an adequate indication of the flow phenomena that takes place near the surface of the airfoil.

4.3.4 Procedure to obtain aerodynamic coefficients

Reports and plots were used for post-processing where quantities like lift and drag coefficients were computed and examined. The aerodynamic coefficient values from wind tunnel tests and XFOIL can be compared to the results from STAR-CCM+, and conclusions can be made from this comparison on the accuracy of the STAR-CCM+ model.

4.4 Two-dimensional validation results

The results obtained from the mesh independency study, as well as statements and discussions about the two-dimensional validation, are presented in section 4.4.

4.4.1 Mesh independency results

A mesh independency study was conducted on the NACA-0018 airfoil at a $0°$ angle of attack. This was done before the two-dimensional validation was performed to determine the required cell count for an accurate simulation. The drag coefficient value converged to a value of $C_d = 0.00932$, while the converged value for the lift coefficient was $C_l = 0.5077$.

From Figure 4-6 and Figure 4-7, it is evident that the values for the drag and lift coefficient are independent from 280 000 cells, and the assumption can be made that the accuracy of the results is adequate. The percentage error in the drag coefficient at 280,000 cells are $\%_{error} = 0.75\%$. To manage computational resources optimally without wasting time, the cells were kept at 280 000. The base size that results in a cell count of 280 000, is $30\,mm$. The prism layer has a total thickness of $3\,mm$, and the y^+ values are below 1.

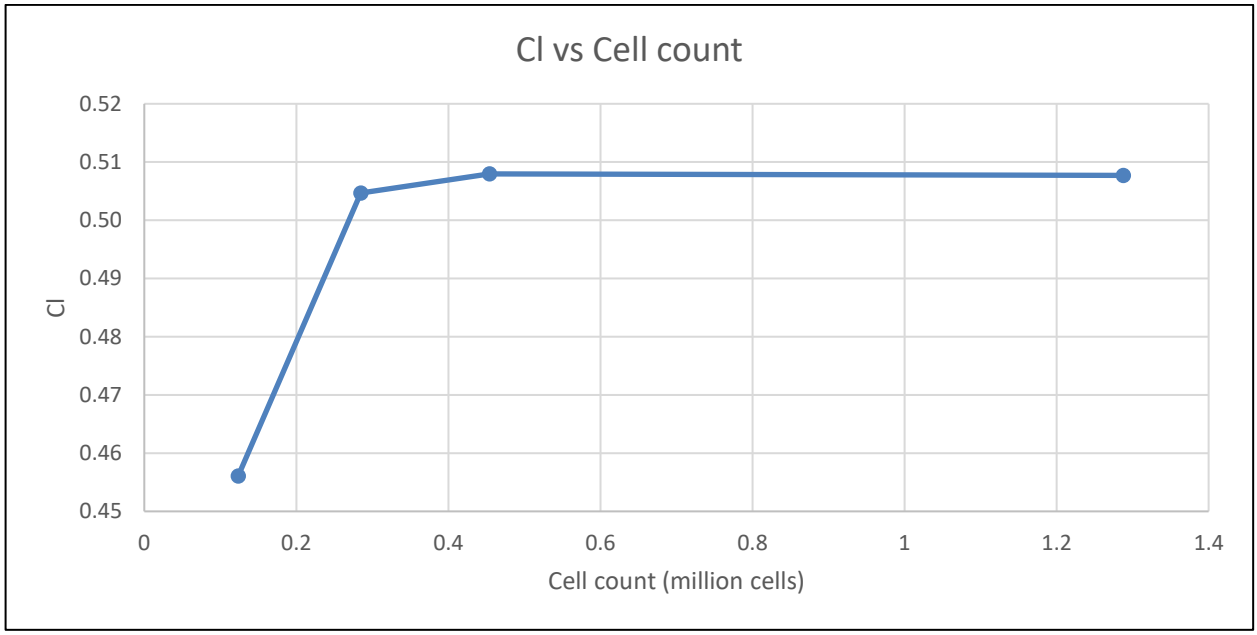

Figure 4-6: C_l Mesh independency for NACA-0018

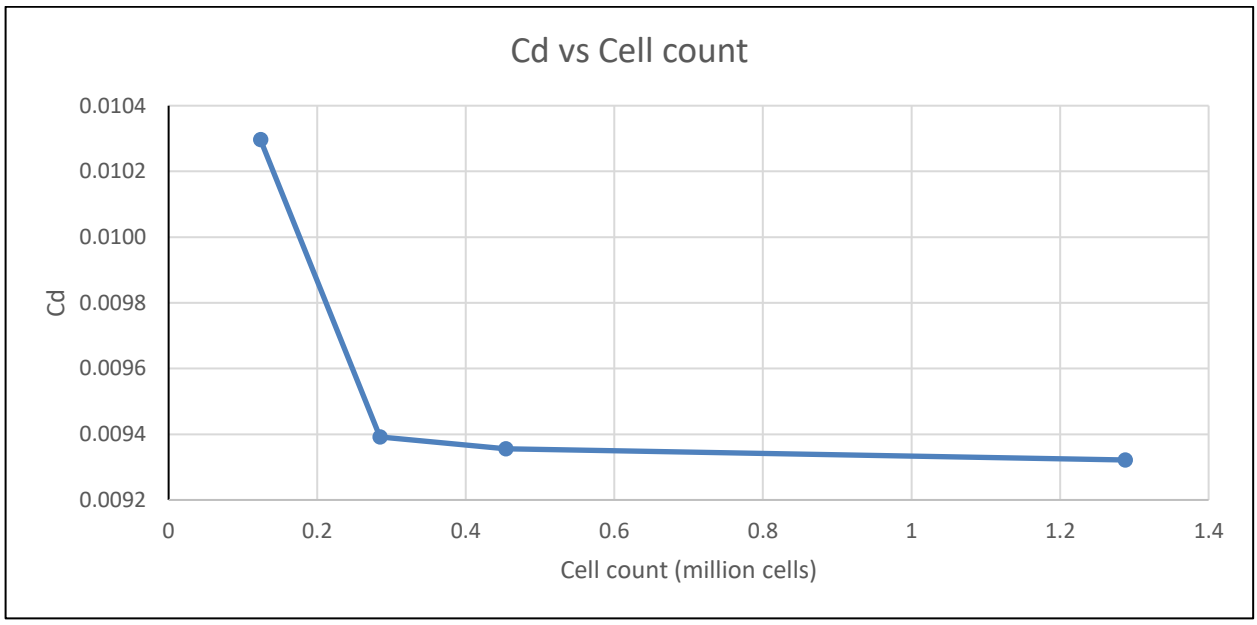

Figure 4-7: C_d Mesh independency for NACA-0018

4.4.2 Aerodynamic coefficients results

The data from the STAR-CCM+ solution was compared to data from XFOIL, as well as experimental data for the NACA-0018 airfoil simulated at various angles of attack. A key characteristic of the NACA-0018 airfoil is that it has a symmetrical shape; in other words, there will be no lift produced at a zero-degree angle of attack as shown in the results (Figure 4-8). At low angles of attack, the STAR-CCM+ and XFOIL results compare well with the wind tunnel results, but the error in the results increases as the angle grows. The results are plotted on a graph and are illustrated in Figure 4-8 and Figure 4-9. A too high value for the lift coefficient was predicted with STAR-CCM+ when the AOA was increased beyond 9°.

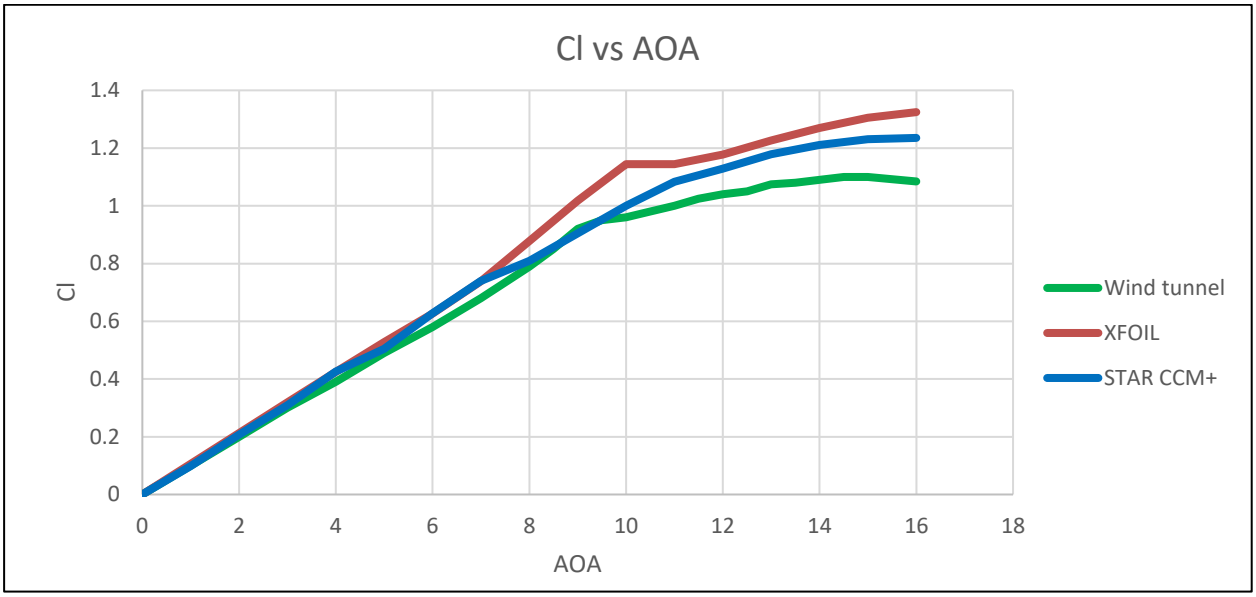

Figure 4-8: C_l vs AOA of NACA-0018 at $Re = 0.7 \times 10^6$

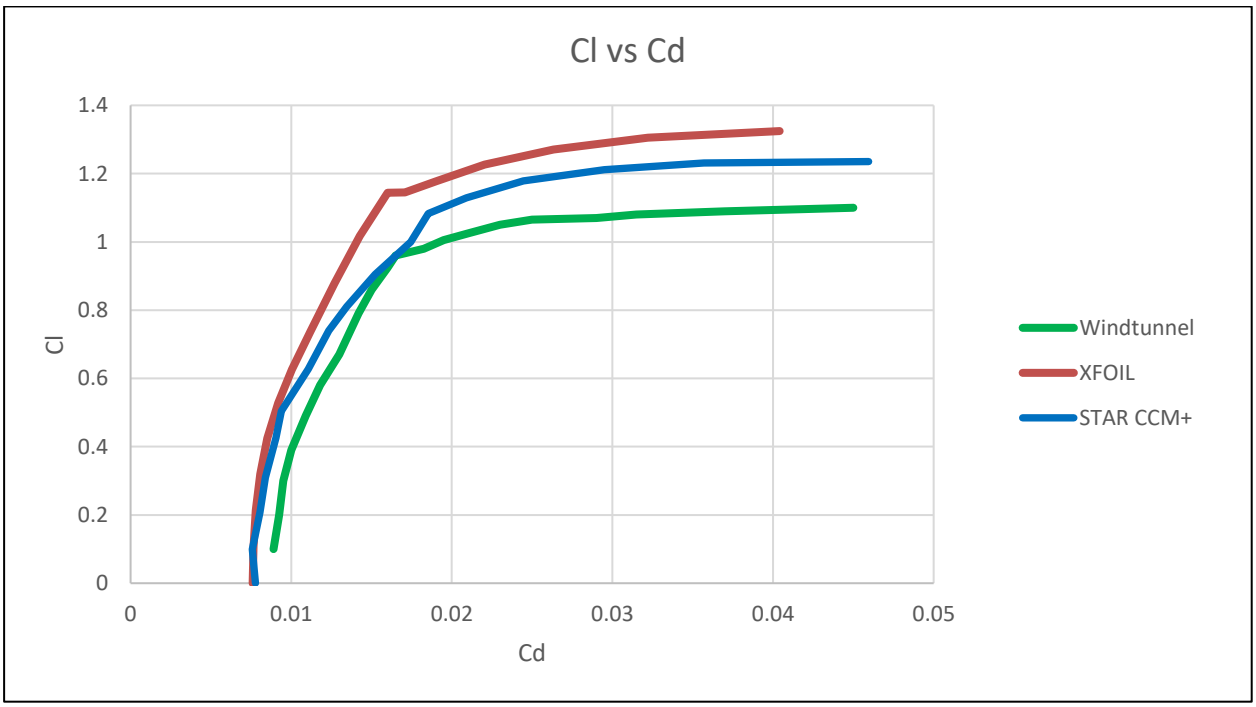

Figure 4-9: C_l vs C_d of NACA-0018 at $Re = 0.7 \times 10^6$

The reason for this increase in error beyond 16° is because of flow separation on the surface of the airfoil (Timmer, 2008), and also because the $\gamma - Re_\theta$ transition model cannot accurately simulate the occurrence of a stall (Hansen, 2014). This error cannot translate into the work for the boundary layer suction study, as the vertical stabilizer was only studied at low angles of attack and the studies were steady state. When the angle of attack was increased beyond 16°, the values for STAR-CCM+ had difficulty converging due to separation.

4.4.3 Transition location results

Transition on the NACA-0018 airfoil at $Re = 0.7 \times 10^6$ and $0°$ AOA occurs on the 59 % chord length position (Timmer, 2008). XFOIL also indicates this to be the location for transition on the NACA-0018. The point of transition for this validation study can be seen on a skin friction coefficient plot in Figure 4-10. Transition occurs at $0.15\,m$ on the $0.25\,m$ chord airfoil, which means $x/c = 60\,\%$ and the percentage error from Timmer's predicted value is $1\,\%$.

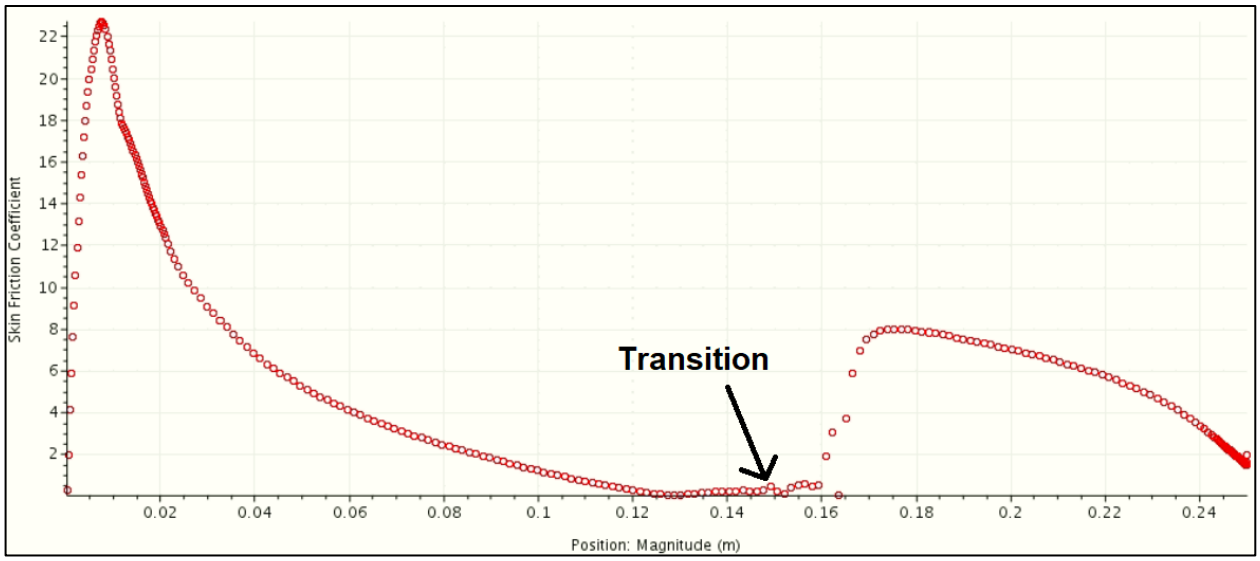

Figure 4-10: Skin friction coefficient plot of NACA-0018 at 0° AOA

4.5 Conclusion

Looking at Figure 4-8 and Figure 4-9, it is clear that the results of STAR-CCM+ compare well with XFOIL as well as the wind tunnel data at low angles of attack. The results of STAR-CCM+ are over predicted at angles of attack higher than $9°$. Convergence becomes an issue once the angle of attack gets bigger than $16°$ because of flow separation from the wall. Laminar-turbulent transition was accurately predicted by STAR-CCM+ and the $\gamma - Re_\theta$ transition model at low angles of attack. The study on boundary layer suction was completed at $0°$ angle of attack, which means that the accuracy of the boundary layer suction simulations (Chapters 6 and 7) were high.

CHAPTER 5: THREE-DIMENSIONAL VALIDATION

Three-dimensional verification was conducted in a similar manner as two-dimensional verification, Chapter 4. The three-dimensional validation was performed by comparing the STAR-CCM+ results to the results from the study done by Thomas Hansen (Hansen, 2014), as well as flight tests conducted on the Standard Cirrus glider. A visual comparison of the transition was made in conjunction with a comparison of the performance speed polar between this validation study, research of Hansen and flight tests done at Idaflieg, Germany (Hansen, 2014).

The three-dimensional validation study shows competence in the CFD simulations to follow. This validation was done on the Standard Cirrus; a sailplane that is used in world club class competitions. The validation simulations also show the ability of CFD to calculate and predict transition locations on the surfaces of the empennage which is crucial for accurate overall performance prediction of the sailplane. The experimental values on the Cirrus glider are from flight tests conducted at Idaflieg in Germany during the annual Sommertreffen in 2011. Hansen (2014) also simulated this sailplane to create a validated reference model. These two cases were used for comparison in this validation.

The flight tests from which the experimental data were extracted, were completed to establish the effect of different leading-edge tapes on the wing to increase the gliding flight performance. Three of the flights were conducted to establish the flight performance without the use of tapes to investigate the performance of the glider. The aim of these flights was to determine the performance with modern technologies since the previous flight tests were conducted in 1974. The results from the clean configuration flight tests were used during the validation study. According to the flight tests, the mass of the glider was $355.6\ kg$ and the reference area, S, was 10 m^2 (Pätzold, 2012). The velocities at which these simulations were performed, ranged between $90\ km/h$ and $160\ km/h$.

The CFD simulations by Hansen were also done with STAR-CCM+ by solving the Reynolds-Averaged Navier-Stokes equations with the $\gamma - Re_\theta$ transition model as well as the $k - \omega$ SST turbulence model. During his simulations, a trimmed hexahedral mesh was used in conjunction with a hyperbolic extruded prism layer. The turbulence intensity was set to 0.1%, with a turbulent viscosity ratio of 10. Hansen defined the free-stream edge of the turbulence model at $50\ mm$. The angles of attack used to find the needed lift coefficient at specific velocities, are found in the report of Hansen. This data was used to create the speed polar graph as part of the validation.

5.1 Three-dimensional validation requirements

As with the two-dimensional validation, it is critical to accurately predict the location of transition. This is especially significant due to the role the laminar flow region plays in suction modelling, as well as the influence transition has on the aerodynamic properties when a larger area laminar flow can be established. The occurrence of a laminar separation bubble on the surface must also be predicted by CFD, as well as the influence on the aerodynamic performance.

5.2 Three-dimensional validation setup

The accuracy of the results is influenced by the setup of the simulation on STAR-CCM+. The setup of the simulation, including the geometry, mesh and solver setup, is discussed in this section.

5.2.1 Geometry setup

The mesh size is reduced by applying symmetry conditions on the Standard Cirrus glider; only one half of the glider was therefore simulated. The flow domain used for the simulation of the Standard Cirrus glider, was a $[35\ m, 15\ m, 15\ m]$ rectangle with the origin at $[8\ m, 7.5\ m, -7.5\ m]$. After this geometry was created, the body of the glider was imported into STAR-CCM+, rotated to the appropriate angle of attack and subtracted from the rectangular flow domain. The surfaces were split into the necessary parts in order to define specific areas of the glider and the flow domain. These surfaces were used to create regions where the boundary conditions were defined.

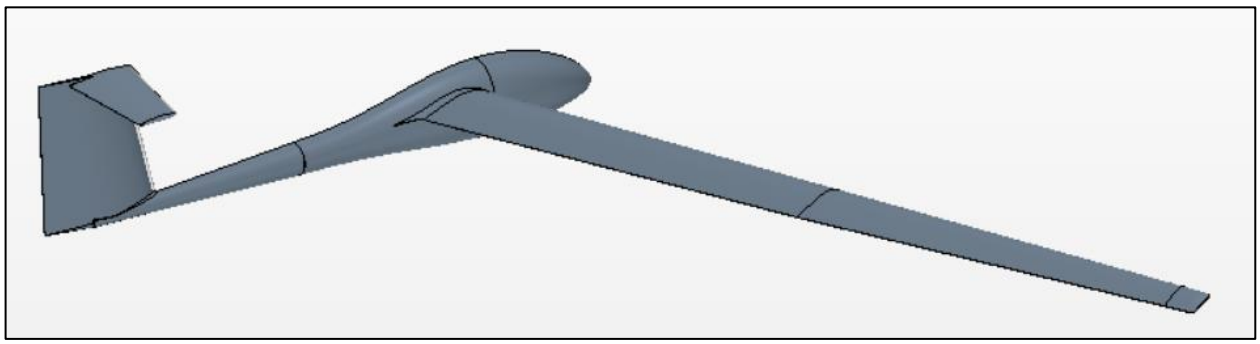

Figure 5-1: Geometry of the Standard Cirrus glider half used in this CFD validation

5.2.2 Grid configuration

A mesh was created of the flow domain where the surface re-mesher was used. Along with the surface re-mesher, the polyhedral mesher was used as the main volume mesher and the prism layer mesher was selected as an optional boundary layer mesher.

Custom surface and volumetric controls were used on critical areas like the root of the wing, at the trailing edges, the wing itself and the fuselage to capture the flow around these parts. Mesh refinement of the boundary layer and wake is imperative for accurate results as the mesh plays an important role in near and far field calculations. The wake refinement control was activated in the trailing edge surface control to capture the wake past the airfoil. The mesh at the root of the wing and the prism layer mesh on the fuselage are visualized in Figure 5-2.

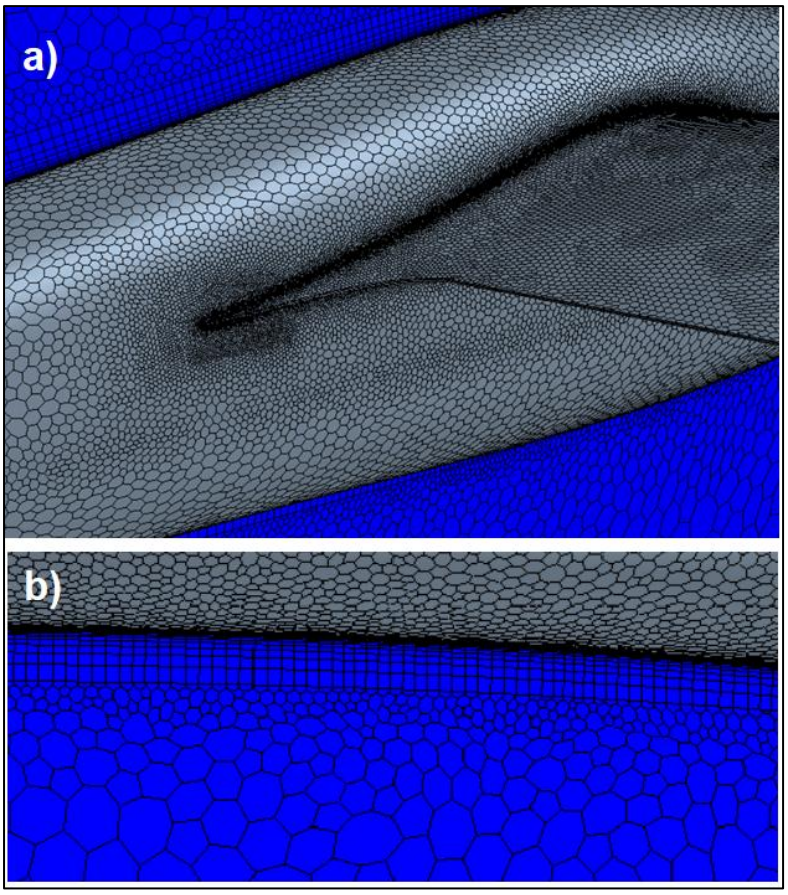

Figure 5-2: a) Mesh at the root of the wing of the Cirrus glider, b) Prism layer mesh on the surface of the fuselage

5.2.3 Setup of flow parameters and physics

The two opposite sides of the flow domain where fluid enters and exits the domain, consist of a velocity inlet and a pressure outlet. The transition model utilised by the boundary layer flow, was chosen as the $\gamma - Re_\theta$ transition model with the user field function set to $8\ mm$ and applied to the free-stream edge definition. The $k - \omega$ turbulent model was used and the velocities at which these simulations were performed, are between $90\ km/h$ and $160\ km/h$ - applied at different angles of attack. The turbulence intensity was set to $0.1\ \%$, and the turbulence viscosity ratio was kept at 10. The angle of attack and velocity of the Cirrus glider, which was used in the CFD simulations, are tabulated in Table 5-1.

Table 5-1: Input data for speed polar

Velocity $[km/h]$	**90**	**95**	**100**	**110**	**120**	**140**	**160**
Angle of attack$[deg]$	2,663	1,77	1,013	-0,207	-1,128	-2,396	-3,22

5.3 Three-dimensional validation procedure

The first step in the three-dimensional validation process was to investigate the impact of mesh size on the correctness of the aerodynamic properties and phenomena. A mesh independency study was conducted to ascertain the suitable mesh density for the validation process.

The validation was firstly done by visually comparing the location of the boundary layer transition on the Standard Cirrus glider on various locations of the glider. The visuals used in the evaluation originates from the study done by Hansen, and were compared to the CFD model of this validation study. Another comparison was done by simulating the sailplane at several angles of attack and speeds to compare the speed polar graph to results from Hansen's report and flight test results, which were conducted at Idaflieg. The speed polar is an indicator of the performance of a glider, and the graph represents the speed of the glider versus its sink rate. The weight of the sailplane was $3488\ N$, the air density was 1.225 $kg.m^3$ and the surface area of the wing was 10 m^2 (Hansen, 2014).

5.4 Three-dimensional validation results

A mesh dependency study was conducted on the Standard Cirrus glider in order to determine what the quality of the mesh must be to successfully simulate the validation model. The results of the study are visible in Figure 5-3 and Figure 5-4.

5.4.1 Mesh independency results

The prediction of lift was very accurate, with a deviation of 2.8% between the mesh with 1.4 million cells compared to the finest mesh with 66 million cells. The deviation was 0.13% when the mesh had 18 million cells. Although this is true for lift, the drag value is not as accurately predicted by a coarse mesh. Therefore, a finer mesh was necessary. There was a 21% deviation in the coefficient of drag when using a mesh with 2 million cells compared to the finest mesh, whereas the difference is a mere $1.2\ \%$ when the mesh density increased to 18 million cells.

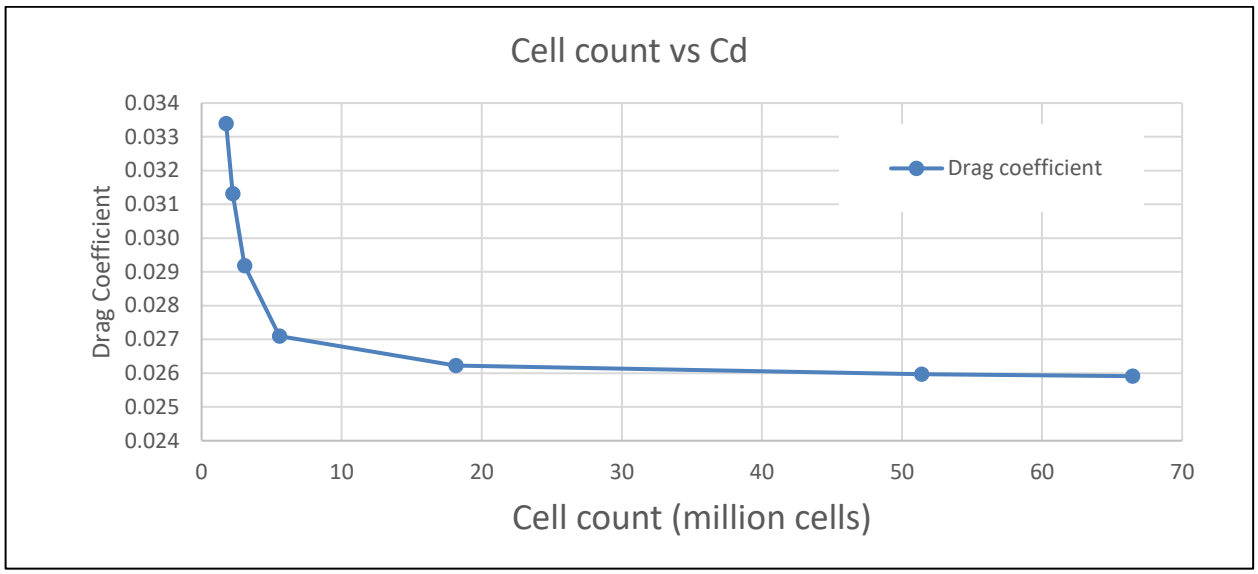

Figure 5-3: Mesh independency results for three-dimensional: Cell count vs Cd

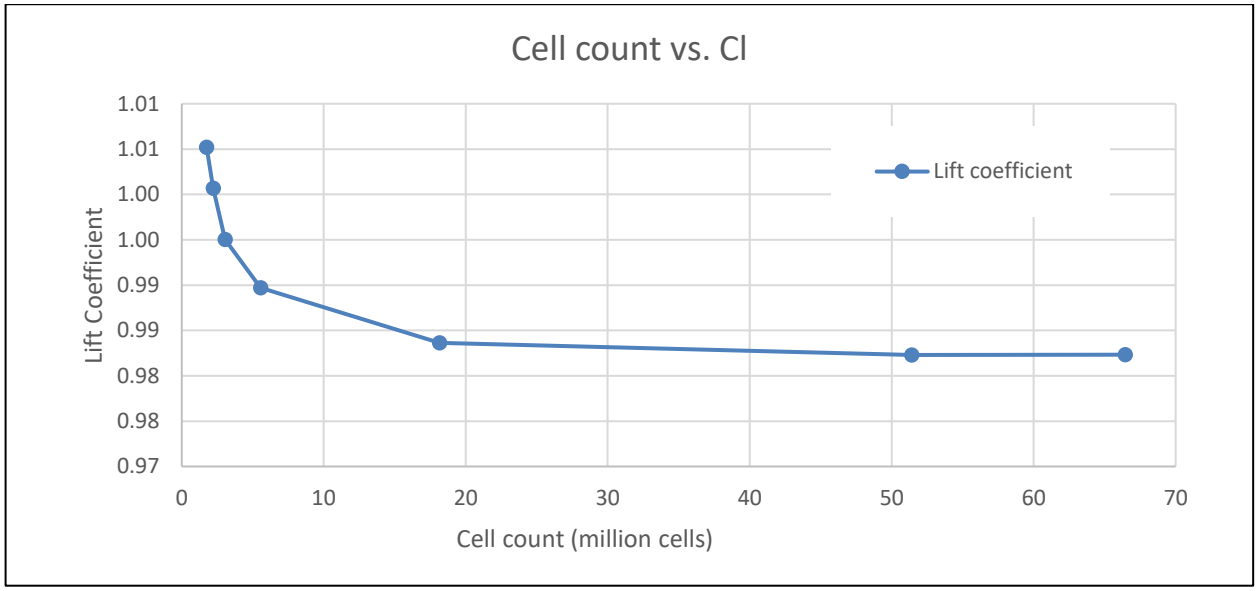

Figure 5-4: Mesh independency results for three-dimensional: Cell count vs Cl

5.4.2 Transition results

The turbulent kinetic energy produced on the top side of the Cirrus glider can be seen in Figure 5-5. The left side is of the Cirrus glider from Hansen, and the right side is from this validation. The transition process begins near the middle of the chord along the span of the wing. The location where the turbulent kinetic energy is a maximum, occurs where the laminar transition bubble is present. Behind the bubble, the flow reattaches and turbulent flow trails the reattachment point.

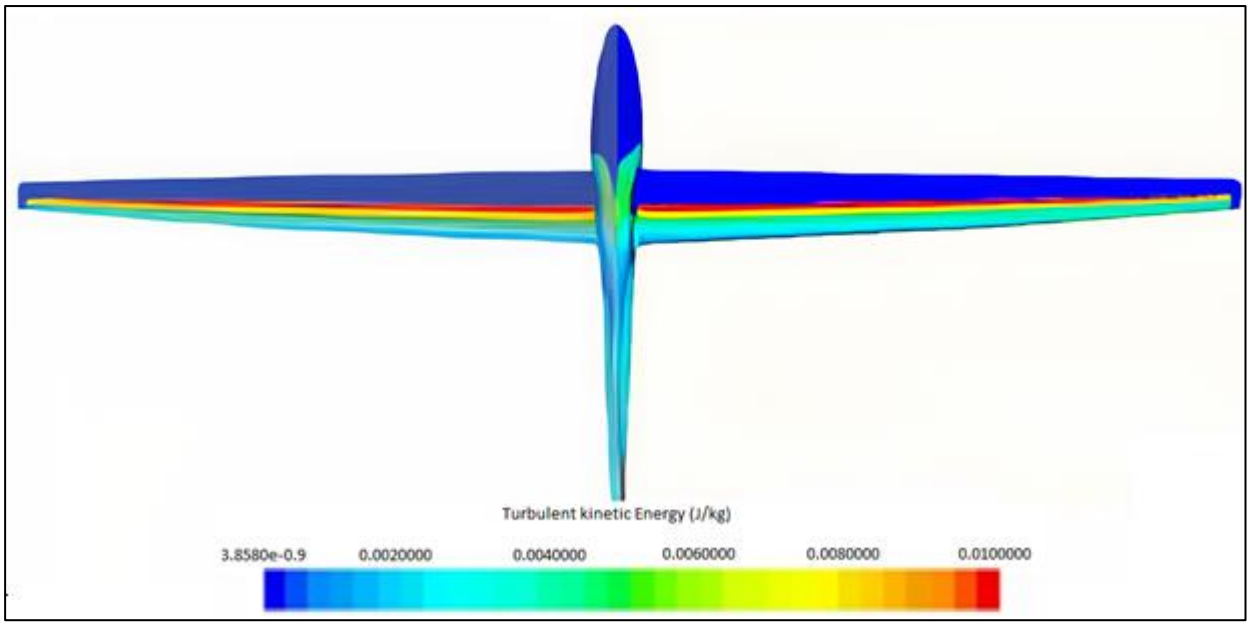

Figure 5-5: Transition viewed from above. Left is Hansen study, right is this validation

Figure 5-5 illustrates that the turbulent kinetic energy produced on the bottom side of the glider is minimal. The start of the turbulent flow of the study by Hansen and the validation occurs at the same point. There is a slight difference between the starting point of turbulent energy on the fuselage. This can be because of using a different type of mesh and a different mesh setup.

Transition on the bottom side of the glider is visualized in Figure 5-6. The laminar separation bubble is small and the turbulent kinetic energy very low. The laminar region at the wing tips does not model real flow correctly, and the $\gamma - Re\theta$ model is unable to model the vortices produced by the wing tips (Hansen, 2014).

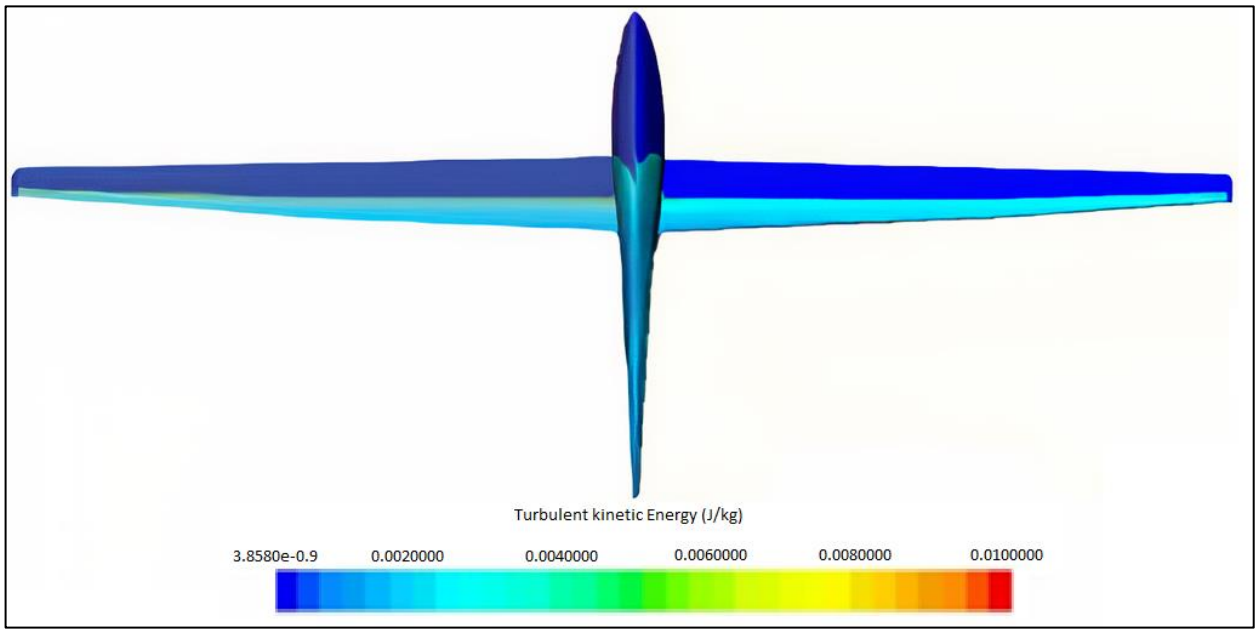

Figure 5-6: Transition viewed from the bottom. Left is Hansen study, right is this validation

5.4.3 Speed polar results

Since a speed polar graph is a measurement of performance, it was used as another method of comparison. The sailplane was simulated at different velocities and specific angles of attack to obtain the information required for the speed polar graph. The sink rate was plotted against velocity for the speed polar.

An aircraft in straight and level flight must have a lifting force equal to the weight of the airplane. The same cannot be applied for a glider because there is no propulsion. A glider in steady level flight is in an un-accelerated descent. The equations in this section explain how the sink rate equation can be attained, which was used for the speed polar graph.

The coefficient of lift is expressed in equation 5.1

$$C_L = \frac{L}{q_\infty S} = \frac{W}{q_\infty S} = \frac{mg}{q_\infty S} \tag{5.1}$$

and the coefficient of drag is illustrated in equation 5.2

$$C_D = \frac{D}{q_\infty S} \tag{5.2}$$

With S being the reference area, m being the mass of the glider and g being the gravitational constant. q_∞ is the dynamic pressure, as depicted by equation 5.3

$$q_\infty = \frac{1}{2}\rho_\infty V_\infty^2 \tag{5.3}$$

where ρ_∞ is the air density and V_∞ is the free-stream velocity. The descent glide angle is not dependent on the altitude of the glider or the wing loading, and is shown in equation 5.4

$$\tan(\theta) = \frac{1}{C_L/C_D} \tag{5.4}$$

The sailplane must fly at a fixed velocity, also known as the equilibrium glide velocity, to attain a certain C_L/C_D. The performance of a glider can be measured by creating a speed polar, which is a graph that demonstrates the velocity of the glider against the sink rate. The sink rate is shown in equation 5.5

$$h = V_\infty \sin(\theta) = -V\frac{C_D}{C_L} = -\sqrt{\frac{W}{\frac{1}{2}\rho S C_L}}\frac{C_D}{C_L} \tag{5.5}$$

The speed polar graph of the Standard Cirrus glider was compared to experimental results from the flight tests done at Idaflieg. In Figure 5-7, results from Hansen and from this validation study are shown. The results from Hansen shows an improved rate of descent in comparison to the flight data. The reason for this phenomenon can be dependent on a number of things, which include the fact that a hexahedral mesh was used to characterize the flow boundary, the shape and size of the flow domain could have an influence as well as the refinement of the mesh at vital locations. A structured hexahedral mesh was used by Hansen, a highly space-efficient model, but the results when using this mesh are not accurate for very complicated geometries. The validation study done for this dissertation shows that the results are close to that of the Idaflieg flight tests. This is an indication that the simulation was an adequate representation of reality.

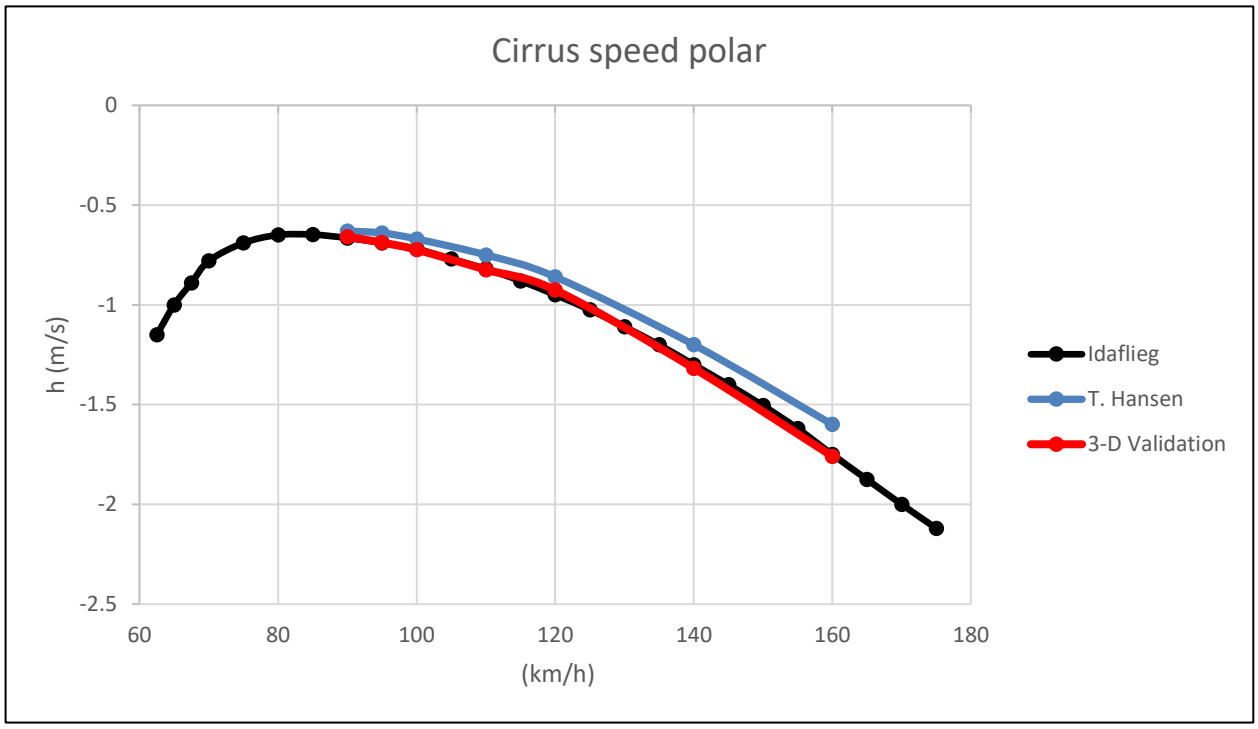

Figure 5-7: Speed polar of the Standard Cirrus glider

5.5 Conclusion

In this chapter, the validation was done on the Standard Cirrus glider by using the CFD code STAR-CCM+. The flow was considered to be steady, and the $k-\omega$ SST turbulence model was used in conjunction with the $\gamma - Re_\theta$ transition model. The three-dimensional study followed, and the results were compared to the study done by Hansen, as well as to that of flight tests done at Idaflieg, Germany.

It was found from the simulations that the numerical model portrays the performance of the glider well. The simulation setup for the validation will be used as the point of departure for the boundary layer suction simulations.

CHAPTER 6: BOUNDARY LAYER SUCTION MODELLING

The concept of boundary layer suction applied to the empennage of a sailplane was introduced in Chapter 2, and it was apparent that a possibility for drag reduction exists due to a stabilized and prolonged laminar boundary layer. This stabilization prevents premature transition and the result is an extended region of laminar flow. The implementation strategy for boundary layer suction on the JS3 vertical stabilizer is discussed in this chapter. The ultimate goal was to find the boundary layer suction configuration which had the best results to reduce drag of the JS3 vertical stabilizer. The CFD simulations were done in two and three dimensions, where the two-dimensional study was conducted as an introduction to boundary layer suction and to present the general flow occurrences associated with boundary layer suction.

The setup and results are explained in each section. The results are also discussed for each part of the aerodynamic improvement process. The different features analysed during improvement of the aerodynamic properties include the hole location defined by the chord length, the suction hole size, the spacing of the suction holes and the influence on drag of two and three rows of boundary layer suction holes. Another factor which had to be confirmed, is the required pressure difference between the inlets (suction holes) and outlet to drive the boundary layer suction system.

All the simulations were conducted with STAR-CCM+, and the geometries were generated with NX. The angle of attack of the airfoils was set at $0°$, and the chord length of the airfoils was $1\ m$. The simulations were performed at a velocity of $40\ m/s$. This value was taken from the 2018 South African Nationals, where the winner of the 18 Meter class flying a JS3 sailplane, maintained an average speed of $39.56\ m/s$ across six tasks during the competition (Naviter, 2018). Although the cruise speed is higher than this average flight speed from the competition data, the simulations were conducted at this speed. It was argued that should suction be beneficial at this velocity, which is the lower range of cruise speeds, it would also be beneficial at higher flight speeds.

6.1 Two-dimensional boundary layer suction

Boundary layer suction in two dimensions was examined in order to determine whether it will result in drag reduction when applied to the JS3 vertical stabilizer airfoil by using minimal computational resources and time. The aim of these two-dimensional investigations was to examine the flow phenomena near the suction hole, and to establish the impact of boundary layer suction on transition.

The positioning of the boundary layer suction holes was influenced by the boundary layer transition location, which is evident in the sections to follow. Boundary layer suction must be placed before the point of transition due to the increased suction force required for a turbulent boundary layer. The influence of boundary layer suction on aerodynamic properties is shown by comparing a clean airfoil with an airfoil using boundary layer suction. This airfoil where boundary layer suction is not present, is referred to as the baseline model.

The setup of the CFD simulation was similar to that of the two-dimensional validation in Chapter 4. The solver and mesh configurations were already validated and, therefore, the same methodology was used in the following sections.

6.1.1 Two-dimensional baseline model

The baseline model consisted of an airfoil of the JS3 vertical stabilizer, with a chord length of $1\ m$ and with no boundary layer suction present. The environmental parameters which were utilised are summarized in Table 6-1.

Table 6-1: Environmental parameters for two-dimensional baseline model setup

Parameter	Value	Unit
Velocity	40	m/s
Density	1.225	kg/m^3
Pressure	101325	Pa
Chord length	1	m
Dynamic viscosity	1.85×10^{-5}	m^2/s
Reynolds number	2.65×10^{6}	-

The drag value associated with the baseline model was $D = 3.881\ N$. The coefficient of drag for this model was calculated as $C_d = 0.00396$, the skin friction drag coefficient was $C_{df} = 0.00291$ and the pressure drag coefficient was $C_{dp} = 0.00105$.

The transition location of the baseline model airfoil can be seen by utilising a pressure versus position plot, as well as a skin friction coefficient versus position plot (Figure 6-1). The point of transition is seen on both graphs at the point where a discontinuity occurs and there is a sudden pressure fluctuation. The pressure difference is due to the outer flow resisting displacement from the larger boundary layer thickness, which occurs when transition takes place (Van de Wal, 2010).

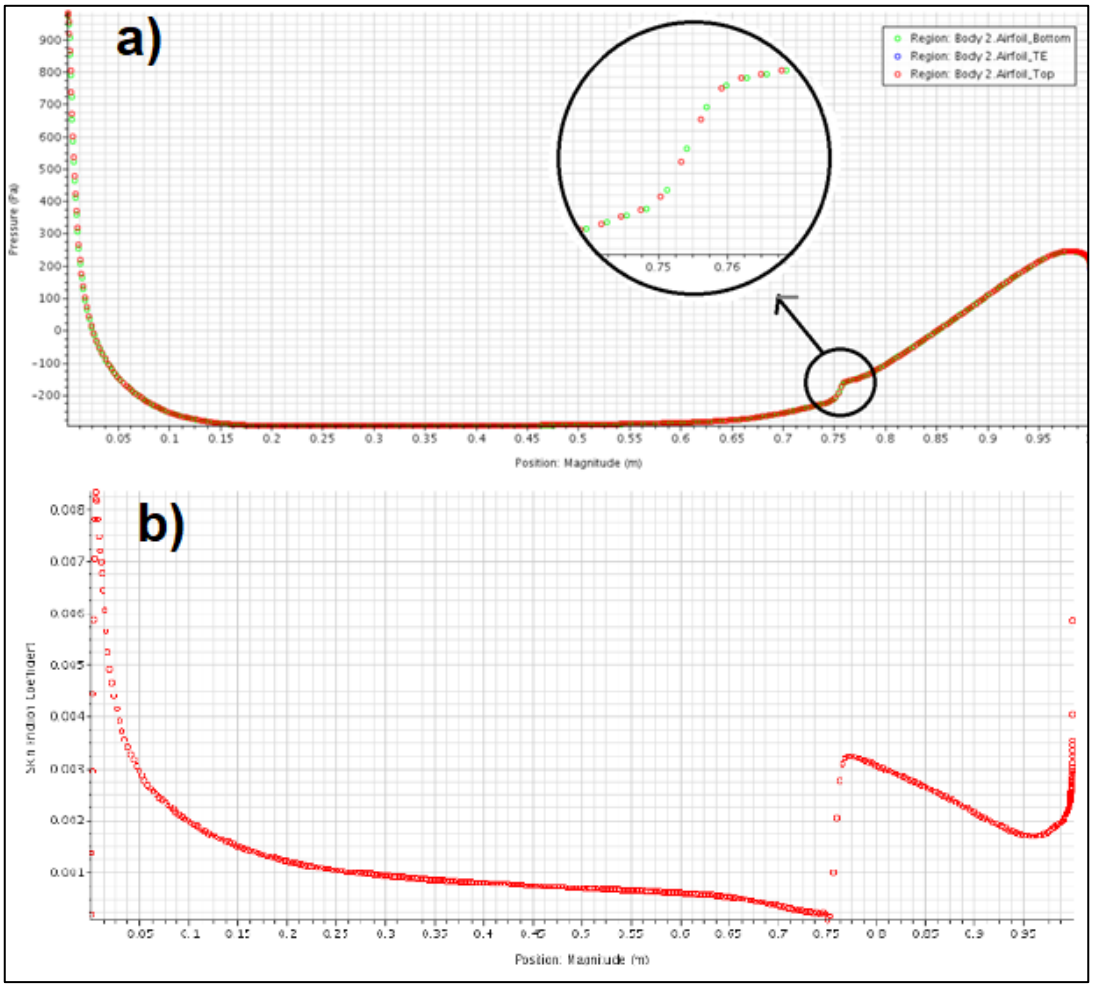

Figure 6-1: Point of transition on two-dimensional JS3 vertical stabilizer airfoil: a) Pressure vs position, b) Skin friction coefficient vs position

For adequate boundary layer control, the suction holes must be placed upstream of the transition point due to the fact that a laminar boundary layer is a prerequisite for the successful implementation of boundary layer suction. This is because the suction force needed when the boundary layer is turbulent, is excessive for drag reduction. Transition was calculated at $x/c = 74.5\ \%$ on the baseline airfoil, which indicates good potential for the application of boundary layer control on this flow region which is mostly laminar.

6.1.2 Two-dimensional model setup

The effect of boundary layer suction was investigated when applied in the range between 67% and 72% of the chord length. The geometry for the simulation at a $70\ \%$ chord is shown in Figure 6-2, illustrating the top and side views of the airfoil, respectively. The dimensions are in millimetre and the size of the two-dimensional suction hole, or "slot", is $1\ mm$.

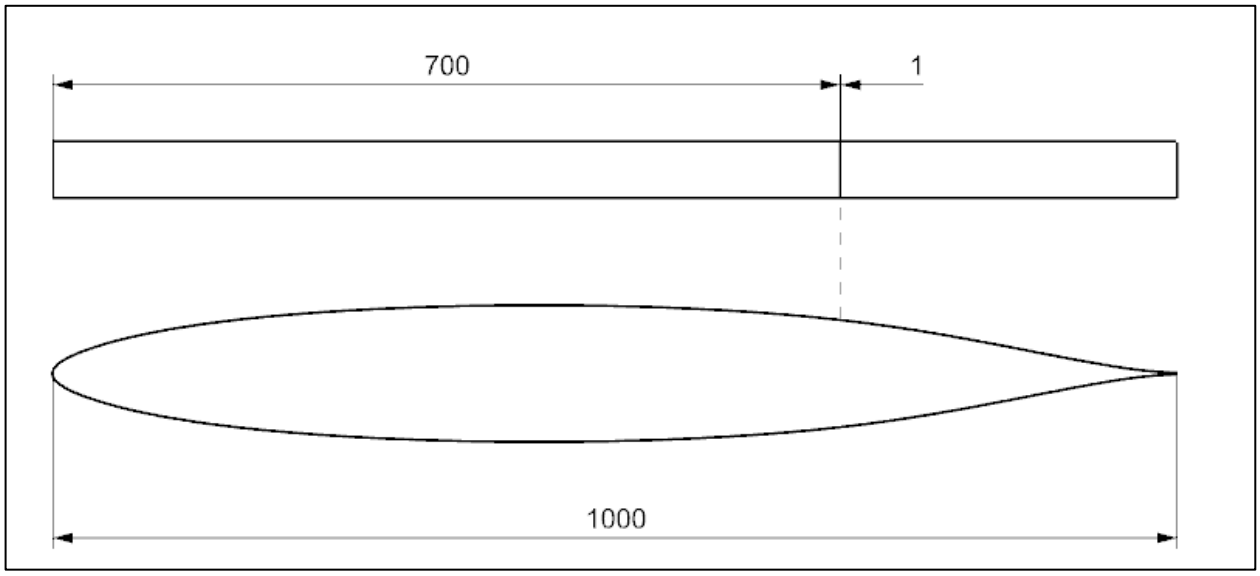

Figure 6-2: Geometry setup for the two-dimensional simulation, Top and side view

The boundary layer suction slot was created in NX by splitting the surface of the airfoil to have the following four surfaces: top airfoil, top airfoil suction slot, bottom airfoil and bottom airfoil suction slot. The surface of the suction slot was renamed in STAR-CCM+ and a boundary was created for the various suction surfaces. The computational domain consisted of a velocity inlet of $V = 40\ m/s$, a pressure outlet and symmetry planes for the side walls. The airfoil was defined as walls, with the boundary layer suction surfaces defined as pressure outlets. The size of the suction slot for the two-dimensional simulations was $1\ mm$. Boundary layer suction was implemented on the top and bottom of the airfoil.

6.1.3 Two-dimensional procedure

Boundary layer suction was implemented on different chord positions, before the point of transition, on the JS3 vertical stabilizer airfoil. The required pressure to initiate boundary layer suction must be less than atmospheric pressure, and less than the pressure naturally occurring at the location where suction was applied. The influence of boundary layer suction can be established by examining the aerodynamic properties. An iterative procedure was used to vary the pressure at the suction slot for each simulation in order to alter mass flow. The effect of multiple rows of suction holes was not investigated in two-dimensions, but was investigated later in three-dimensions as there are spanwise flow components which must be considered.

6.1.4 Two-dimensional results

The results of the aerodynamic properties from the application of boundary layer suction on the two-dimensional airfoil are discussed in this section. Another subject of discussion is the

consequence of the implementation of boundary layer suction on laminar-turbulent transition when the pressure difference and the suction position are changed.

The graph below depicts drag in Newton versus the pressure difference in Pascal. The pressure difference is between atmospheric pressure ($101325\ Pa$) and the pressure required for mass flow to occur at the suction slot. The figure illustrates the effect on drag when there is a pressure difference across the suction hole and when there is no suction present on the airfoil. The coloured lines in the graph indicate at what percentage chord the slot was implemented. The horizontal line represents the instance when boundary layer suction is not present with an absence of the slot; in other words, a clean airfoil. The drag generated by the airfoil with no suction present is equal to $3.88\ N/m$ at $40\ m/s$, with a planform area of $1\ m^2/m$.

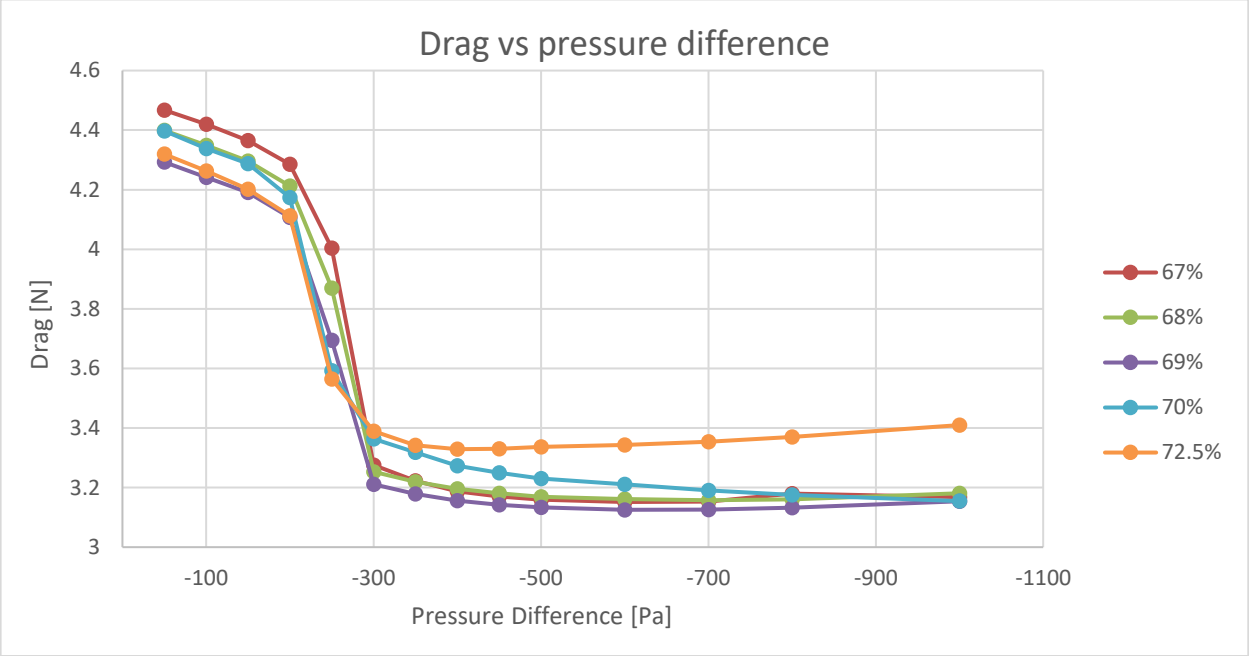

Figure 6-3: Two-dimensional results: The influence of suction pressure and location on drag

Figure 6-3 shows that drag was the lowest when boundary layer suction was applied at $x/c = 69\ \%$. As the suction location shifts toward the leading edge, drag increases minimally. However, when the location of suction moves toward the trailing edge, the drag increase is more substantial. The maximum amount of drag reduced for the two-dimensional boundary layer suction simulation was $19.47\ \%$, when the difference between atmospheric pressure and the pressure at the suction hole was $-600\ Pa$. The drag value at this chord position and with a pressure difference of $-600\ Pa$, was $3.125\ N/m$.

The transition location was at $x/c = 74.5\,\%$ when there is no boundary layer suction present. When suction was applied at $x/c = 69\,\%$, the most significant reduction in drag is seen and the point of transition shifts to the $x/c = 85\,\%$ position, as displayed in Figure 6-4. After boundary layer suction was implemented, the point of transition was extended by $10\,\%$. Even though the boundary layer flow around the airfoil was not completely laminar, there was a substantial improvement in drag of the airfoil with boundary layer suction.

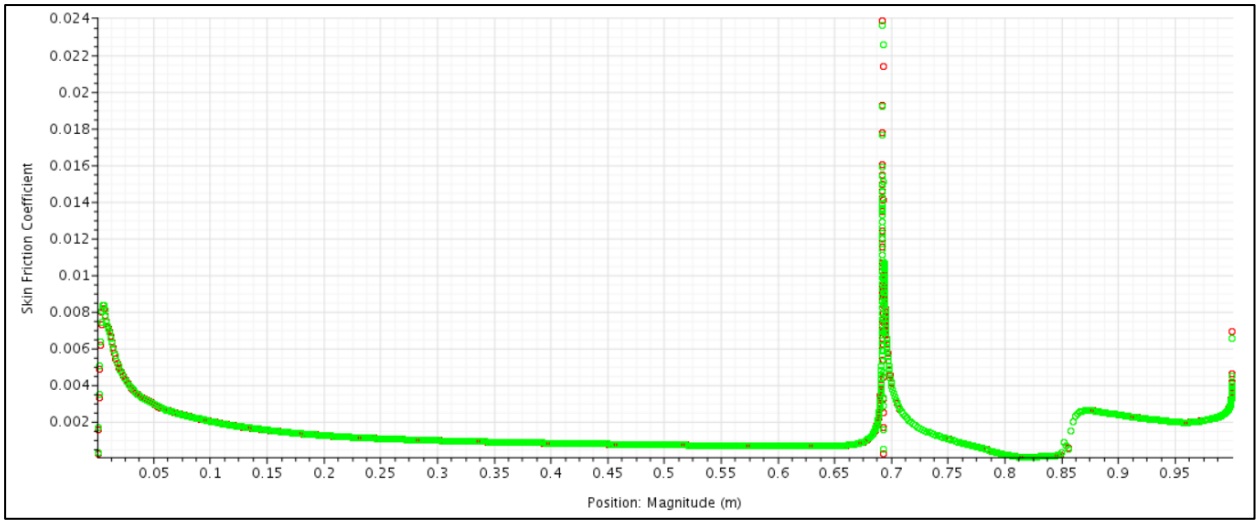

Figure 6-4: Position vs pressure plot for the two-dimensional study at 69 % chord, Δ_P = 600 Pa

When the pressure difference ranges from $0\ to - 250\ Pa$, there was no reduction in drag, but an increase compared to the baseline model. In Figure 6-1 a), the pressure difference on the airfoil where suction was implemented was close to $-250\ Pa$, which means that when a suction force of, for example, $-50\ Pa$ was applied at the suction holes, a blowing motion was established. When the difference in pressure exceeds a specific value, there was a minor drag increase. The reason for this is that air that has already passed the hole, is sucked back into the hole. This phenomenon, present in the boundary layer when the pressure difference is too high, is visible in Figure 6-5 b) with a pressure difference of $\Delta P = -1000\ Pa$. Figure 6-5 a) illustrates the location where boundary layer suction is implemented. Figure b) shows the streamlines in a geometry scene with velocity representing the vector field. The red line designates the location of the suction surface on the airfoil. The fluid flows into the suction hole and, trailing the hole, a region exists where the fluid changes direction as indicated by the black circle. The fluid that has already passed the hole is then sucked back into the hole.

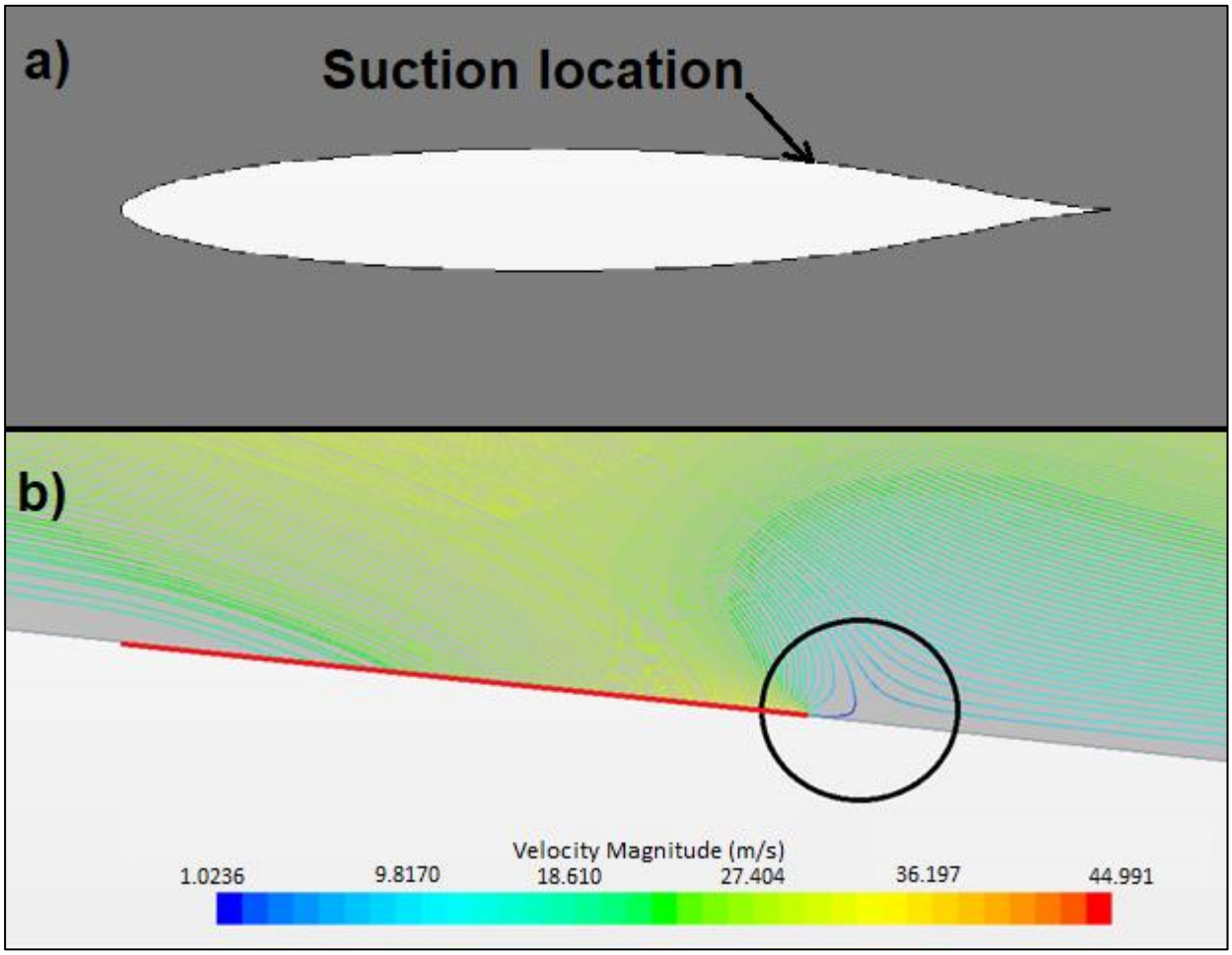

Figure 6-5: Boundary layer at two-dimensional suction hole, $\Delta P = -1000$ Pa

When boundary layer suction was implemented at the region after the point of transition, i.e. in the turbulent boundary region, a higher difference in pressure was required to achieve drag reduction. It will be challenging to achieve a high enough suction force since an external source will not be used, but rather a naturally occurring, low-pressure zone on the glider.

6.1.5 Conclusion for two-dimensional boundary layer suction

From the two-dimensional simulations, it is evident that there was a reduction in drag when boundary layer suction was implemented on the airfoil. This is a good starting point before initiating the three-dimensional investigation since these three-dimensional simulations will be computationally exhaustive and time-consuming. These calculations give sufficient proof for the possibility of drag reduction, and further investigation into the three-dimensional case is necessary. Drag was reduced by 19.47 % when the pressure difference is $-600\ Pa$ on the two-dimensional airfoil section.

6.2 Three-dimensional baseline model

The possibility for drag reduction with the application of boundary layer suction is now further investigated for a three-dimensional flow environment. The baseline model was once again used as a reference to which the three-dimensional boundary layer suction cases were compared. The model used consisted of a three-dimensional clean airfoil, with the profile of the JS3 vertical stabilizer. The airfoil had a chord length of $1\,m$ and a width of $0.1\,m$. Figure 6-6 illustrates the geometry of the side and top views of the baseline model with the dimensions in mm. A CAD geometry of the airfoil was generated in NX and then imported into STAR-CCM+. The computational domain was defined by a velocity inlet with $V = 40\,m/s$, a pressure outlet, symmetry planes for the side walls and the airfoil was defined as walls.

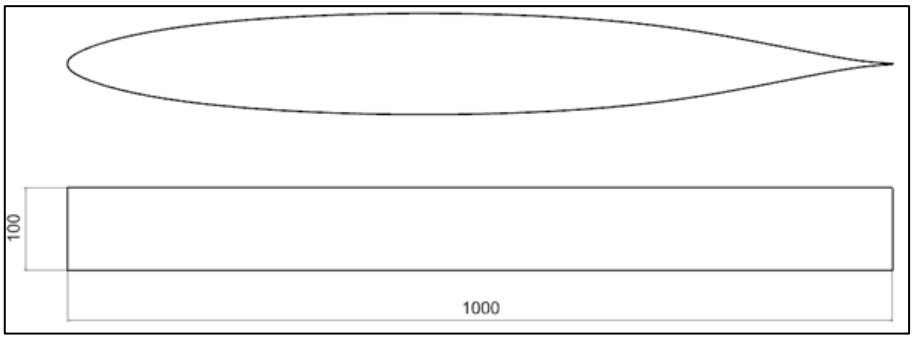

Figure 6-6: Baseline model geometry of three-dimensional $1\,m$ chord airfoil

The position of boundary layer transition was found by examining the skin friction coefficient graph as shown in Figure 6-8. Boundary layer transition on the baseline model without the presence of suction occurred at $x/c = 73.5\,\%$. This value compares well to the two-dimensional case of $\frac{x}{c} = 74.5\%$, which delivers a percentage error of 1.36%. This error can be accredited to the spanwise flow components which are considered in the three-dimensional case, as well as a coarser three-dimensional mesh. Transition is visible where the plot has an acute increase in the skin friction coefficient. The occurrence of a laminar separation bubble on the airfoil is characterized by a bulge on the pressure coefficient plot (Figure 6-9). The turbulent reattachment region after the separation bubble is accompanied by turbulent attached flow, and this is presented by the turbulent kinetic energy, as can be seen in Figure 6-7.

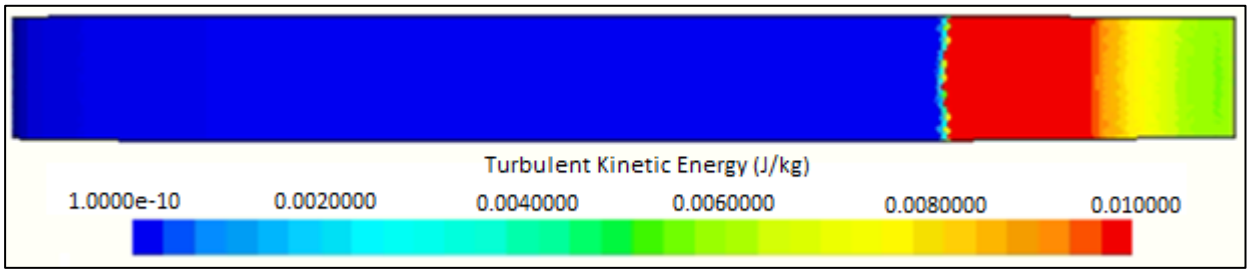

Figure 6-7: Turbulent kinetic energy scene of the three-dimensional baseline model

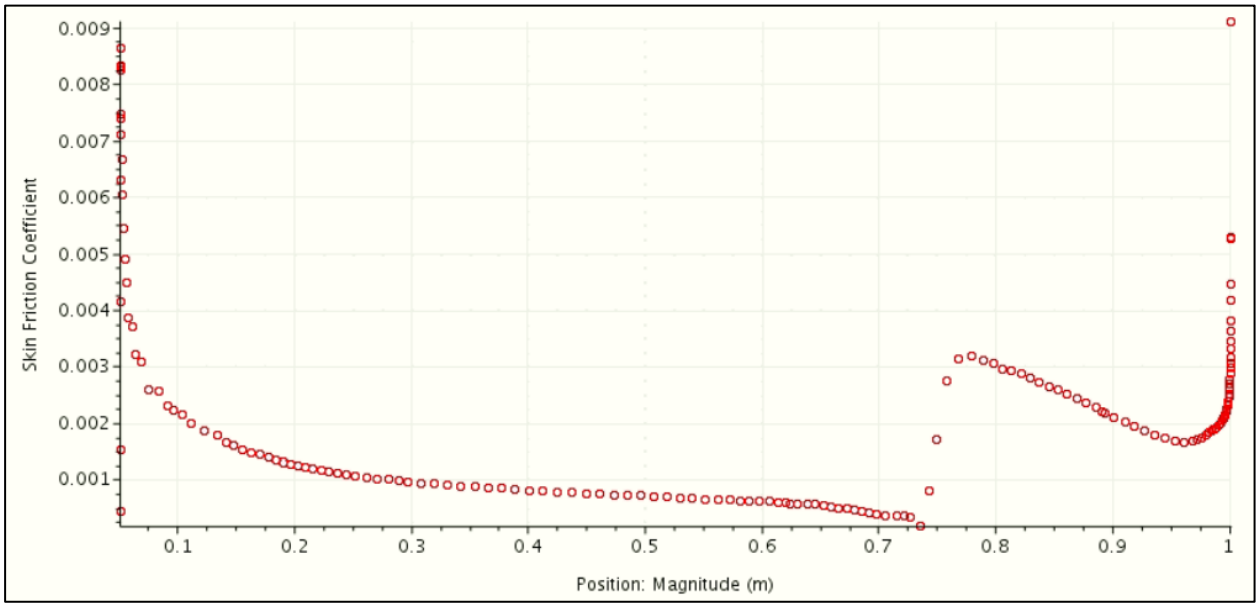

Figure 6-8: Skin friction coefficient plot of the three-dimensional baseline model, Re = 2.65×10^6, AOA = 0°

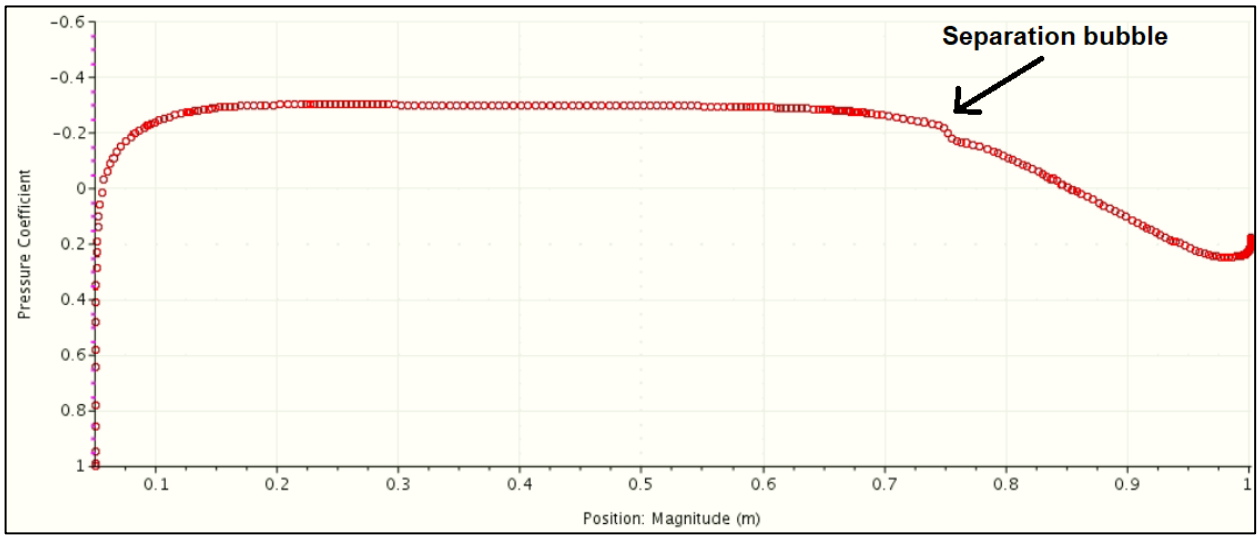

Figure 6-9: Pressure coefficient plot of the three-dimensional baseline model, Re = 2.65×10^6, AOA = 0°

Drag produced by the baseline model airfoil was equal to $D = 0.394\ N$, and the drag coefficient was equal to $C_D = 0.00401$. The results of the baseline model from the two- and three-dimensional cases are tabulated in Table 6-2. The results between the two cases are very similar, with the difference between the drag coefficient of the cases $1.233\ \%$.

Table 6-2: Three-dimensional baseline model results

Case	C_D	C_{Df}	C_{Dp}	Transition x/c %
Two-dimensional	0.003961	0.002911	0.001050	74.5
Three-dimensional	0.00401	0.00294	0.001070	73.5
Percentage difference	1.233%	1.002%	1.870%	1.36%

The skin friction coefficient scene of the baseline model is presented in Figure 6-10. According to literature (Kulkarni *et al.*, 2018), the skin friction drag must increase when the boundary layer turns turbulent, and this phenomenon is indicated in the skin friction coefficient scene of the airfoil below. A reduction in the skin friction drag ensues when the laminar region of the boundary layer is extended, which was done with boundary layer suction.

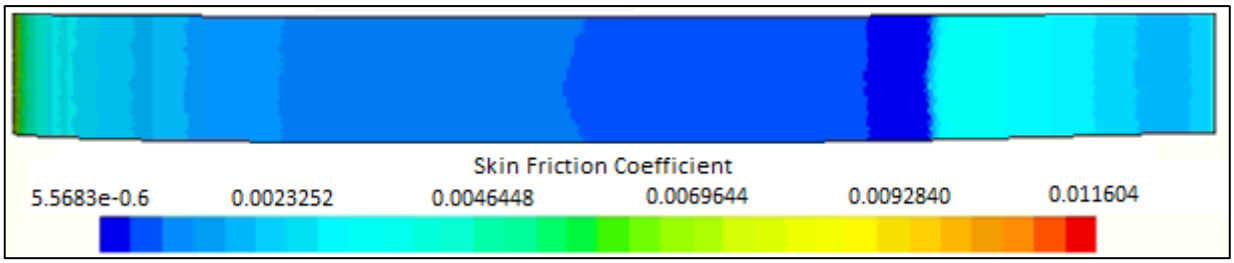

Figure 6-10: Skin friction coefficient scene of the three-dimensional baseline model

6.3 Position of three-dimensional boundary layer suction

This section focuses on the improvement of the aerodynamic properties of the JS3 vertical stabilizer airfoil by examining the most suitable chord position to apply boundary layer suction in a three-dimensional environment. By applying suction to a simplified version of the JS3 vertical stabilizer, computational resources as well as the time to conduct these simulations are kept to a minimum.

6.3.1 Setup to determine three-dimensional boundary layer suction position

In Figure 6-11, the setup of the geometry to determine the optimum three-dimensional boundary layer suction position on the $1\ m$ chord airfoil is shown. The top and side views are depicted with the dimensions in mm. The airfoil consisted of a row of $1\ mm$ boundary layer suction holes, spaced $10\ mm$ apart. Boundary layer suction was implemented on only one side of the airfoil to minimize computational resources and time. The side view illustrates the chamber, a hollow space inside the airfoil, which the suction holes are connected to.

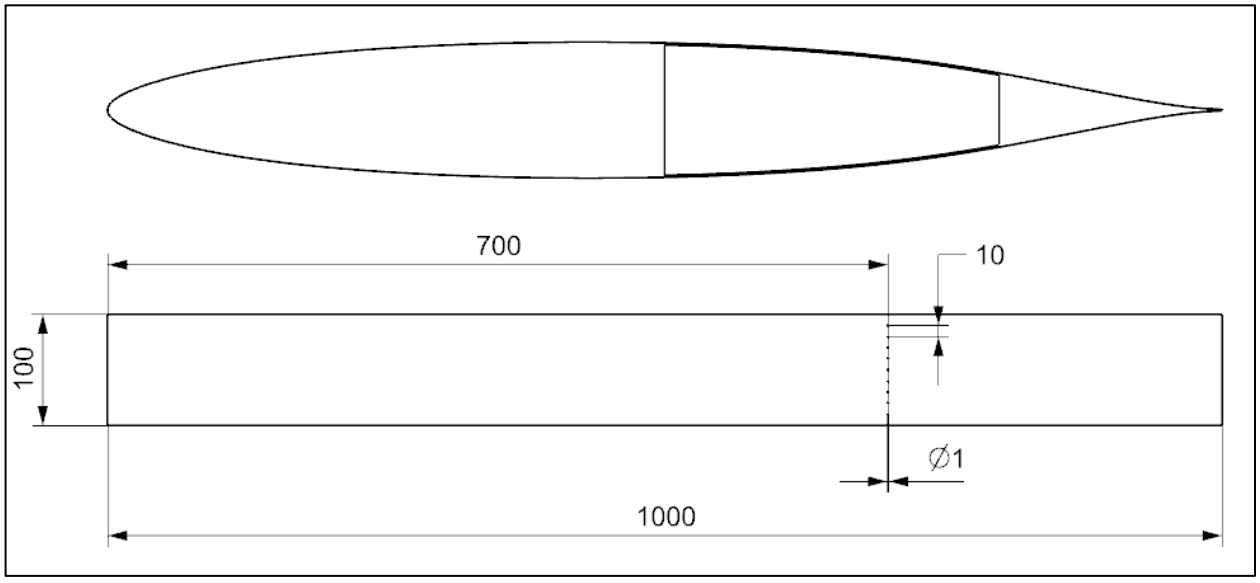

Figure 6-11: Geometry to show suction chord position on three-dimensional $1\ m$ chord airfoil

The boundary layer suction hole boundaries were defined as walls. The bottom side of the chamber inside the airfoil was defined as a pressure outlet, as depicted in Figure 6-12. This pressure was altered during the simulations in order to initiate mass flow through the suction holes.

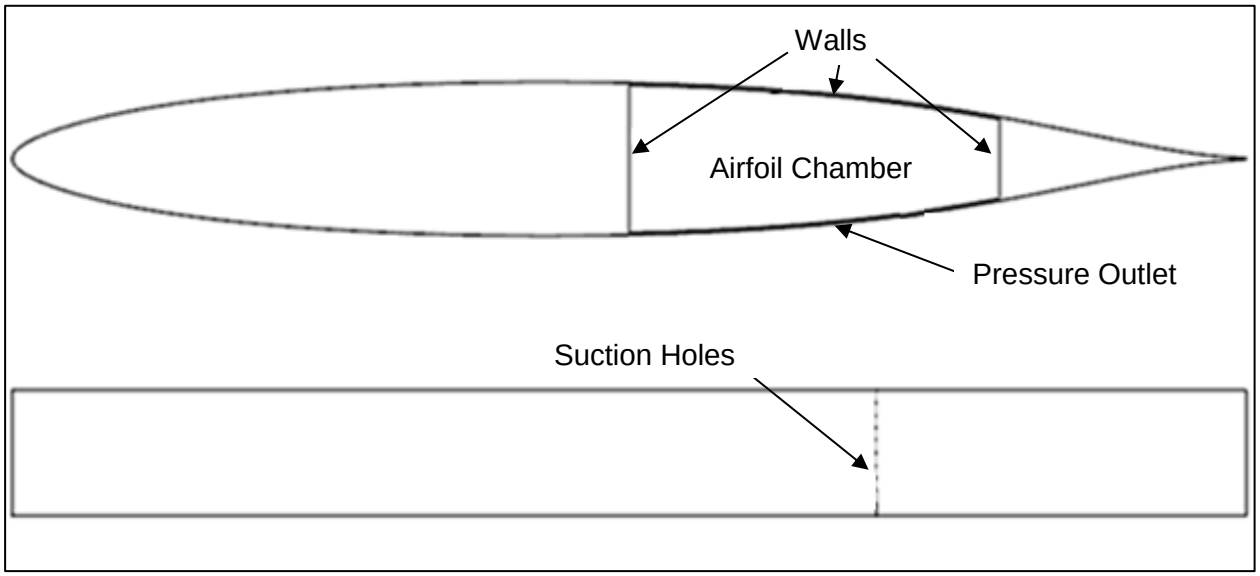

Figure 6-12: Three-dimensional geometry of the airfoil with boundary layer suction

6.3.2 Procedure to determine three-dimensional boundary layer suction position

Figure 6-11 illustrates boundary layer suction applied at a chord position of $x/c = 70\%$. The positions where boundary layer suction was applied, ranges from 68% to 78%. For each simulation, the pressure was changed from $-150\,Pa$ to $-700\,Pa$ at intervals of $50\,Pa$ for the lower pressure differences, and $100\,Pa$ for larger pressure differences. The influence of the change in pressure was examined by looking at several factors, including aerodynamic coefficients, turbulent kinetic energy and skin friction coefficient.

6.3.3 Three-dimensional boundary layer suction position results

The results of the simulations to determine the top boundary layer suction chord position are displayed in Figure 6-13. This graph shows the drag of the airfoil in Newton versus the pressure difference, applied to the bottom surface of the chamber in Pascal. Boundary layer suction was applied at different chord locations, which is presented by the coloured lines in the figure.

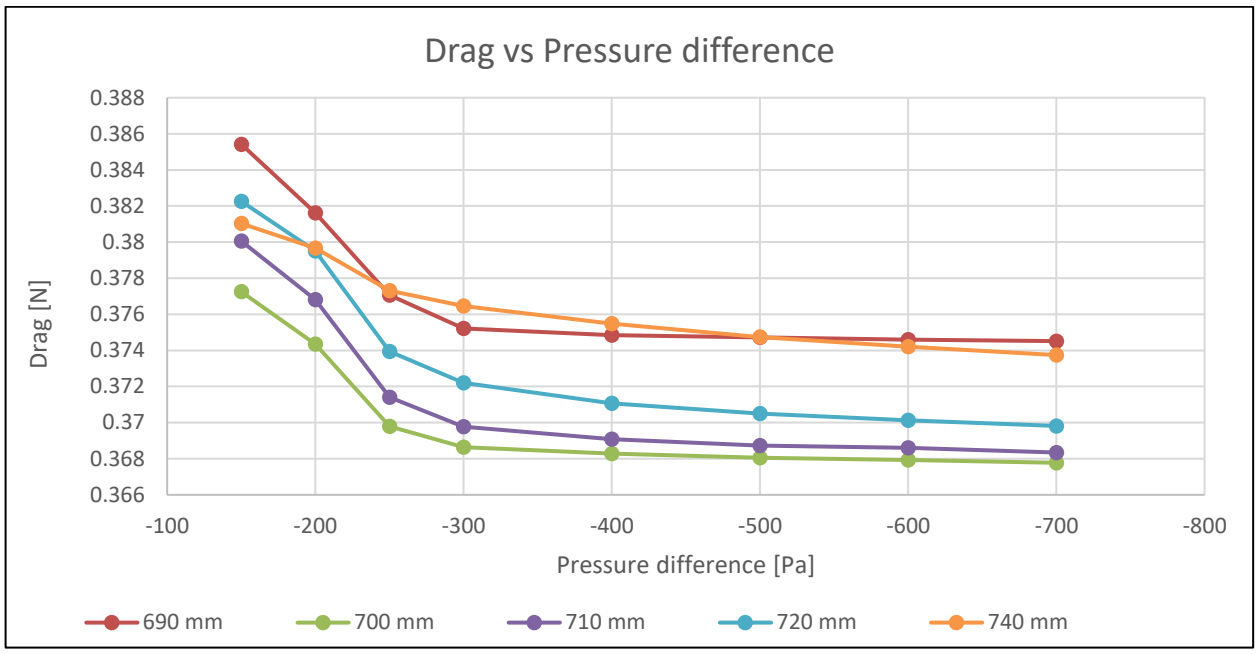

Figure 6-13: Three-dimensional boundary layer suction position results on $1-m$ chord airfoil: $Drag\ vs\ \Delta P$

In Figure 6-13 it is clear that the lowest drag was obtained when boundary layer suction was implemented $700\,mm$ from the leading edge, or on $x/c = 70\%$. The resulting drag when boundary layer suction was implemented at $x/c = 70\%$ is equal to $D = 0.367\,N$. When the pressure difference was $-700\,Pa$, the drag reduction of the airfoil, in comparison with the baseline model was $13.3\ \%$. The transition location was extended by $5.2\ \%$ from $x/c = 73.5\ \%$ to $x/c = 78.7\ \%$; this is visible in the skin friction coefficient plot in Figure 6-15. The boundary layer suction position results are tabulated in Table 6-3, including the improvement in drag coefficients and the extension of the laminar region. It was mentioned in literature that boundary layer suction improved the skin friction drag due to a stabilized boundary layer (Schlichting & Gersten, 2017). A correlation between the baseline model results and the results from the model where boundary layer suction was applied at $x/c = 70\ \%$, is demonstrated in Figure 6-14. It is clear from this visual illustration of the turbulent kinetic energy that the laminar region is extended when boundary layer suction was implemented on the airfoil.

Table 6-3: Three-dimensional boundary layer suction position results

	C_D	%	Transition $\frac{x}{c}$ [%]	%
No suction	0.00401		73.5	
Position 70%	0.00374	13.3	78.7	5.2

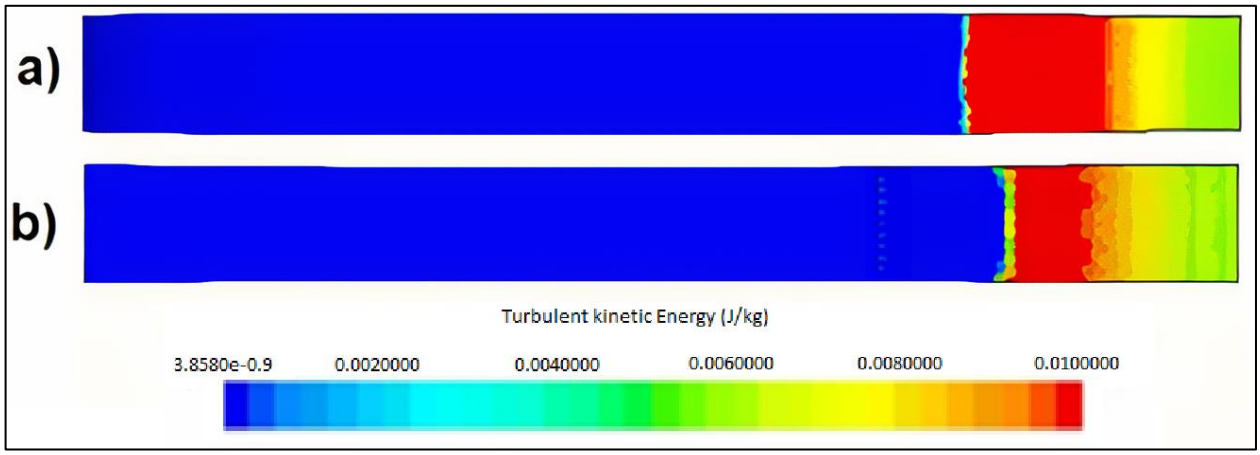

Figure 6-14: Turbulent kinetic energy comparison for the three-dimensional boundary layer suction position model: a) No suction is present, b) Boundary layer suction applied at x/c = 70%

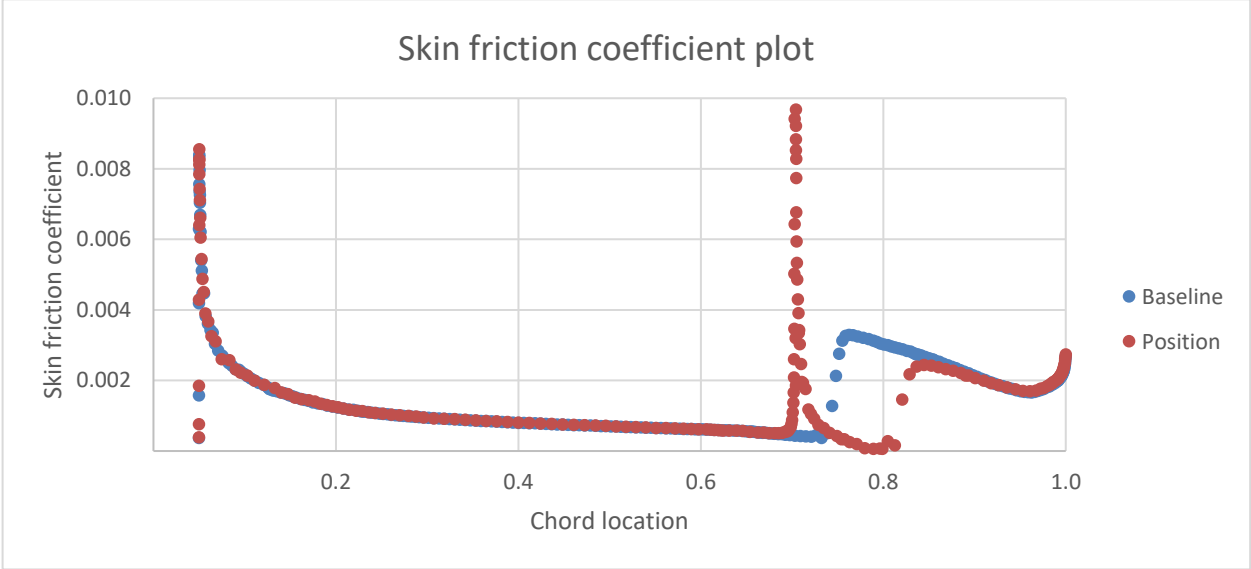

Figure 6-15: Skin friction coefficient plot for the three-dimensional boundary layer suction position model

6.4 Three-dimensional boundary layer suction hole size

The focus of this section falls on the application of boundary layer suction on the airfoil for drag reduction by altering the suction hole size. It was mentioned in section 6.3 that the maximum drag reduction took place when boundary layer suction was applied at a chord position of $x/c = 70\%$. Hence, the chord location where boundary layer suction was implemented to determine the optimum size of the suction holes, is $x/c = 70\ \%$.

6.4.1 Setup to determine three-dimensional boundary layer suction hole size

The setup to determine the optimum boundary layer suction hole size on the $1\ m$ chord airfoil was similar to Figure 6-11; the only difference being the size of the suction holes. The diameter of the suction holes for section 6.4's simulations ranges from $0.7\ mm$ to $1.2\ mm$.

6.4.2 Procedure to determine three-dimensional boundary layer suction hole size

Boundary layer suction was applied on the airfoil at x/c = 70% and the spacing between the suction holes was $10\ mm$. The diameter of the holes was changed from $0.7\ mm$ to $1.2\ mm$ during the simulations at intervals of $0.1\ mm$. The pressure was changed from $-150\ Pa$ to $-700\ Pa$ at intervals of $50\ Pa$ for the lower pressure differences, and $100\ Pa$ for larger pressure differences. The impact of the pressure change on drag was studied by looking at aerodynamic coefficients, turbulent kinetic energy and skin friction coefficient.

6.4.3 Three-dimensional boundary layer suction hole size results

The results of the simulations to find the best boundary layer suction hole size are displayed in Figure 6-16. This figure is a plot of drag versus pressure difference, which is applied to the bottom side of the chamber. Drag was the lowest when boundary layer suction hole size is equal to $0.8\ mm$, and increased when the hole size was enlarged or made smaller.

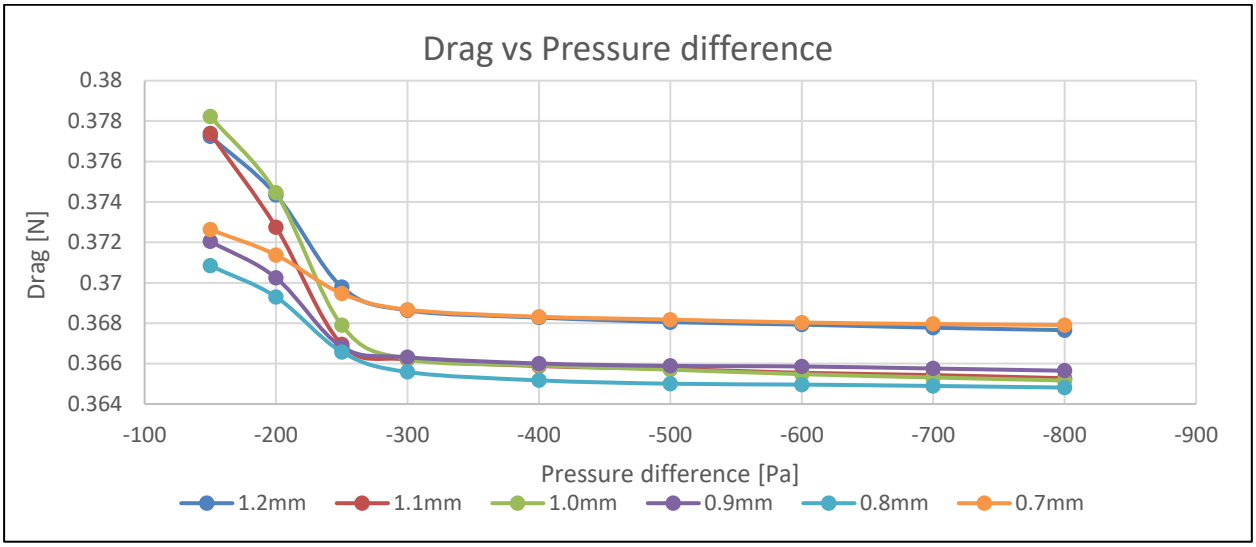

Figure 6-16: Three-dimensional boundary layer suction hole size results: Drag vs ΔP

Drag was equal to $D = 0.365\ N$ when the pressure difference was $\Delta P = -800\ Pa$. The transition location was extended by $6.5\ \%$ in comparison with the baseline model. Results from implementing the best boundary layer suction hole size are shown in Table 6-4.

Although the results show a decrease in the drag coefficient, the skin friction drag remains relatively the same. This means that there must be a reduction in the pressure drag coefficient. It was said in literature that the pressure drag coefficient would reduce as the size of the boundary layer suction holes increased (Kulkarni *et al.*, 2018). The pressure drag coefficient for the baseline model was $C_{dp} = 0.00107$. This value changed to $C_{dp} = 0.000973$ when the suction hole size was $0.8\ mm$, which means that the Cd_p value was improved by $18\ \%$.

Table 6-4: Three-dimensional boundary layer suction hole size results

	C_D	%	Transition $\frac{x}{c}$ %	%
No suction	0.00401		73.5	
Position: 70%	0.00374	13.3	78.7	5.2
Hole size: 0.8mm	0.00372	14.4	80	6.5

6.5 Three-dimensional boundary layer suction spacing

The spacing of boundary layer suction holes for drag reduction was examined and is discussed in this section. In the previous sections on the application of boundary layer suction, drag was reduced the most when boundary layer suction was applied at a chord position of $70\ \%$ and when the hole size was equal to $0.8\ mm$. These conditions were implemented to determine the spacing of the holes.

6.5.1 Setup to determine three-dimensional boundary layer suction spacing

The setup of the model to determine the optimum boundary layer suction spacing was again similar to Figure 6-11. The differences are the hole size, which was $0.8\ mm$, and the spacing of the suction holes ranged from $8\ mm$ to $12\ mm$.

6.5.2 Procedure to determine three-dimensional boundary layer suction spacing

The location where boundary layer suction implemented was $x/c = 70\ \%$, the hole size was $0.8\ mm$ and the spacing between the holes was changed from $8\ mm$ to $12\ mm$. The pressure was changed from $-150\ Pa$ to $-800\ Pa$, and the influence of the pressure change on drag was examined by studying aerodynamic coefficients, turbulent kinetic energy and skin friction coefficient.

6.5.3 Three-dimensional boundary layer suction spacing results

The results from the simulations to find the optimum boundary layer suction spacing are shown in Figure 6-17, a plot of drag versus pressure difference applied to the bottom side of the chamber. The legend of the plot displays the spacing between the boundary layer suction holes. Drag was the lowest when the spacing between the suction holes was equal to $10\ mm$, thus the results would stay the same as those from section 6.4.

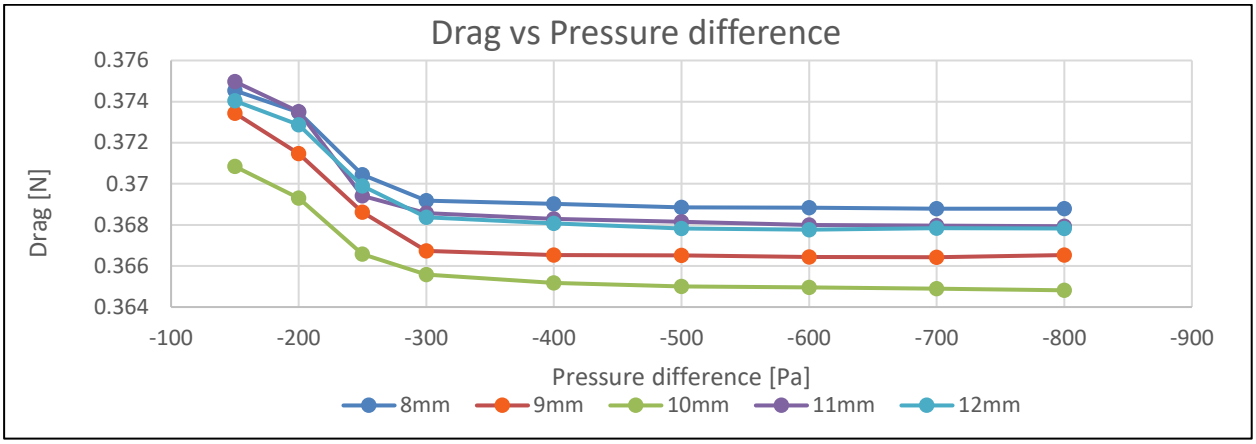

Figure 6-17: Three-dimensional boundary layer suction spacing results: Drag vs ΔP

6.6 Multiple three-dimensional boundary layer suction rows

Section 6.6 comprises of the study of the consequence of multiple boundary layer suction hole rows on drag created by the airfoil. The first row of boundary layer suction holes was applied on a chord position of $x/c = 70\ \%$, the suction hole size was $0.8\ mm$ and the spacing between the suction holes was $10\ mm$.

6.6.1 Setup for multiple rows boundary layer suction

The geometry for the application of multiple boundary layer suction hole rows is shown in Figure 6-18. The first simulations for this section include the application of two boundary layer suction holes row on the airfoil, and later on a third row was added.

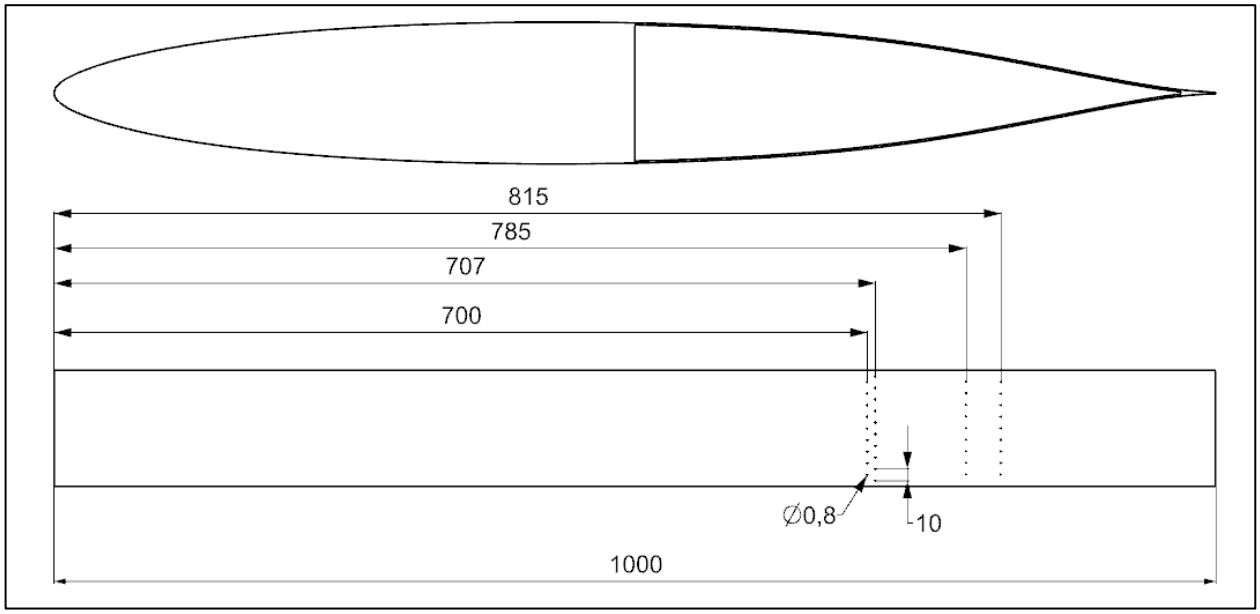

Figure 6-18: Geometry to determine the position of multiple suction rows on the three-dimensional 1 m chord airfoil

6.6.2 Procedure for multiple rows of boundary layer suction

The first row of boundary layer suction holes was applied at $x/c = 70\ \%$. The hole size was $0.8\ mm$ and the spacing between the holes was $10\ mm$. When two boundary layer suction hole rows were applied to the airfoil, the distance from the first row ranged from $5\ mm$ to $9\ mm$ at intervals of $1\ mm$. The pressure was changed from $-300\ Pa$ to $-800\ Pa$. The impact of the pressure change on drag was studied by looking at aerodynamic coefficients, turbulent kinetic energy and skin friction coefficient.

A third and fourth row of boundary layer suction holes were implemented on the airfoil by following the same procedure as with the second row. After simulating the JS3 empennage, it was clear that the pressure which was available below the horizontal stabilizer was $P = -750\ Pa$. This was used as the reference pressure for the pressure outlet.

6.6.3 Multiple rows of boundary layer suction results

The results of the application of two rows of boundary layer suction holes to the airfoil are illustrated in Figure 6-19, showing a plot of drag versus pressure difference. The legend of the plot displays the distance between the leading edge to the second row of suction holes. Drag was minimum when the second boundary layer suction row was applied $707\ mm$ from the front of the airfoil.

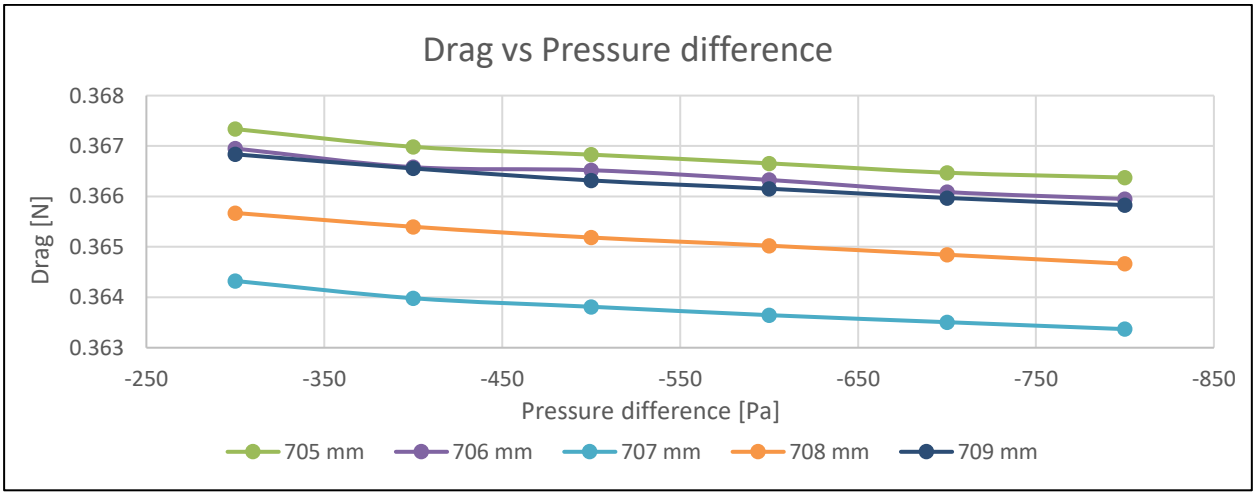

Figure 6-19: Three-dimensional results for two boundary layer suction rows: Drag vs ΔP

The results of the application of three rows of suction holes to the airfoil are depicted in Figure 6-20. This figure contains the drag and mass flow versus position when the pressure difference is equal to $\Delta P = -750\ Pa$. The drag reduction is maximum when the third row of boundary layer suction holes is implemented on the airfoil on a chord length of $x/c = 78.5\ \%$.

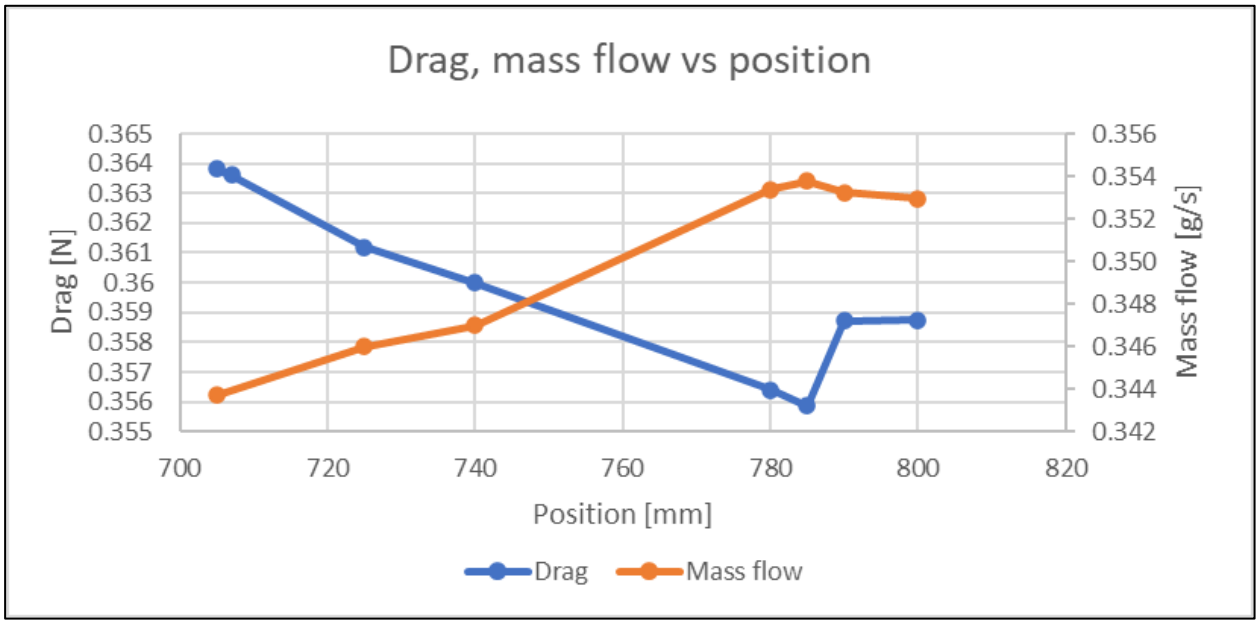

Figure 6-20: Three-dimensional results for three boundary layer suction rows

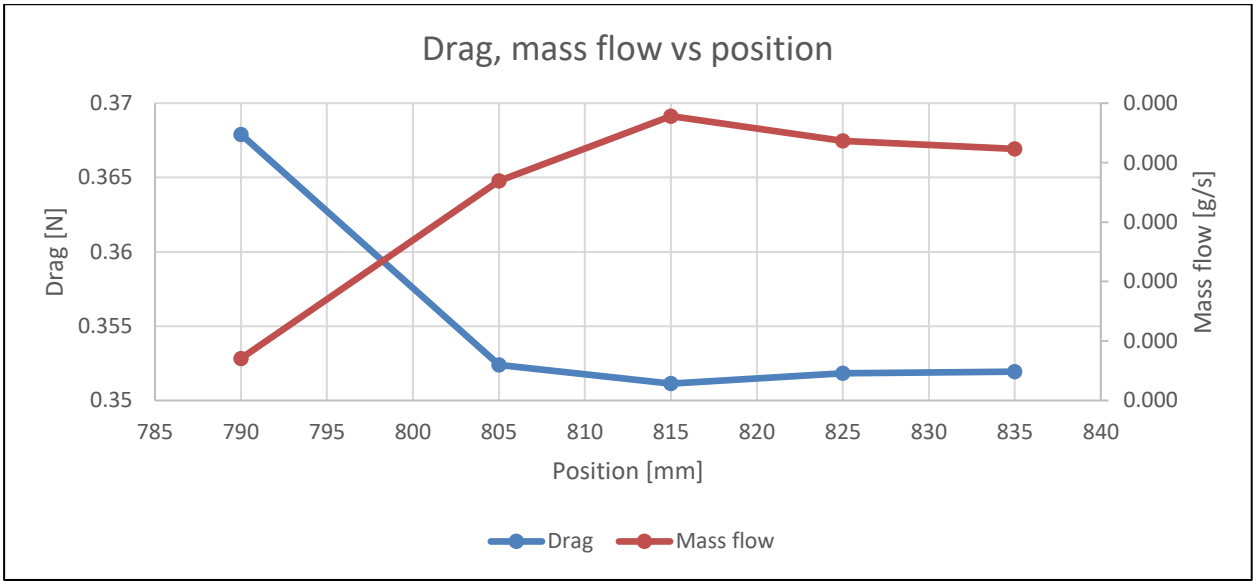

Figure 6-21: Three dimensional results, drag and mass flow vs position

All the results from the implementation of boundary layer suction are presented in Table 6-5. The skin friction coefficient plot is shown in Figure 6-22, where three rows of boundary layer suction holes were applied to the airfoil. The turbulent kinetic energy scene comparison between the baseline model and three rows of boundary layer suction holes, is presented in Figure 6-23.

Looking at the results, it is clear that the difference in drag between the implementation of the third and fourth row was not significantly large. Thus, a fifth row was not added as the improvement on the aerodynamic performance of the airfoil would be minimal.

Table 6-5: Three-dimensional boundary layer suction results

	C_D	C_D reduction from baseline [%]	Transition $\frac{x}{c}\%$	Transition extension from baseline [%]
No suction	0.00401		73.5	
Position: 70%	0.00374	13.3	78.7	5.2
Hole size: 0.8mm	0.00372	14.38	80	6.5
Spacing: 10mm	0.00372	14.38	80	6.5
2 Rows: 707 mm	0.00371	15.09	81.2	7.7
3 Rows: 785 mm	0.00361	20.19	86.4	12.9
4 Rows: 815 mm	0.00358	21.30	88.01	14.51

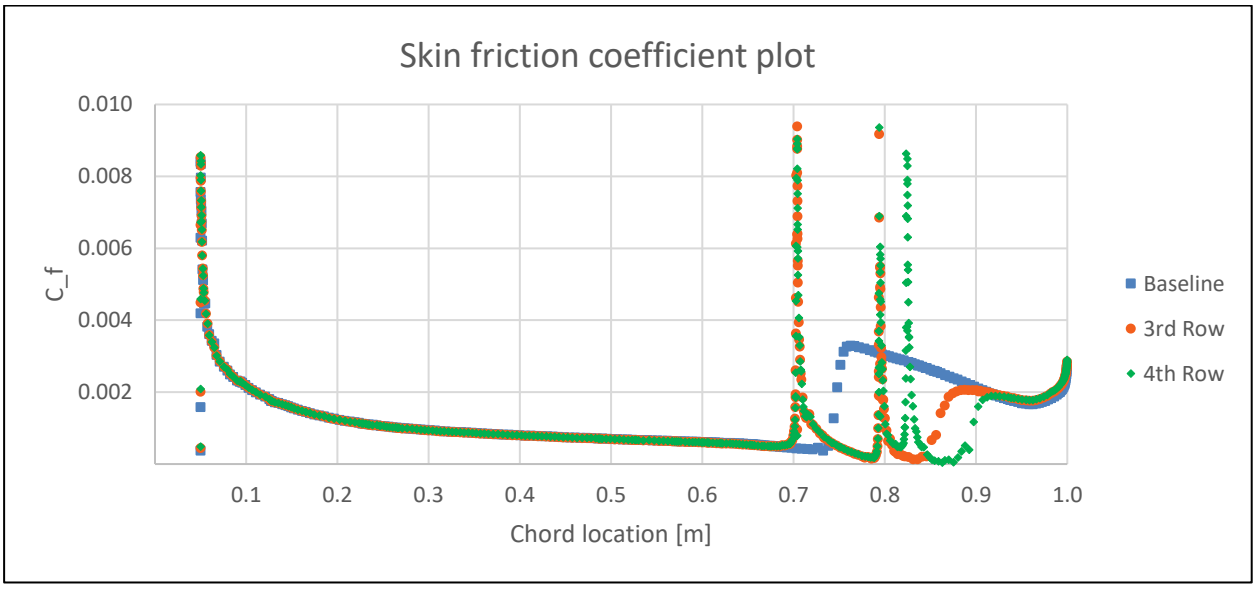

Figure 6-22: Skin friction coefficient plot: Four rows of boundary layer suction holes

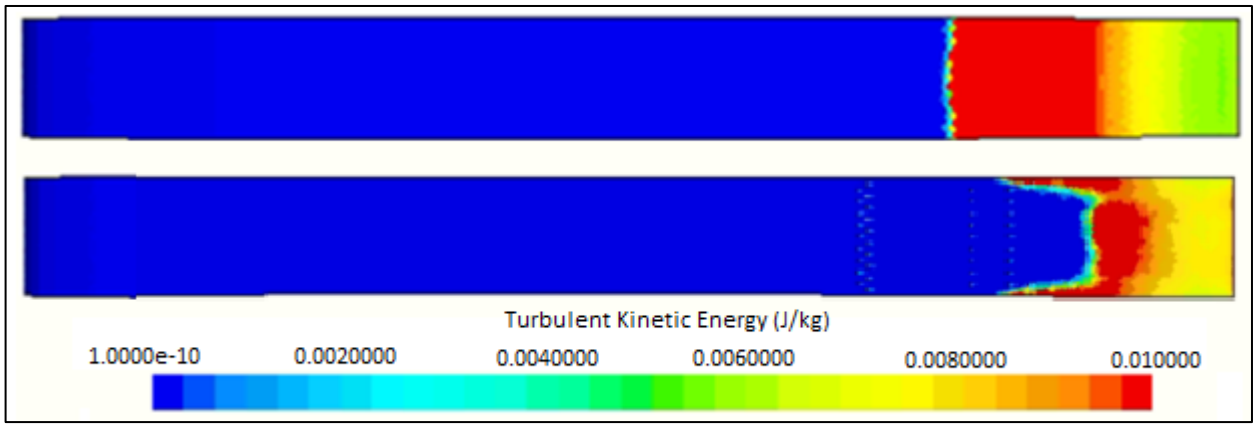

Figure 6-23: Turbulent kinetic energy comparison: Four rows boundary layer suction

6.7 Conclusion

There is an apparent increase in the laminar flow region on the airfoil with the implementation of boundary layer suction. The best results were found when boundary layer suction was applied at $x/c = 70\%$, the size of the suction holes was $0.8\ mm$ and spaced $10\ mm$ from each other. The second, third and fourth row of boundary layer suction was applied to $x/c = 70.7\%$, $x/c = 78.5\ \%$ and $\frac{x}{c} = 81.5\%$ respectively, to reduce the drag by $21.3\ \%$ and extend transition by $14.5\ \%$. These inputs were used in the investigation of the application of boundary layer suction to the vertical stabilizer of the JS3 as discussed in Chapter 7.

CHAPTER 7: BOUNDARY LAYER SUCTION SYSTEM

Boundary layer suction was applied to a simplified airfoil with the JS3 vertical stabilizer profile in Chapter 6. Substantial improvements were observed in the aerodynamic performance of the airfoil with the application of boundary layer suction. A very apparent increase in the laminar region on the airfoil was observed in the two-dimensional case studies. Boundary layer suction is subject to a further, more practical investigation by implementing suction on the vertical stabilizer of the JS3 in Chapter 7.

The input data used to obtain the results from the previous chapter was applied to the vertical stabilizer of the JS3. The simulations were once again performed at $40\ m/s$. This version of the vertical stabilizer was compared to the baseline model, where no boundary layer suction was present.

A low-pressure area is needed to drive boundary layer suction, reason being that additional energy sources which could increase the performance of the glider are prohibited in gliding competitions. FAI Sporting Code for gliding states that a glider is a fixed-wing aircraft with no means of propulsion. Thus, gliders taking part in FAI Sporting Events are forbidden to make use of pumps (Internationale, 2008).

A natural, low-pressure region on the sailplane can be used as a source for the boundary layer suction system. This region must also have the ability to create a large enough mass flow through the boundary layer suction holes to reduce the drag maximally. The outlet situated in this low-pressure zone must be designed to produce the least amount of drag to obtain meaningful results.

An outlet was designed with the primary goal to produce a natural suction flow from the pressure difference between the suction holes and the outlet. This eliminates the need for a pump in the system.

Since the focal point of this study is on boundary layer suction, the simulations were simplified by using only one half of the computational domain and by utilizing a symmetry boundary in the middle of the sailplane. Simulating only one half of the sailplane is allowed because the sailplane is symmetrical and the assumption is made that the boundary layer suction system will be implemented on both sides of the sailplane. The simulations were further simplified by applying boundary layer suction to an ideal case of the JS3 vertical stabilizer, where the gap between the vertical stabilizer and the rudder was not present. The pitot tube was also excluded, as well as the hinge between the horizontal and vertical stabilizers.

7.1 Baseline model for the JS3 vertical stabilizer

The baseline model was used as a reference to measure drag reduction when boundary layer suction was applied to the vertical stabilizer. The baseline model consists of one half of the JS3 empennage, as well as part of the tail-boom. The geometry and simulation setup are described in this section, as well as the aerodynamic results.

7.1.1 Baseline model setup

The flow domain setup was similar to the setup of the three-dimensional validation. The geometry of the empennage can be seen in Figure 7-1, where it is noted that only one half of the empennage and tail-boom was simulated. The JS3's empennage geometry was imported into STAR CCM+ and the flow field consisted of a $20 \times 10 \times 5\, m$ cuboid. The empennage was centred with regard to the height of the flow field.

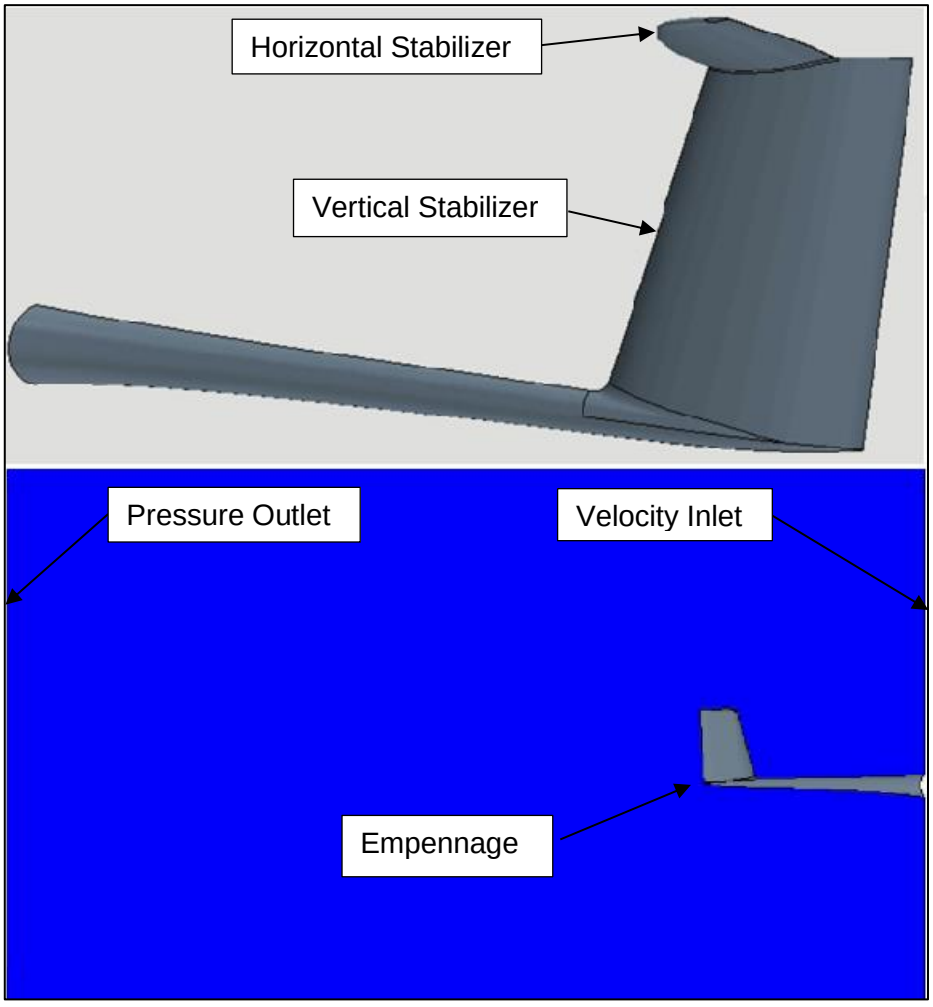

Figure 7-1: Baseline model geometry of the JS3 empennage

A polyhedral mesh was used, together with a prism layer mesh. The target cell size of the vertical and horizontal stabilizer was $5\,mm$, and the minimum cell size was $1\,mm$. A prism layer mesh was created on the surfaces with the prism layer near-wall thickness chosen to ensure that the wall y^+ value was less than 1. A total of 20 prism layers were used. Cylindrical parts with diameters of $10\,mm$ were created at the leading edges in order to define the mesh in front of the stabilizers. The mesh was refined to accurately capture the flow phenomena near the leading edges. Polyhedral cells were used for the rest of the mesh. The wake refinement behind the vertical stabilizer can be seen in Figure 7-2 a), and b) illustrates the prism layer mesh near the trailing edge of the vertical stabilizer. Figure 7-2 c) shows the mesh at the leading edge of the vertical and horizontal stabilizers.

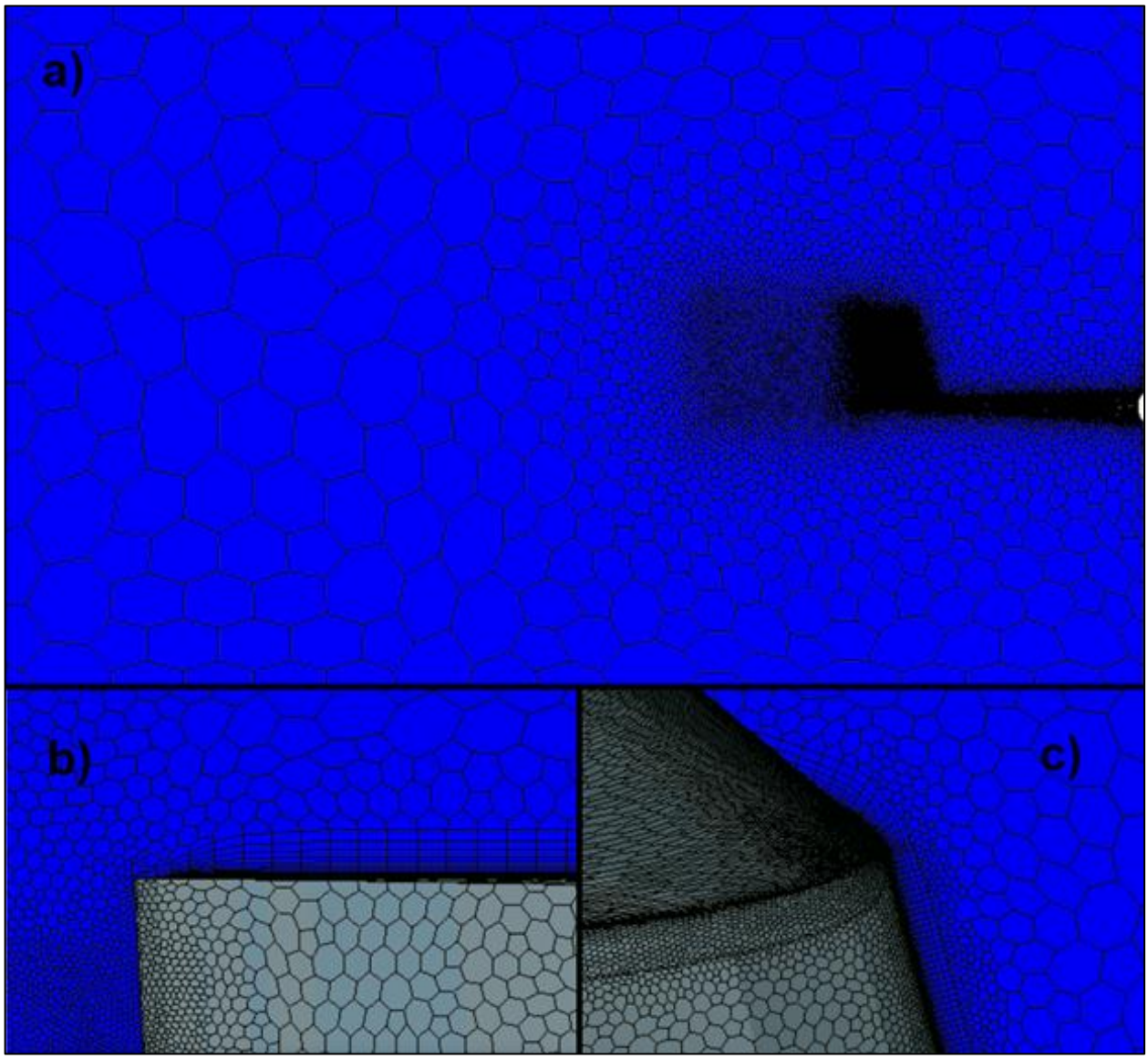

Figure 7-2: Baseline model mesh setup: a) and b) show the prism layer mesh near the trailing edge of the vertical stabilizer, c) shows the mesh at the leading edge of the vertical and horizontal stabilizers

7.1.2 Baseline model simulation procedure

After a satisfactory mesh quality was established and showing little variations in the results, a low-pressure area on the vertical stabilizer was identified. This low-pressure area was used to drive the boundary layer suction system. The aerodynamic parameters of the baseline model were then measured. These parameters were used to compare the baseline model results and the results from the model with boundary layer suction to determine how much improvement was made.

7.1.3 Baseline model CFD results

The drag value associated with the baseline model's vertical stabilizer was $D = 0.877\ N$. Note that this indicates that the vertical stabilizer's total drag was $D = 1.754\ N$, because only one side of the empennage was used. Significant improvement must be made with the application of boundary layer suction to justify the utilization of the system.

The pressure available on the vertical stabilizer was $P = -752\ Pa$, meaning that the pressure was $752\ Pa$ below the reference pressure value of $P = 101325\ Pa$. A pressure scene of the JS3 vertical stabilizer baseline model is displayed in Figure 7-3.

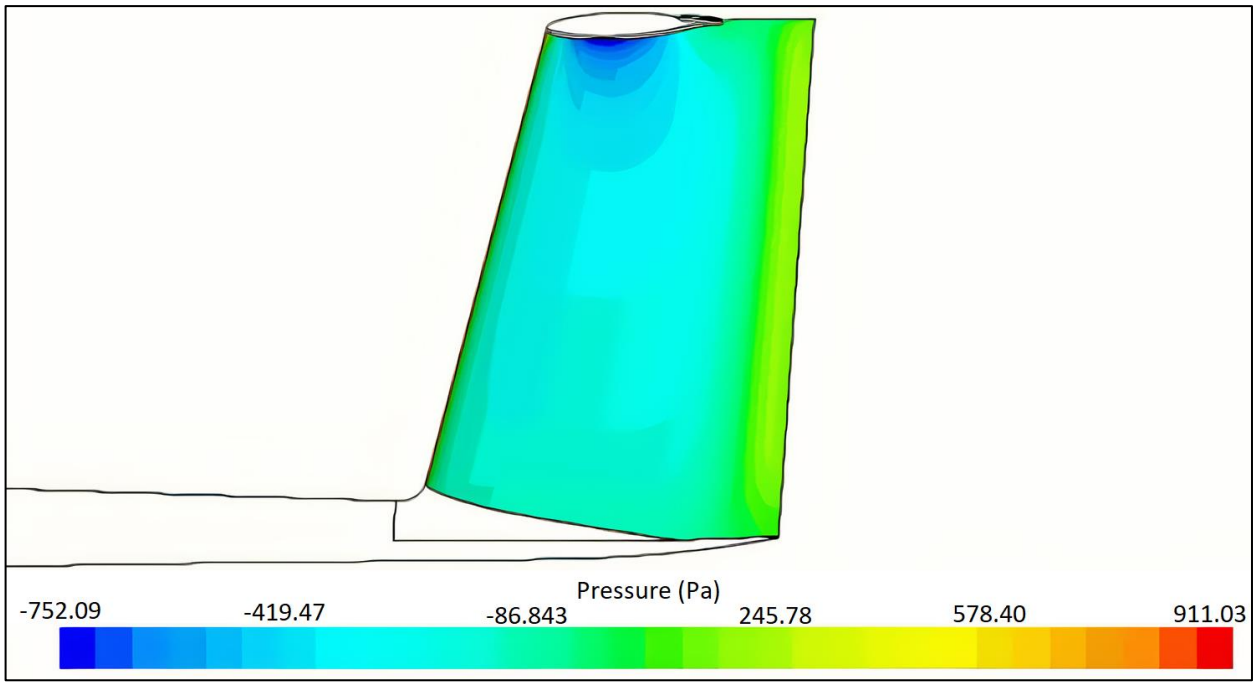

Figure 7-3: Pressure scene of the JS3 vertical stabilizer

The turbulent kinetic energy on the vertical stabilizer is illustrated in Figure 7-4. Laminar flow is indicated by the dark blue regions. Transition is depicted by the red region in the turbulent kinetic energy scene and commences at approximately three-quarters of the vertical stabilizer's chord length.

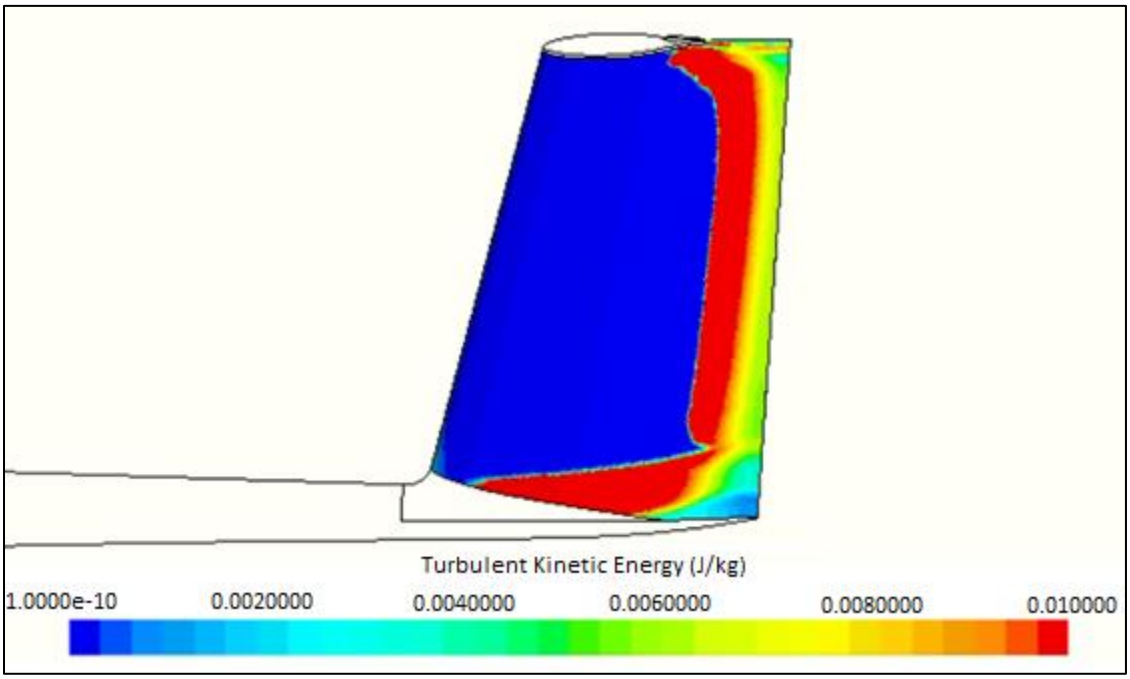

Figure 7-4: Turbulent kinetic energy on the baseline model

7.2 Boundary layer suction applied on JS3 vertical stabilizer

Boundary layer suction was implemented on the vertical stabilizer of the JS3, without being accompanied by an outlet, to determine the mass flow required to drive the system and to determine the aerodynamic performance increase. By only viewing the suction holes, the effect of boundary layer suction on the vertical stabilizer's aerodynamic performance was determined. This was only a preliminary study preceding the boundary layer suction system implemented on the vertical stabilizer.

7.2.1 Boundary layer suction setup

The setup of the flow domain was comparable to that in section 7.1. The geometry of the empennage with suction holes is illustrated in Figure 7-5. The insert in the left-hand corner of this figure displays the chamber inside the vertical stabilizer to which the suction holes are connected.

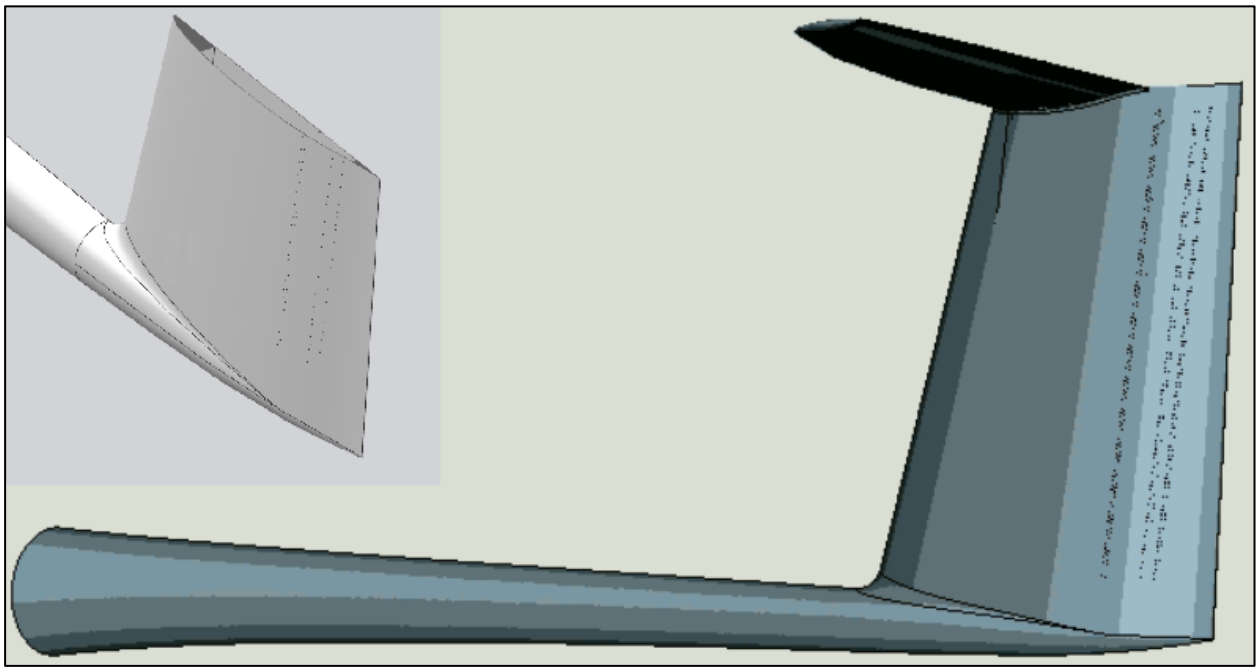

Figure 7-5: Geometry of JS3 vertical stabilizer with boundary layer suction

The only difference between this simulation setup and that of the baseline model is the mesh of the suction holes, and the chamber inside the vertical stabilizer on one side of the chamber is defined as a pressure outlet. The boundary layer suction holes were refined by using a mesh size of $0.2\ mm$. A target size of $15\ mm$ was used to refine the mesh of the chamber.

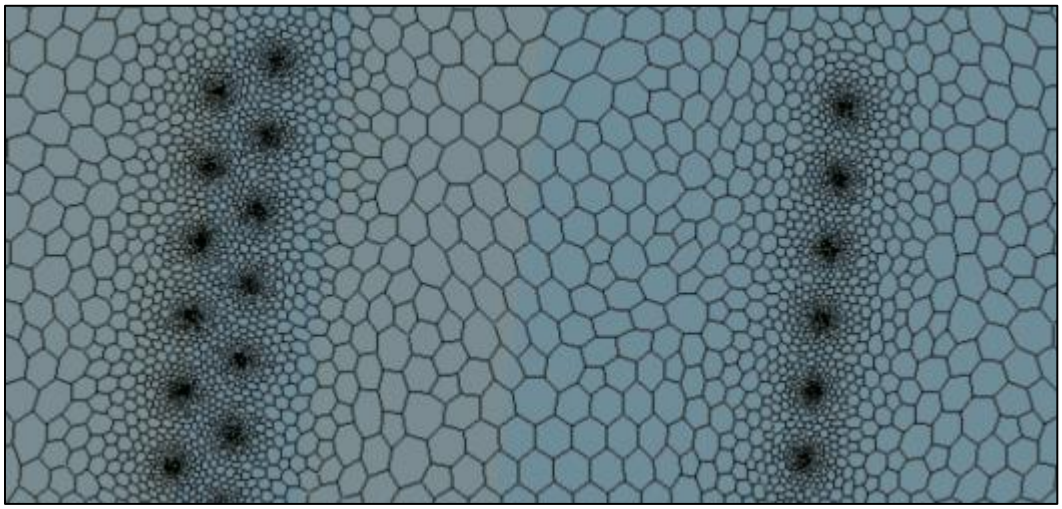

Figure 7-6: Mesh refinement around the suction holes

The side of the chamber closest to the leading edge of the vertical stabilizer was defined as a pressure outlet in STAR-CCM+. The gauge pressure value was set to $-750\ Pa$, which was the pressure available for the outlet and would generate the flow from the suction holes to the outlet.

7.2.2 Boundary layer suction procedure

The boundary layer suction data from Chapter 6 was implemented on the vertical stabilizer. Following the addition of the boundary layer suction holes and the mesh generation, the influence of boundary layer suction on the vertical stabilizer's drag was determined. This was done by comparing the drag value of the vertical stabilizer with boundary layer suction to that of the baseline model to determine what aerodynamic improvement was made.

7.2.3 Boundary layer suction results

The drag produced by one half of the JS3 vertical stabilizer with the application of boundary layer suction was $D = 0.7\ N$, which means that the total drag of the vertical stabilizer was $D = 1.4\ N$. A $20.6\,\%$ reduction in drag was obtained from the vertical stabilizer with the application of boundary layer suction when compared to the baseline model. The results of the application of boundary layer suction, without an outlet present, are tabulated in Table 7-1.

Table 7-1: Results of boundary layer suction on the JS3 empennage

	$\boldsymbol{Vertical\ stabilizer\ drag\ [N]}$	%	Mass flow [g/s]
Baseline model	0.877	-	-
Boundary layer suction	0.696	20.6	3.82

The turbulent kinetic energy scene of the JS3 vertical stabilizer with boundary layer suction is shown in Figure 7-7. A visible extension of the transition line can be seen when comparing Figure 7-7 with Figure 7-4. This means that the laminar region of the vertical stabilizer was enlarged, resulting in the lower drag.

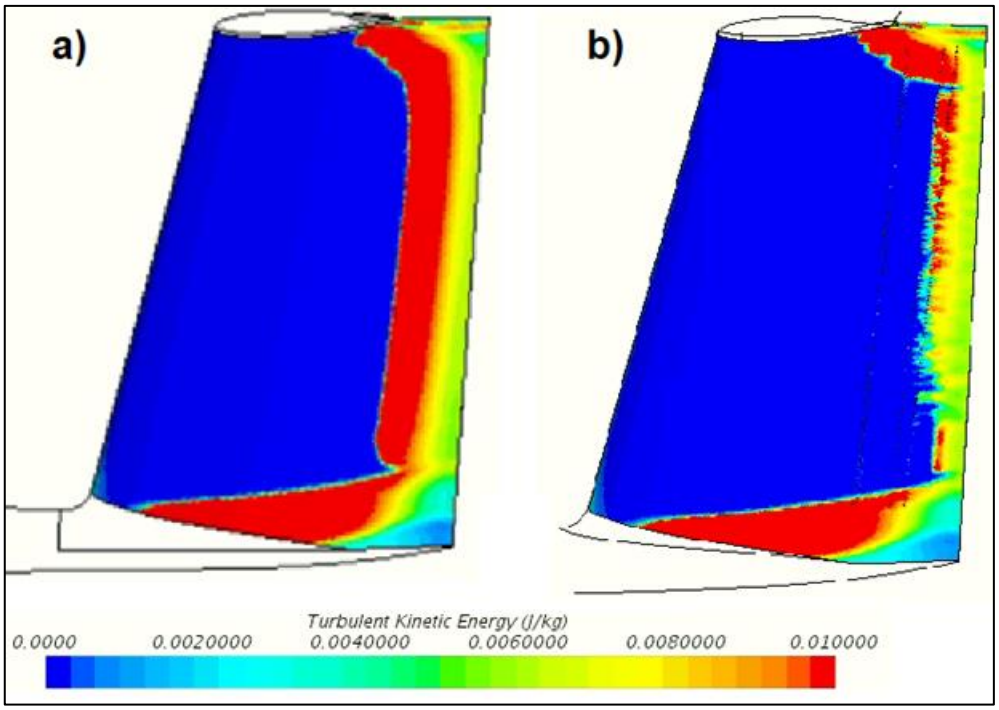

Figure 7-7: Turbulent kinetic energy scene: a) Baseline model, b) Boundary layer suction present

Boundary layer suction had little influence on an already turbulent boundary layer, which is evident on the top of the vertical stabilizer. Transition starts at the top of the vertical stabilizer before the boundary layer transitions at the bottom of the vertical stabilizer on the same chord location. The boundary layer suction holes were implemented at a constant chord length, which was determined by the studies done in Chapter 6, and the transition line of the baseline model could be used as a reference for future studies.

7.3 Boundary layer suction outlet

The function of the boundary layer suction outlet is to provide a point of exit for the air from the suction holes while creating a low-pressure area in the vertical stabilizer chamber. Air extraction must be accomplished with minimum drag generation. Therefore, the air exiting the outlet must be discharged into the free-stream without affecting the aerodynamic performance of the sailplane negatively. This air also should not cause separation from the vertical stabilizer since it will result in an increase in drag.

The point of lowest pressure in proximity to the boundary layer suction holes will deliver the best performance for the suction holes. The low-pressure region below the horizontal stabilizer, as shown in Figure 7-3, was chosen as the location for the system outlet. The difference in pressure creates a natural suction flow. When the outlet is positioned at the low-pressure area, it will operate as an air extraction device for the suction holes. This low-pressure zone is the driving force behind the boundary layer suction system.

Additional drag exists due to resistance of flow through ducts from the inlet to the outlet. Ducting of airflow increases the total drag created by the sailplane. The drag can be minimized by ensuring that the ducting has a large enough diameter so that the internal flow velocity will be low (Jonker *et al.*, 2014). This must be taken into consideration for further designing inside the chamber of the vertical stabilizer should the system be implemented. The air channel must also be hydraulically smooth to reduce the drag generated by the ducting's sidewalls. This means that the channel's roughness must be less than the thickness of the viscous sub-layer of turbulent flow to avoid an accumulation of a thick boundary layer (Schreur, 2004).

7.3.1 Boundary layer suction outlet geometry

The shape of the outlet influences the boundary layer downstream of the outlet. Also, there is a possibility of separation trailing the outlet due to the velocity change from the flow exiting the outlet to the free-stream flow velocity. The outlet concept came from the JS3 cockpit extractor, where concerns regarding the flow exiting the extractor, like flow separation, are taken into account.

To prevent separation from occurring, the outlet's rear wall was designed to be tangent to the surface of the vertical stabilizer (Jonker, 2011). The head loss due to inlet, outlet and friction can be minimized by shaping the outlet in the form of a trumpet so that the inlet area is larger than the outlet area (Jonker, 2011), as illustrated in Figure 7-8.

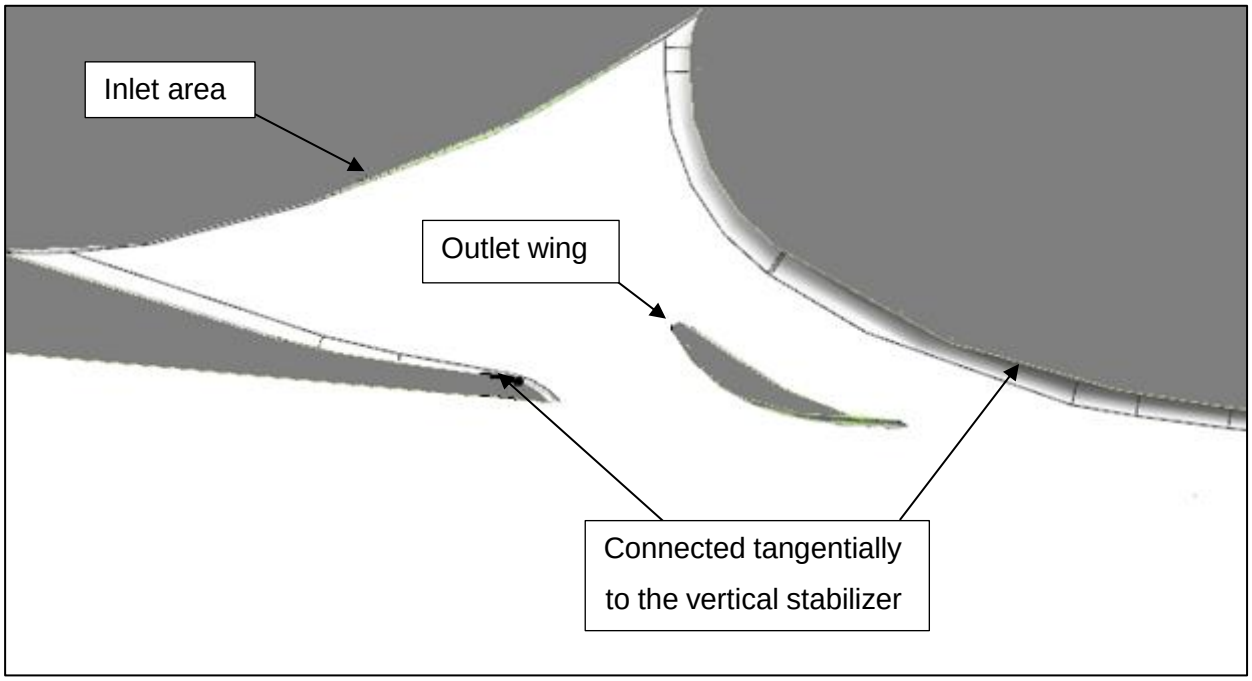

Figure 7-8: Cross-sectional view of the outlet

Transition and separation can be postponed when the critical Reynolds number is increased (Gad-El-Hak, 2000). The purpose of the outlet wing (see Figure 7-8) is to alter the shape of the velocity profile by increasing the velocity near the vertical stabilizer wall and therefore increasing the critical Reynolds number. By adding the outlet wing, the velocity difference between the flow exiting the outlet and the free-flow is reduced (Jonker, 2011). If the wake's velocity is less than the free-stream velocity, the introduction of exhaust air at a velocity close to the free-stream velocity may lead to drag reduction (Schreur, 2004).

Another benefit of the outlet wing is the downward velocity component that is created, which reduces the boundary layer height (Jonker, 2011). Lowering the boundary layer height means that the pressure drag is lower when the boundary layer stays adhered to the vertical stabilizer (Young, 1989).

7.3.2 Boundary layer suction outlet procedure

The boundary layer suction outlet was implemented on the vertical stabilizer of the JS3 without the suction holes being present. To determine the outlet throat area, which will provide the correct mass flow through the outlet, an iterative process was used by refining the outlet. After the mesh was generated and the simulation was run, the ventilation rate was determined by the required flow through the suction holes.

7.3.3 Boundary layer suction outlet results

The development of the boundary layer suction outlet is shown in Figure 7-9. A velocity vector scene is illustrated of the flow through the outlet. Too many sharp edges and bulky parts were present in the first version of the outlet. The first version also provided a mass flow of $2\ g/s$, which was almost five times the required amount of airflow. The throat of the outlet that provides sufficient negative pressure inside the chamber is equal to $185\ mm^2$, and this version of the outlet provided a mass flow of $0.35\ g/s$.

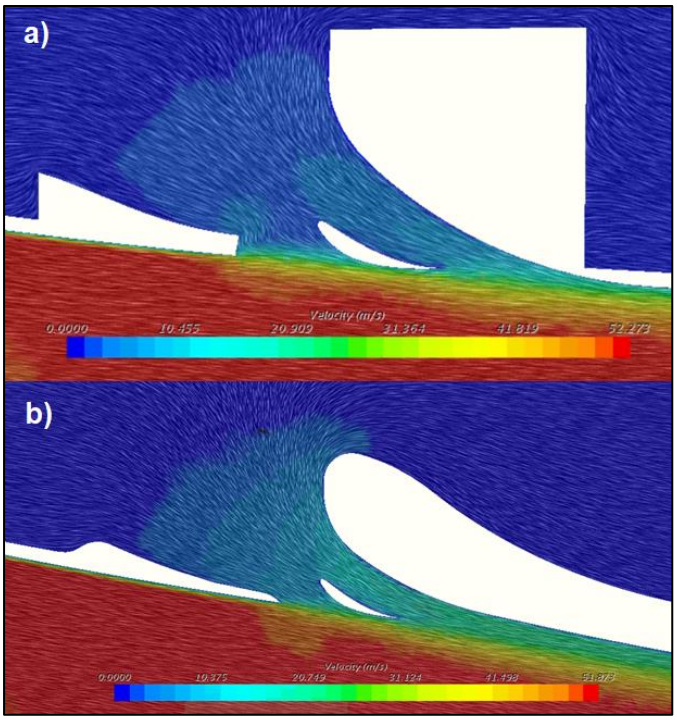

Figure 7-9: Velocity vector scene of the boundary layer suction outlet: a) First version, b) Last version

7.4 Boundary layer suction system

The previous sections' input data were combined to form the boundary layer suction system on the JS3 vertical stabilizer. Boundary layer suction was applied to the vertical stabilizer, with the outlet present as well. The results from this model were then compared to the results of the baseline model to determine if improvements on the aerodynamic performance of the sailplane were made.

7.4.1 Boundary layer suction system setup

The flow domain setup was similar to the previous sections. The suction holes are linked to the outlet with the chamber inside the vertical stabilizer. Figure 7-10 displays the geometry of the vertical stabilizer with the boundary layer suction system. To determine if the low-pressure area, where the outlet was situated, has the required influence on the airflow to drive the system, no part on the empennage was defined as a pressure outlet.

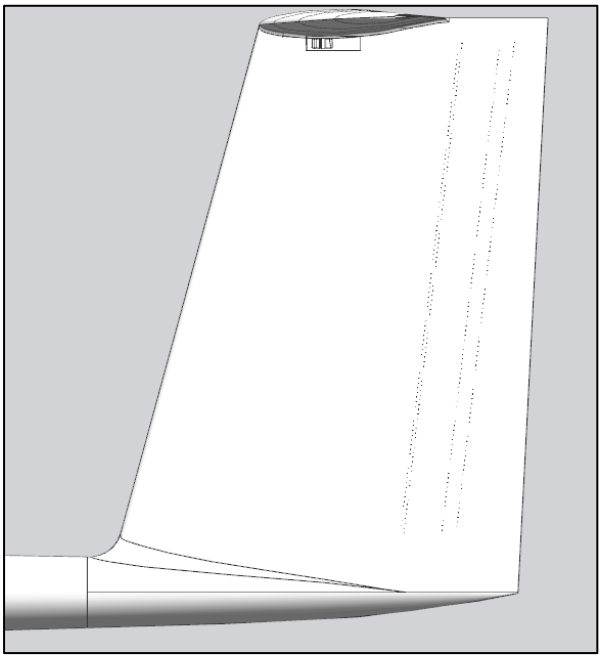

Figure 7-10: Boundary layer suction system geometry

7.4.2 Boundary layer suction system procedure

After the geometry of the empennage with the boundary layer suction system was imported into STAR-CCM+, and the model's mesh was adequately refined, the simulation was run. The aerodynamic parameters were measured and were used to compare to the results of the baseline model of the JS3 empennage.

7.4.3 Boundary layer suction system results

The vertical stabilizer's drag, with the combined boundary layer suction system applied, was equal to $D = 0.89\ N$. Compared to the baseline model's drag, the drag increased with $1.3\ \%$ even though there was a drag reduction of $20.6\ \%$ when only the boundary layer suction holes were present on the vertical stabilizer. The results from the boundary layer suction system are assembled in Table 7-2.

Table 7-2: Results from the application of boundary layer suction system on the JS3 vertical stabilizer

	$\boldsymbol{Vertical\ Drag\ [N]}$	**%**
Baseline model	0.877	-
Boundary layer suction holes alone	0.696	20.58
Boundary layer suction system	0.888	-1.32

The turbulent kinetic energy scene of the vertical stabilizer can be seen in Figure 7-11. The vertical stabilizer of the baseline model is compared to the model with the application of the boundary layer suction system. The extension of the transition line was similar for this case, compared to when only the boundary layer suction was implemented on the vertical stabilizer. This means that the outlet provides enough mass flow through the suction holes, but the increase in drag due to the outlet is too high.

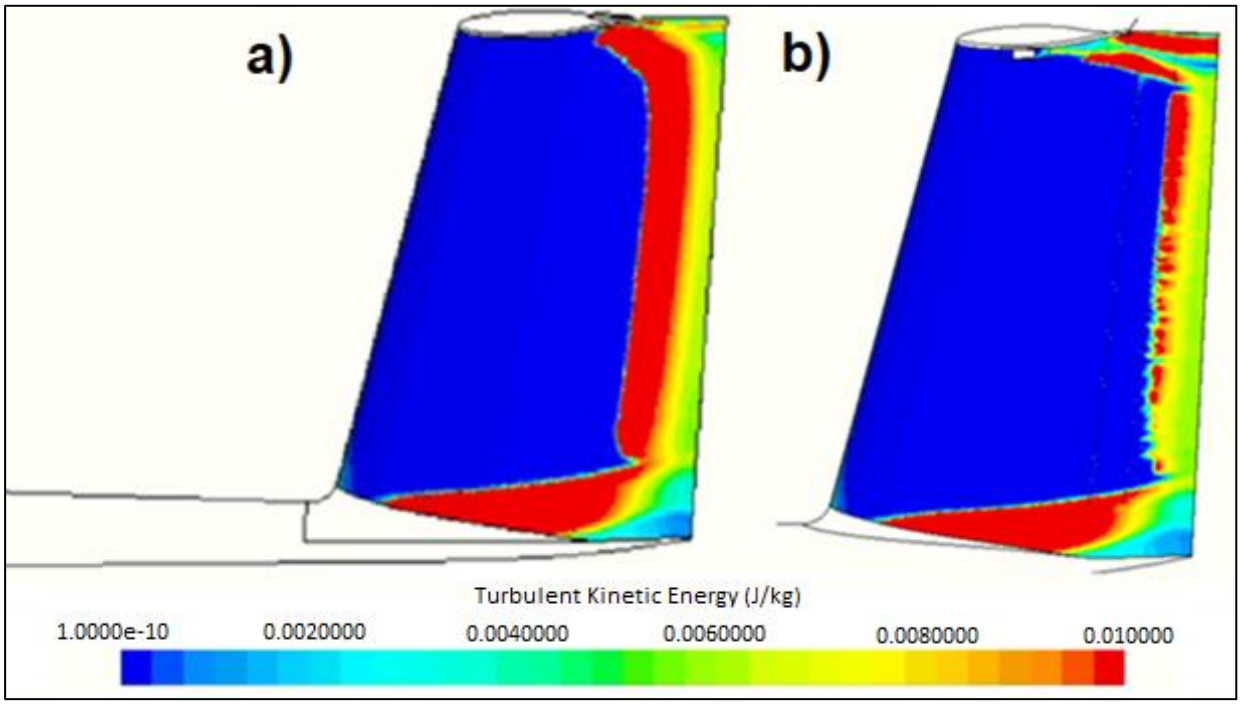

Figure 7-11: Turbulent kinetic energy scene: a) Baseline model, b) Boundary layer suction system

CHAPTER 8: CONCLUSION AND RECOMMENDATIONS

The main objective of this dissertation was to investigate the implementation of a boundary layer suction system on the JS3's vertical stabilizer, without making use of a pump to drive the system but rather a natural occurring low-pressure zone as the suction source. The findings from this project are summarized in Section 8.1, as well as indicating the extent of the objective that has been reached. In section 8.2, recommendations for future studies are given.

8.1 Conclusion

Boundary layer suction was identified as a method to extend transition and increase the laminar flow region. It is an active boundary layer control method that reduces the boundary layer thickness (Green, 1997), and keeps the boundary layer stabilized by filling up the velocity profile near the wall (Schlichting & Gersten, 2017). Even though this stabilized boundary layer increases the local skin friction, the total skin friction is still lower than that of a turbulent boundary layer. A laminar boundary layer also produces less pressure drag, resulting in a lower total drag for a laminar boundary layer.

Matters regarding the suction hole size and angle, the suction chord location and the suction velocity were addressed next. Additionally, specific challenges regarding boundary layer suction which must be taken into account during the implementation of a boundary layer suction system were discussed. These include manufacturing and maintenance, as well as external factors such as insect contamination and weather-related water ingress.

The next part of the report documented the motives for using CFD as a tool to model boundary layer suction. Drag prediction with CFD was reviewed, which included topics like mesh generation, boundary conditions, transition and turbulence models. It was found that the SST $K-\omega$ turbulence model is a suitable choice because of its low memory requirements, good convergence and accuracy. The $\gamma - Re_\theta$ transition model was used because it predicts the onset of transition well.

The first objective of this dissertation was to validate the CFD models with experimental data with similar flow conditions as found on sailplanes. A two-dimensional validation was conducted on the NACA-0018 airfoil and was simulated between $0°$ and $16°$ AOA in order to compare the aerodynamic coefficients from STAR-CCM+ to those of XFOIL and wind tunnel test results. At lower angles of attack, the results from STAR-CCM+ compared well with XFOIL and wind-tunnel data, but the error increased when the angle of attack increased beyond $9°$. The three-dimensional validation was also performed on STAR-CCM+ and the results were compared to a

study by Hansen (2014), as well as flight tests on the Standard Cirrus glider. The STAR-CCM+ model compared well with Hansen's study and the speed-polar graph of the flight tests.

The implementation of boundary layer suction on an airfoil with the shape of the JS3 vertical stabilizer was the next objective for this dissertation. A preliminary study was conducted on a two-dimensional airfoil of the JS3 vertical stabilizer. This study gave sufficient evidence of drag reduction on the airfoil and boundary layer suction was further investigated on a three-dimensional airfoil.

Three-dimensional studies on the JS3 vertical stabilizer airfoil included identifying the position, suction hole diameter, spacing and number of rows for drag reduction. These studies concluded that the first row of boundary layer suction holes must be applied at $x/c = 70\%$, the diameter of the holes must be $0.8\ mm$ and spaced $10\ mm$ from each other. The second, third and fourth row were implemented at $x/c = 70.7\%$, $x/c = 78.5\ \%$ and $\frac{x}{c} = 81.5\%$ respectively, to reduce the drag by $21.3\ \%$ and extend transition by $14.5\ \%$.

A natural occurring, low-pressure zone in proximity to the suction holes on the vertical stabilizer was identified below the horizontal stabilizer. This low-pressure area was implemented to create a natural suction flow to operate as an extraction device for the suction holes. The outlet was designed according to the cockpit extractor of the JS3, where separation was prevented by designing the outlet to be tangent to the surface of the vertical stabilizer. The head loss was minimized by shaping the outlet in the form of a trumpet (Jonker, 2011). The outlet wing was added to increase the critical Reynolds number by altering the shape of the velocity profile near the surface of the vertical stabilizer. This increase in the critical Reynolds number postpones transition and separation (Gad-El-Hak, 2000). The outlet wing also reduces the difference in the velocity of the outer flow and the flow exiting the outlet (Jonker, 2011).

Boundary layer suction was first applied to the vertical stabilizer without the presence of the outlet. A net gain in performance of $20\ \%$ was achieved with the implementation of suction holes. When the outlet was added to the vertical stabilizer, the drag of the vertical stabilizer was increased by $1.2\ \%$ compared to the baseline model. Although the boundary layer suction system did not show an adequate reduction in drag on the vertical stabilizer, the favourable results from the application of boundary layer suction alone can be used on future designs of sailplanes.

8.2 Recommendations

For future research on the application of boundary layer suction, the following recommendations can be taken into consideration:

- Modification of the vertical stabilizer airfoil to obtain a more substantial percentage laminar flow over the airfoil with passive laminar flow control.
- The ideal case for the JS3 vertical stabilizer was simulated, without the influence of external factors. The gap between the vertical stabilizer and the rudder must be taken into account in future studies.
- The boundary layer suction system can be studied at a higher cruise speed to see if the results are favourable.
- A more in-depth study can be conducted on the design of the outlet to reduce the drag added to the boundary layer suction system.
- The possibility of further drag reduction can be investigated with a fifth row of boundary layer suction holes.
- A low-pressure zone near the trailing edge of a sailplane surface will reduce the amount of drag generated by the outlet. The possibility of such a location can also be investigated
- Boundary layer suction has been applied by using the chord position of the vertical stabilizer as reference. Another possibility is to use the transition line (from Figure 7-7) as a reference instead because the boundary layer turns turbulent at the top before the bottom.

BIBLIOGRAPHY

A Medida, S. 2014. Correlation-based Transition Modeling for External Aerodynamic Flows.

Almohammadi, K.M., Ingham, D.B., Ma, L. & Pourkashan, M. 2013. Computational fluid dynamics (CFD) mesh independency techniques for a straight blade vertical axis wind turbine. *Energy*:483-493.

Anderson, J. 1995. Computational Fluid Dynamics: McGraw-Hill Education.

Andersson, B., Andersson, R., Håkansson, L., Mortensen, M., Sudiyo, R. & van Wachem, B. 2011. Computational Fluid Dynamics for Engineers. Cambridge: Cambridge University Press.

Beck, N., Landa, T., Seitz, A. & Boermans, L. 2018. Drag Reductiom by Laminar Flow Control. *Energies*:252.

Blazek, J. 2015. Chapter 1 - Introduction. *(In* Blazek, J., *ed.* Computational Fluid Dynamics: Principles and Applications (Third Edition). Oxford: Butterworth-Heinemann. p. 1-5).

Boermans, L. 2006. Research on Sailplane Aerodynamics at Delft University of Technology. *Netherlands Association of Aeronautical Engineers*:10-12.

Braslow, A.L. 1999. A History of Suction Type Laminar Flow Control with Emphasis on Flight Research, Monograpgh in Aerospace History, No. 13. Washington, D.C.: NASA History Division, Office of Policy and Plans.

Bridges, D.H. 2007. Early flight-test and other boundary-layer research at Mississippi State 1949-1960. *Journal of Aircraft*, 44(5):1635-1642.

Carmichael, B.H. 2002. Some events in suction stabilization of the laminar boundary layer or anyone for 100% laminar flow. *Technical Soaring*, 26:70-75.

CD-Adapco. 2016. User Guide. *STAR CCM+ v2019.1*.

Chattot, J.J. & Hafez, M.M. 2015. Theoretical and applied aerodynamics: And related numerical methods.

Drela, M. & Giles, M.B. 1987. Viscous-inviscid analysis of transonic and low Reynolds number airfoils. *AIAA Journal*, 25(10):1347-1355.

El khchine, Y. & Sriti, M. 2017. Boundary layer and amplified grid effects on aerodynamic performances of S809 airfoil for horizontal axis wind turbine (HAWT). *Journal of Engineering Science and Technology*, 12:3011-3022.

FAA. 2003. Glider flying handbook. [Washington, D.C.].

Gad-El-Hak, M. 2000. Flow Control: Passive, Active and Reactive Flow Management. Cambridge: Cambridge University Press.

Gleyzes, C., Cousteix, J. & Bonnet, J.L. 1984. A Calculation Method of Leading-Edge Separation Bubbles. (*In* Cebeci, T. Numerical and Physical Aspects of Aerodynamic Flows II organised by Berlin, Heidelberg: Springer Berlin Heidelberg. p. 173-192).

Green, B.E. 1997. An approach to the constrained design of natural laminar flow airfoils [microform] / Bradford E. Green. Hampton, Va. : [Springfield, Va: National Aeronautics and Space Administration, Langley Research Center ; National Technical Information Service, distributor.

Hansen, T. 2014. Modeling the Performance of the Standard Cirrus Glider using Navier-Stokes CFD. *Technical Soaring*, 38:5-14.

Houghton, E.L., Carpenter, P.W., Collicott, S.H. & Valentine, D.T. 2016. Aerodynamics for Engineering Students: Butterworth-Heinemann.

Huang, L., Huang, P., Lebeau, R. & Hauser, T. 2004. Numerical Study of Blowing and Suction Control Mechanism on NACA0012 Airfoil. *Journal of Aircraft - J AIRCRAFT*, 41:1005-1013.

Internationale, F.A. 2008. FAI Sporting Code. *Fai.org*.

Jonker, A.S. 2011. Performance enhancing elements for an 18m-Class glider. Potchefstroom: North West University.

Jonker, A.S., Bosman, J.J., Mathews, E.H. & Liebenberg, L. 2014. Flow over a glider canopy. *The Aeronautical Journal*:669-682.

Joslin, R.D. 1998. AIRCRAFT LAMINAR FLOW CONTROL. *Annual Review of Fluid Mechanics*, 30(1):1-29.

Katz, J. 2003. Race Car Aerodynamics: Bentkey Pub.

Khalil, E.E. & Akademia Baru, P. 2012. CFD History and Applications. *CFD Letters*, 4:2012.

Kulkarni, R., Rohit, B., Lokanatha, V. & Lokesh, C. 2018. Understanding boundary layer suction and its e ect on wings - A review. *IOP Conference Series: Materials Science and Engineering*, 376:012030.

L. Oberkampf, W., N. Sindir, M. & T. Conlisk, A. 1998. AIAA Guide for the Verification and Validation of Computational Fluid Dynamics Simulations.

Langtry, R. 2006. A correlation-based transition model using local variables for unstructured parallelized CFD codes.

McCormick, B.W. 2009. Aerodynamics, Aeronautics and Flight Mechanics. New York: Wiley.

McMasters, J.H.N.-W., J.L. 1977. Soaring the next 25 years. Some technical extrapolations. *Soaring*, 41(1):21-28.

Menter, F.R. 1994. Two-equation eddy-viscosity turbulence models for engineering applications. *AIAA Journal*, 32(8):1598-1605.

Murad, N., Naser, J., Alam, F. & Watkins, S. 2004. Simulation of Vehicle A-Pillar Aerodynamics using various Turbulence Models. *SAE Technical Papers*.

Naviter. 2018.

Official results for Meter 18 on task 7. https://www.soaringspot.com/en_gb/sanats2018/results/18-meter/task-7-on-2018-10-06/daily Date of access: 15 March 2019.

Oberkampf, W.L., Sindir, M. & Conlisk, A.T. 1998. Guide for the verification and validation of computational fluid dynamics simulations. *American Institute of Aeronautics and Astronautics, Reston, VA*.

Oskam, B. & Slooff, J. 1998. Recent advances in computational aerodynamics at NLR. 36th AIAA Aerospace Sciences Meeting and Exhibit.

Pätzold, F. 2012. Preliminary Results of Flight Performance Determinationof Cirrus75 D-6607 S/N 633. Paper presented at the Idaflieg.

Pfenninger, W. & Groth, E. 1961. LOW DRAG BOUNDARY LAYER SUCTION EXPERIMENTS IN FLIGHT ON A WING GLOVE OF AN F-94A AIRPLANE WITH SUCTION THROUGH A LARGE NUMBER OF FINE SLOTS. *(In* Lachmann, G.V., *ed.* Boundary Layer and Flow Control. Pergamon. p. 981-999).

Sadrehaghighi, I. 2020. Mesh Generation in CFD.

Saric, W.S. 1992. Laminar-turbulent transition: fundamentals. Special Course on Skin Friction Drag Reduction (réduction de Traînée de Frottement). Advisory Group for Aerospace Research & Development, North Atlantic Treaty Organization.

Schlichting, H. & Gersten, K. 2017. Boundary-Layer Theory. Berlin: Springer-Verlag.

Schreur, B.W. 2004. The Ventilation of Streamlined Human Powered Vehicles.

Shi, Y., Bai, J., Jun, H. & Tihao, Y. 2015. Numerical analysis and optimization of boundary layer suction on airfoils. *Chinese Journal of Aeronautics*, 30.

Sosnowski, M., Krzywanski, J. & Gnatowska, R. 2017. Polyhedral meshing as an innovative approach to computational domain discretization of a cyclone in a fluidized bed CLC unit. *E3S Web Conf.*, 14:01027.

Spalart, P. & McLean, J. 2011. Drag reduction: Enticing turbulence, and then an industry. *Philosophical transactions. Series A, Mathematical, physical, and engineering sciences*, 369:1556-1569.

Talay, T.A., Aeronautics, U.S.N., Scientific, S.A., Office, T.I. & Center, L.R. 1975. Introduction to the Aerodynamics of Flight: Scientific and Technical Information Office, National Aeronautics and Space Administration; Springfield, Va.

Thomas, F. & Milgram, J. 1999. Fundamentals of Sailplane Design: College Park Press.

Timmer, W. 2008. Two-dimensional low-Reynolds number wind tunnel results for airfoil NACA 0018. *Wind engineering 32(6), 525-537*, 32.

Tu, J., Yeoh, G.H. & L, C. 2008. Computational Fluid Dynamics: A Practical Approach. Oxford: Butterworth-Heinemann.

Van Dam, C.P. 1999. Recent experience with different methods of drag prediction. *Progress in Aerospace Sciences*, 35(8).

Van de Wal, H. 2010. Design of a wing with boundary layer suction.

van Leer, B. 2010. Introduction to Computational Fluid Dynamics.

Yang, Z. & Schenkel, M. 2004. Assessment of Closed-Wall Wind Tunnel Blockage using CFD.

Young, A.D. 1989. Boundary Layers. Washington, D.C.: American Institute of Aeronautics and Astronautics.

Yousefi, K., Saleh, R. & Zahedi, P. 2013. Numerical Investigation of Suction and Length of Suction Jet on Aerodynamic Characteristics of the NACA 0012 Airfoil. Vol. 1.

Zahn, J. 2017. Control of the Impact of Steps and Gaps on Laminar-Turbulent Transition in Boundary Layers.